Microfluidic platforms: from 3D printing to µPADs for chemical and biological applications

In Partial Fulfillment of the Requirements for the Degree of Doctor by UPC

Author:

Pouya Mehrdel

Supervisor:

Prof. Jasmina Casals-Terré

June 2021

Acknowledgment

First of all, I would like to express my sincere gratitude to Professor Jasmina Casals-Terré for her unconditional support and her patience in teaching and guiding me. Her extensive experience, deep knowledge and extraordinary ingenuity saved me multiple times. But more than everything, I appreciate her efforts in teaching me on how to think strategically and I know that she suffered a lot in taming my instinctive stubbornness (for which I'm extremely sorry!). I think, I am now more professional, cooperative and flexible than before. Also, I would like to thank Dr. Josep Farre Llados for his assistance during my PhD. Moreover, I am grateful to Professor Jordi Romeu Garbi for his support. Although he wasn't my supervisor, he never ceased his help and support.

I won't be frank if I don't confess how much I owe to my best friend, who happens to be my wife too! She always had my back and supported me without any questions. How could I handle the ups and downs of my life in the passing years without her unconditional companionship? I just want to say, I'm very lucky to have someone like Sepid in my life. I will never forget her tolerance, sympathy and empathy.

I also want to express my appreciation to my colleagues at the Microtech Laboratory; Genis Rabost, Enric Perarnau Olle, Hamid Khosravi, Oriol Caro Ignacio, Oscar Carreras Gallo, Joan Antoni Lopez Martinez and Shadi Karimi. Although Shadi and I were working on different projects, our works had many mutual aspects and it was more convenient for us to work together. During our PhD journey, Shadi and I passed through some dark, dreadful and misty valleys (which are now filled with our blood, sweat and tears), but we made it at any costs. I couldn't make it without Shadi's help. Thanks Shadi.

I had magnificent tutors, helpful colleagues and a loving and supportive wife, but Sepid and I also made some great friends in the past years. Shahin, Elnaz, Milad, Mahsa, Hamid (alavi), Hamid (ghorbani), Neda and Ariana made our living in Spain quite easier and we enjoyed a lot from their companionship. They were always with us in our hard days and we appreciate their support. Thanks guys!

At last but not the least, I would like to thank my parents. My mom and dad are very influential on my life and way of thinking. They have always been my role models, and I have always tried to be like them. They have inspired me, motivated me and have done whatever they could to support me and show

me their love and affection. My parents' sacrifices are in epic scales. I will never be able to pay them back. I guess this thesis will make them a little bit less disappointed in me! Finally, I want to thank my family in law. They were always understanding and supportive of us.

Cheers to new challenges!

Pouya Mehrdel

In loving memory of my sweet grandmother who

passed away during the writing of this thesis…

May her soul rest in peace…

Table of Contents

i. Abstract

Over the past decade, microfluidic technology has proven its capabilities to start bringing detection and quantification capacities to novel miniaturized devices. The current generation of microfluidic platforms provide great precision in detection and quantification. At the same time, they have started to evolve towards self-sufficient (stand-alone) setups. These platforms are relying less and less on external power sources and they use built-in detection and quantification methods to be flexible and mobile. Among the various Lab on a Chip (LOC) applications, micro–Total Analysis Systems (µTAS) and Point of Care Tests (POCT) are the pinnacles of microfluidic platforms. They are accurate, rapid, cost-effective, and user-friendly. They can monitor and measure compounds that were, previously, only detectable in state-of-the-art laboratories. This characteristic is quite important and vital, especially when it comes to human health status monitoring. Therefore, developing POCs and µTASs has been the center of attention for researchers in recent years.

To reduce the reliance of microfluidic platforms on external power sources and measuring instruments. There is the need to improve and enhance the microfluidic platforms, not only from the performance point-of-view but also from their manufacturability, to be able to batch produce them at lower costs.

Most microfluidic circuits detect or measure a compound and in the first step, they need to label/enhance a reaction, in other words, mix two or more components and then analyze the results based on the readout. This thesis proposes an enhancement of the performance of a key element in most µTAS and POC devices such as the micromixer, with the introduction of a geometrical expansion that increases the diffusion path without increasing the pressure loss. Afterwards, its performance is validated and the design has been used to quantify for the first time on a microfluidic platform the ionic strength of buffered and non-buffered solutions. Finally, and to avoid the need for syringe pumps, in the same quantification strategy, we have introduced paper as a substrate material and optimized the inlet geometry to enhance the performance of the novel microfluidic paper-diffusion-based sensor for ionic strength quantification. The proposed sensor was able to quantify the ionic strength of buffered and non-buffered solutions down to 0.1 M concentrations using Whatman 5 paper substrate.

Keywords: *Microfluidics; Microfabrication; Soft-lithography; 3D-printing; Micromixer; Diffusion assay; colorimetric detection; µTAS; µPAD; ionic strength measurement; pH measurement.*

ii. Abbreviations

LOC	Lab on a Chip
µTAS	microfluidic Total Analysis Systems
POCT	Point of Care Testing
µPAD	microfluidic Paper-based Analytical Devices
Re	Reynolds number
Pe	Peclet number
PDMS	Polydimethylsiloxane
St	Strouhal number
SL	Stereolithography
2PP	Two-photon polymerization
DLP	Digital Light Projection
SAR	Split and Recombine
LOD	Limit of Detection
EHD	Electro Hydrodynamic
EKI	Electro Kinetic Instability
AC	Alternate current
DC	Direct current
FEM	Finite Element Method
FVM	Finite Volume Method
RBC	Red Blood Cell
HIV	Human Immunodeficiency Virus
hCG	Human Chorionic Gonadotropin
HPV	human papillomavirus
ABS	Acrylonitrile butadiene styrene
PLA	Polylactic acid
FDM	Fused deposition modeling

iii. Figures captions

1. Introduction

1.1. The origins, importance and influence of microfluidics on human health

Since the dawn of civilization, humanity has always put effort to improve its welfare, security, and prosperity. But the humans comprehended that achieving sustained growth would be farfetched, without considering the importance of health and hygiene among citizens. There is no doubt that each society needs balance and harmony to function properly. However, if the citizens are harmed by poor health standards, it would be highly unlikely for the people to participate in activities that keep the society in harmony. Poor health and hygiene standards have never helped civilizations to achieve prosperity and glory. This fact was well realized by our ancestors. Numerous historical sites around the world support this idea. From the Roman aqueducts to Ottoman hammams (public baths) and Iranian subterranean channels. From ancient traditions in India of not polluting certain rivers to the well-established and regarded knowledge of medicinal plants in China. All of these show that not only the civilization, but the members of society have understood the importance of this fact and they have tried to respect health and hygiene.

Albeit, there are numerous examples of empires, civilizations, and even continents that have crumbled to dust, because of unforeseen health-related problems. The pandemic outbreak of bubonic plague, also known as the “Black-Death”, crippled the world and the European continent in particular. “Black Death” was so devastating that it took the life of one in every three Europeans and it took decades for them to recover from the consequences of the impact. Another example would be the Aztec empire, which turned into ashes because of the widespread outbreak of smallpox in the so-called “New World” by the conquistadors. Despite the impressive advancements in biological and technological fields, humans have shown vulnerability to diseases. The outbreak of the “Spanish Flu” in 1918, rang that alarm for the scholars and researchers. Further advances in biological and pharmaceutical studies, besides the spread of modern medicine in the non/less developed countries, improved the global health standards remarkably, but at the same time created an illusion of invincibility of the diseases for humans. The outspread of SARS (severe acute respiratory syndrome) in 2002, MERS (Middle East Respiratory Syndrome) in 2012, and the Ebola outbreak in West Africa in 2014 could be considered as a warning to the governments and health systems to review their policies and upgrade their facilities. However, the pandemic of COVID-19 caught the world off guard and resulted in a situation that was never seen before

in at least a century. The late pandemic resulted in tens of thousands of fatalities and it is believed to lead to a drastic economic recession. COVID-19 showed the importance of early disease diagnosis and how it can affect the treatment and the subsequent management of the pandemic and economy. Precise early diagnosis not only provides higher chances of survival for the patients, but helps the authorities to monitor the contaminated areas better and enforce confinements, lockdowns, or limiting of transportation more effectively.

Microfluidics technology is one of the novel tools that now we have available to overcome these threads and improve our wellbeing.

This technology has been commonly used in the biological, biomedical, chemical, biochemical and pharmaceutical fields. Yet, over the past decade researchers have focused on developing accurate, rapid, small reagent use, and cost-efficient microfluidic total analysis systems (μTAS) and point of care test (POCT) devices that can be used in a wide range of applications: from food quality control to drug development, from soil pH monitoring to disease diagnosis and health monitoring. Although both μTAS and POCT devices have shown remarkable performance, the POCTs have received additional support due to their role in improving the treatment procedure and providing early diagnosis. POCTs are laboratories on microfluidic chips that can examine bodily fluids and present accurate results in a short time. They can provide bedside diagnosis, which results in accelerating the treatment procedure, lowering the diagnosis costs, and reducing the workload of the hospital laboratories. Furthermore, they can be used by the patients in order to monitor their health status at home continuously and diminish their need of hospitalization for routine tests.

Other than the microfluidics capabilities and the importance of health related investigations (in general), microfluidics has gathered the attention of entrepreneurs. Microfluidic products have obtained an eye-catching market size and it is believed that its market continue to grow by about 50% until 2025 (see Figure 1.1) [Yole development SA*]. Hence, focusing on microfluidic studies is not only influential on the general health status, but it is fruitful from the economic point of view.

* http://www.yole.fr/Status_Of_The_Microfluidics_Industry_Market_Update.aspx

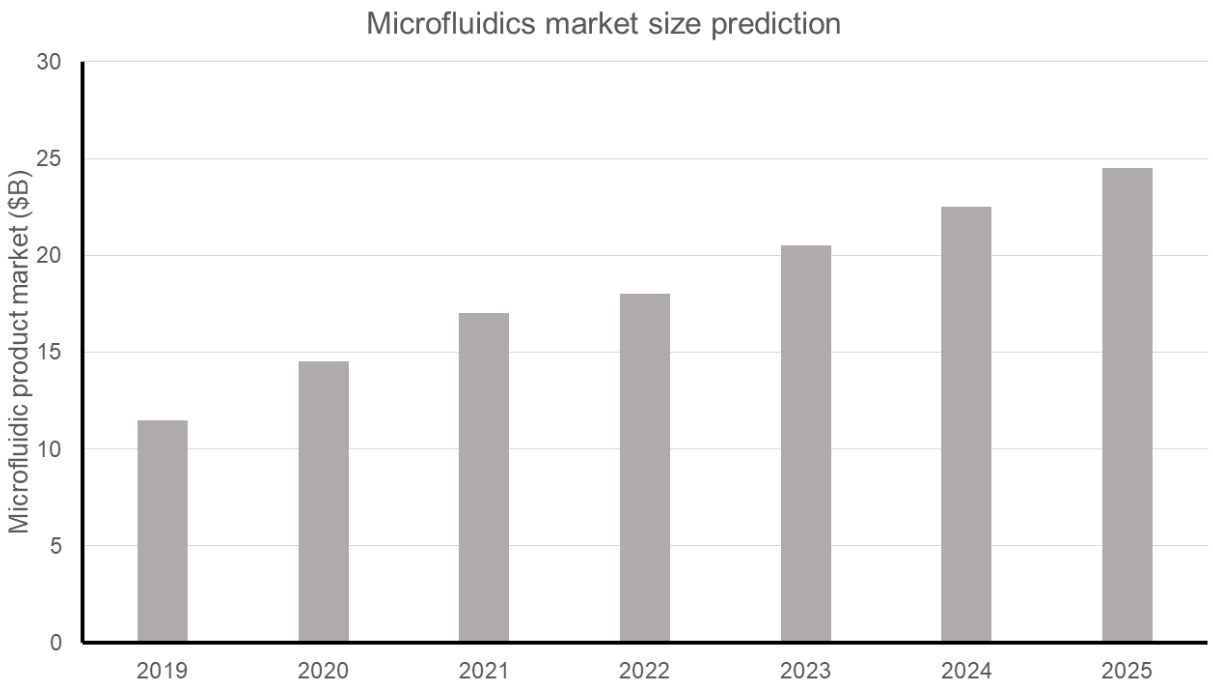

Figure 1.1 The prediction of microfluidic products market size [Yole Development SA].

It is worthy to mention that although all the advancement there has been counted commercial successes due to the complexity and interdisciplinarity of these devices, which is not only a challenge at the research level but it also becomes complex to overcome when there is a need to manufacture them in big batches. It is complex to find a scalable manufacturing process which is compatible with all the sensors or device parts. This issue can be addressed not only by taking advantage of miniaturization but also by introducing porous media features (such as Lab on Paper). This substrate material is often cost-efficient, omnipresent, does not require pumps and is biocompatible, which lead to the introduction of microfluidic Paper-based Analytical Devices (µPAD). These devices offer in situ analysis without requiring sophisticated detection instruments. As a result, they are often affordable, user-friendly, and more appropriate for being used in less developed regions. However, in most cases, they are only capable of providing yes or no type of results. One of the most well-known examples of µPAD is the pregnancy tests (hCG test).

1.2. Micro Total Analysis systems (µTAS) and Point-of-Care testing devices (POCTs)

Micro Total Analysis Systems or µTAS emerged from the integration of various microfluidic and sensing parts into a single setup. Today, the developed platforms are enjoying some remarkable features such as: low reagent requirement, precise detection and quantification, fast responsiveness, reliability and reproducibility of results, portability, and applicability to numerous fields of research.

Generally, µTASs consist of three main parts: separator, micromixer (also known as microreactor, synthesis chamber and so on), and the sensing part.

A separator is used in solutions where there is the need to remove unwanted compounds from the sample. The elimination of such compounds might be very crucial in some cases. For instance, one of the most important bodily fluids is blood. In this case, the presence of red blood cells (RBCs) restricts the utilization of optical sensing methods. Other than purification, the separation is also of interest, especially for biological and biomedical fields. Therefore, the purification/separation should be carefully studied in order to be applied to microfluidic assays [9].

The micromixer/microreactor/synthesis chamber is where the reagents interact with the detector/labeling solution. In case of the biomedical and biological applications, it is common to mix the solution of interest with another solution (biomarker, normally labelled) and track the variations. The preparation method is not limited only to the mixing of two or more solutions. It is possible to use nanoparticles (or often labels) and introduce them to the solution of interest and later monitor the nanoparticles/labels instead of the solution. In the case of the chemical and biochemical fields, the explanation is more straightforward and the term “micromixer/microreactor” is self-explanatory.

The purified and prepared solution should then be delivered to the sensing part and based on the properties of interest, appropriate strategies for the detection and quantification can be adopted.

As described earlier, microfluidic devices have a wide range of applications in multiple fields. For instance, crystallization [10], extraction process [11], polymerization, and organic synthesis applications are some examples of the chemical applications of microfluidic devices and µTASs.

Besides the chemical and biochemical applications, microfluidic platforms have been used extensively in biological and biomedical fields; varying from drug screening and discovery [12] to nucleic acid [13–15], protein [16] and enzyme analysis [17].

After developing and defining the µTAS devices, researchers started to benefit from the µTAS advantages in favor of disease and health state diagnosis. They noticed that the proposed device should be affordable, portable, stand-alone, accurate and user-friendly. Defining the characteristics of such microfluidic devices led to the introduction of Point of Care Testing systems (POCTs). In other words, POCTs are basically µTASs focused on health diagnosis or diagnosis in general.

One of the first commercial successes of the POCT device is the glucometer, which helps the patients with diabetes to monitor their glucose level in blood.

The integration of new detection methods with POCTs has dramatically expanded the application field of the POCTs. They are now being used for the diagnosis of many diseases. For instance, Malaria [18–20], HIV [21,22], HPV [23–25], Dengue and Ebola virus [26,27], Mycobacterium tuberculosis [28], Zika virus [29] and antibodies of certain other illnesses [30–33].

1.3. Micromixers

One of the key elements in POCT or µTAS system is the mixer. This section will introduce the distinct types of micromixers, the different methods of fabrication and several examples of applications.

1.3.1. Micromixer types

1.3.1.1. Passive micromixers

Passive micromixers do not rely on external energy sources for disturbing the flow in order to achieve a uniform mixture of fluids. These micromixers mainly rely on molecular diffusion or chaotic advection for the species dispersion. Achieving a decent mixing would only be possible by enhancing the contact surface between the solutions and taking advantage of geometrical features in the design.

1.3.1.1.1. Lamination based micromixers

In these micromixers, solutions enter through the inlets and flow parallel to each other in the main channel achieving mixing through diffusion mainly, therefore they are called Lamination based. The most common lamination-based micromixers are T (Figure 1.2 a) and Y (Figure 1.2 b) mixers, which have two inlets and the inlets merge to each other to create a single channel. Although these micromixers are easy

to fabricate and use, they require a significant mixing length to perform well. There have been trials to reduce the mixing length by causing secondary flows or vortices within the channel. For instance, Wang et al. [34] modified the T-mixer by placing a diamond-shaped step at the meeting point of inlets. The proposed step caused a disturbance to the flow at a Reynolds regime of 400 to 500 and improved the mixing efficiency. In another study, Hsieh et al. [35] investigated the effect of the inlet angle in Y-mixers on the fluids mixing and showed that if the inlets are positioned at 60° (with respect to the main channel), the mixing length could be reduced significantly. Hong et al. [36] induced chaotic advection in the flow by benefitting from a two-dimensional Tesla configuration (a modification in the main channel that separates a layer of fluid and reintroduces it further back to the flow), and Yang et al. [37], took the Tesla configuration (see Figure 1.2 f) to the third dimension and reported reasonable mixing efficiency for $0.1 < Re < 100$ regimes.

The aforementioned micromixers are clever approaches to address the low mixing efficiencies in T/Y mixers. But it should be noted that vortices and secondary flows do not usually occur at Reynolds regimes smaller than 60. Therefore, using such mixers (especially in biological and biochemical fields) is extremely limited, due to high shear stresses that generated between fluid layers, which could fatally damage cells or even rapture them.

One of the main advantages of T/Y mixers is their two-dimensional geometry and the possibility of fabricating them via conventional soft-lithography methods. Using three-dimensional features eliminates this advantage and complicates the fabrication of the proposed micromixer.

Additionally, it is worth mentioning that all the other passive micromixer types are derivations of the lamination method. However, the continuous progress of the derivative methods (which are described in the following sections) has developed them to a level that they have branched from the lamination method and established their category.

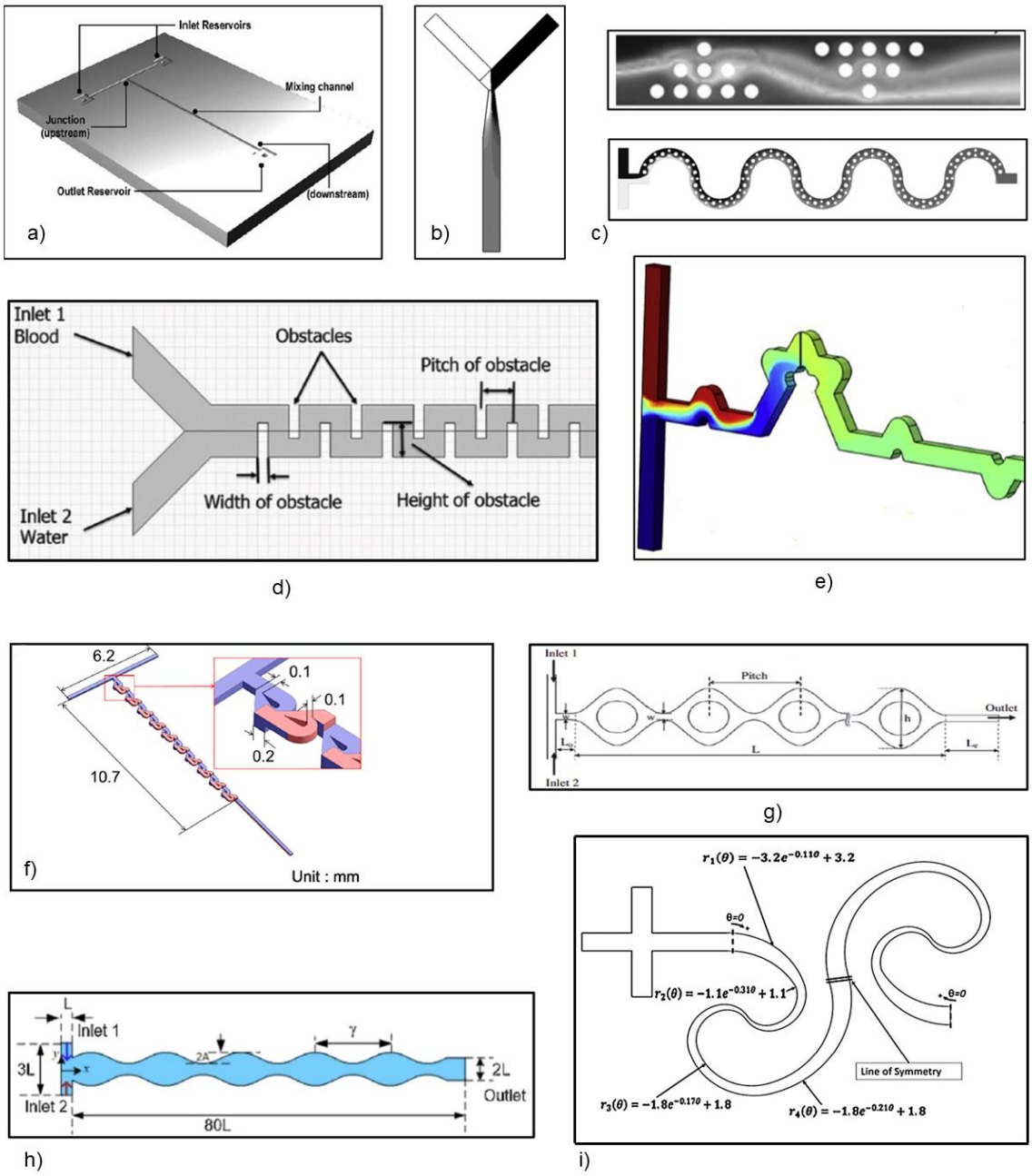

Figure 1.2 Different types of passive micromixers. a) T-mixer [34], b) Y-mixer with enhances inlets' intersection [38]*, c), d) and e) baffled channel micromixers* [39–42]*, f) Tesla micromixer* [43]*, g) Split and Recombine micromixer (SAR)* [44]*, h) Divergence-convergence based serpentine micromixer* [45]*, and i) curved channel micromixer* [46]*. All figures are reproduced with permission from [5,6].*

1.3.1.1.2. Obstacle based micromixers

This type of micromixers uses obstacles along the flow path rather than modifying the general shape of the main channel to enhance the flow disturbance and generate vortices. The obstacles are either

placed on the walls to affect the boundary layer and redirect the flow, or in the middle of the channel to disturb the flow in the main channel. Karthikeyan et al. [41] studied a T-mixer with rectangular obstacles on the walls and optimized the shape of the obstacles to study the influence on the mixing phenomenon. Milotin et al. [47] studied a micromixer with four inlets and a tube as the main channel. The inlets were oriented in a manner that the fluids would create a swirl as they entered the main channel. The mixing in the channel was enhanced by adding semicircular shaped obstacles. The study showed that the proposed micromixer could achieve 100% of efficiency at Reynolds 91 regime. In the case of the obstacles inside the channel, Wang et al. [39] studied the flow behavior in a T-mixer with different layouts of obstacles and reported that flow enters the turbulence state at only high Reynolds numbers. Alam et al. [40] developed a micromixer with reasonable performance at $0.1 < Re < 60$, which had cylindrical obstacles inside the channel.

In summary, most of the mentioned micromixers, such as split and recombine (SAR) (Figure 1.2 g)), split-joint, or even Tesla, are the T-micromixer with obstacles in their path. Sometimes these mixers adopt the divergence-convergence (Figure 1.2 h)) characteristic to increase their efficiency, but the foundation of their geometry is based on lamination and channel with obstacle methods [5].

Overall, the aforementioned micromixers are enhanced versions of the lamination method, but still, they rely on relatively high Reynolds numbers to perform at their full capacity. On the other hand, the introduction of obstacles increases the pressure drops and limits the applicability of these types of micromixers. Finally, the fabrication of such micromixers is not simple and requires sophisticated techniques. As a result, most of them are using 2D structures.

1.3.1.1.3. Divergence-convergence based micromixers

The main mixing parameter in these micromixers relies on expansion vortices, especially when the cross-section area increases dramatically. This method is generally combined with previous approaches. For instance, Mondal et al. [48] adopted an expansion and contraction strategy to a T-mixer and proposed a micromixer with wavy/sinusoidal walls (similar to Figure 1.2 h). They showed that the mixer provided improved results compared to the conventional T-mixer. Afzal and Kim [49] studied the mixing phenomenon in a T-mixer with expansion and contraction parts and a circular obstacle in the middle of the modified sections. They showed that, at $10 < Re < 70$ flow regime, the mixing quality highly depends on the contraction part and the smallest cross-section of the channel rather than other parameters. Expansion vortices grew significantly when flow velocity was high and channel width was narrow.

Similar to previous micromixer models, this method requires a precise fabrication process. Moreover, the generation of expansion vortices requires flows at high Reynolds regimes, which is not compatible with most of the biological applications.

1.3.1.1.4. Curved channel micromixers

The main drawback of the T and Y mixers is their requirement of significant mixing length, especially at lower Reynolds number regimes (0.5 < Re < 10). Such a requirement leads to an increase in the size of the microfluidic device, which conflicts with the fundamental idea of miniaturization in microfluidic devices. This method optimizes the ratio of channel length to the occupied space by applying the spiral or sinusoidal architecture to the micromixer. Scherr et al. [46] designed and evaluated a spiral micromixer with logarithmic curvatures. They showed that the mixer was able to generate "Dean" vortices at Re 67 regime and to provide mixing efficiency of 86%. Sheu et al. [50] investigated a micromixer with three-consecutive quarter circle parts, which almost mimicked a split and recombine micromixer. They showed that the mixer could achieve reasonable efficiencies at high Reynolds number regimes (50 < Re) thanks to secondary flows. The fabrication of these micromixers is not as simple as the T/Y mixers. But at the same time, it is more facile than the baffled or divergence-convergence micromixers. Moreover, the pressure drop of these designs is only slightly higher than the T/Y mixers, since there are no obstacles on the flow path. However, careful efforts should be made to make sure that the pressure drop is not sacrificed for the performance. Table 1.1 presents a brief overview of the studied passive micromixers with respect to the working range (Re), Peclet number and provided mixing efficiency.

Table 1.1 Passive mixers Mixing Efficiency and Flow Regime

Characteristics	Re	Pe	Mixing efficiency	Material
T-mixer (blue dye and colorless liquid) [34]	500	7e5	83%	Silicon/pyrex glass
Split-join/fluorescein dissolved into two different buffers [51]	0.05	50	97%	Mylar
H-shape/colored water solutions [52]	0.08-4.16	n/r	98%	Plexiglass
Reverse-staggered herringbone in channel [53]	0.01-100	34.4-34400	n/r	PDMS
Sinusoidal side walls [54]	0.2-75	n/r	90%	Plexiglass
Unbalanced SAR [55]	Re ≥ 20 Re ≥ 50	n/r	86% 95%	PDMS
Two layers of spiral channels overlapped together [56]	8-40	n/r	90%	Glass

It should be noted that most of the micromixers introduced in Table 1.1 either rely on Reynolds number higher than 50 or on sophisticated geometries/fabrication techniques to provide homogeneous mixtures.

1.3.1.2. Active micromixers

These micromixers mainly rely on external energy sources for reinforcing the mixing in the microchannels (Figure 1.3). The use of external sources not only improves the mixing efficiency, but also decreases the mixing length, remarkably [5]. However, employing such methods with the microfluidic platforms increases the complexity of the device and in some cases, for instance when using electromagnetic driven flows, it could be incompatible with certain biological fluids. Thus, careful considerations should be taken to make sure that choosing such active micromixers does not jeopardize the analysis.

1.3.1.2.1. Pressure driven micromixers

This type of micromixer depends on velocity fluctuations for enhancing the mixing phenomenon. Unlike the passive micromixers, the flow velocity and profile are in transient regime and the contact surface and consequently the mixing process are influenced by the fluctuations. The flow velocity (in other words; the discharge) can experience a sinusoidal trend in its magnitude. Also, the fluid might experience a stop and go (step) function, which creates a pulsatile flow. Therefore, in both cases, the diffusion is accompanied by occasional vortices and results in an improved mixing. For instance, Wu et al. [57] designed a micromixer with a circular mixing chamber and an oscillator. They investigated the effect of pulsatile flow on the mixing quality. They showed that by taking advantage of four mixing chambers and an oscillator, the mixing efficiency could reach up to 97%. In another study, Li and Kim [58] introduced a micromixer that took advantage of water head pressure to create a pulsatile flow. They demonstrated that the micromixer could provide up to 90% of efficiency for flow-rates up to 20 µl/min.

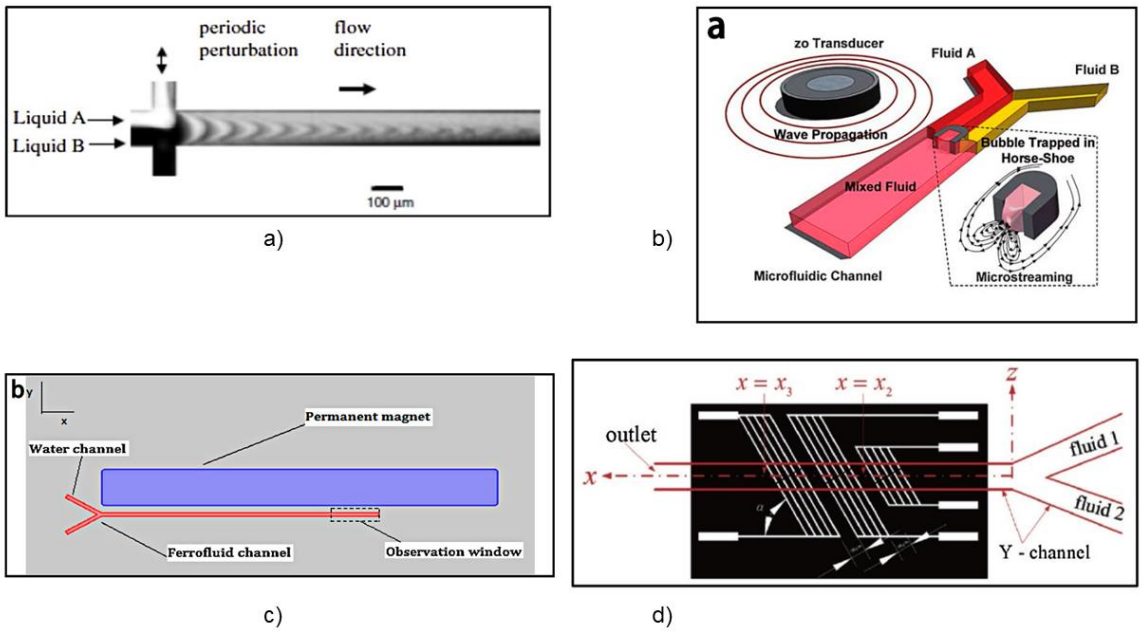

Figure 1.3 Different types of active micromixers. a) Pressure-driven micromixer [1]*, b) Acoustic field driven micromixer* [2]*, c) magnetic field driven micromixer* [3]*, and d) electric field driven micromixer* [4]*. All figures are reproduced with permission from* [5,6]*.*

1.3.1.2.2. Acoustic field-driven micromixer

The mixing phenomenon in some micromixers relies on the vibration of bubbles or fluid molecules. The bubbles might have been inserted into the microfluidic system intentionally or might have been caused by the excitation of the fluid molecules. Regardless of the origin of the bubbles, their vibration enhances the fluid dispersion in the channel. However, studies have shown that exceeding the 50 Hz frequency limit increases the fluid temperature and can result in creating an undesirable environment for biological applications [59,60]. Ahmed et al. [61] managed to generate an air bubble in a micromixer with a horseshoe pattern. Besides generating the air bubble, the proposed micromixer could produce high-quality mixtures in a laminar flow, thanks to the vibrations of the air bubble. Wang et al. [62] investigated the effect of the frequency range on the mixing efficiency. The study demonstrated that if the bubbles were generated within the 1-5 kHz frequency range, they could effectively improve the mixing efficiency.

The acoustic field-driven micromixers have been created using ultrasonic transducers [60,63], thin-film piezoelectric [64,65] and surface acoustic wave [66,67] transducers, as well. For instance, Yang et al. [60] benefitted from an ultrasonic transducer and developed a micromixer that could deliver

mixtures of high homogeneity. On the other hand, Luong et al. [68] developed a micromixer with reasonable performance based on a surface acoustic wave method.

In all the above-mentioned mixers, the mixing phenomenon depends on the perturbation of fluid due to the presence of an acoustic field. It should be noted that the applied shear stress on compounds within the fluids is also highly affected by the vibration. Considering both the thermal and shear stress limits, this method should be cautiously evaluated for the biological and biomedical fields.

1.3.1.2.3. Magnetic field driven micromixers

In this type of micromixers, the perturbation of fluid is usually caused by the effect of an induced magnetic field on certain magnetic particles. The magnetic field can be caused by permanent magnets [69–74], electromagnets [75–79], microstirrers [80–83] and/or integrated electrodes [84,85]. Ballard et al. [69] developed a micromixer based on the use of permanent magnets and rotating magnetic microbeads inside the channel. Fu et al. [75] investigated the mixing process of water and a ferrofluid by using an electromagnetic field (DC current), numerically and experimentally. Boroun and Larachi [78] studied the mixing efficiency under static, oscillating and rotating magnetic fields for magnetic and nanomagnetic fluids (water and iron nanoparticles- Fe^{+2} and Fe^{+3}) and demonstrated that the mixing efficiency was directly influenced by the intensity of the magnetic field.

Despite showing remarkable performance, it should be noted that some biological compounds (such as red blood cells) are sensitive to magnetic fields. Thus, utilizing such forces might compromise the assay.

1.3.1.2.4. Electric field driven micromixers

This type of micromixers is among the most well-studied and well-developed micromixers, due to their controllability, efficiency and, fast-responsiveness. Electric field driven micromixers can be categorized into two groups; Electro hydrodynamic (EHD) disturbance-based micromixers and Electrokinetic instability (EKI) based micromixers [5,86,87].

In the EHD micromixers, the mixing phenomena is carried out thanks to the different conductivity and permittivity of fluids. When the fluids are exposed to direct current (DC) or alternative current (AC) electric fields, the interface between the fluids is disturbed and as a result the mixing is enhanced [1,4,88]. El Moctar et al. [89] investigated the effect of applying DC and AC electric fields to a T-mixer and demonstrated that their proposed EHD micromixer can achieve a mixing quality of 80% in a fraction of a seconds (0.1 s). Nonetheless, it should be noted that this method requires fluids with equivalent density

and viscosity, but different electrical properties. This requirement limits the versatility of the EHD micromixers to many applications.

On the other hand, the mixing phenomena in the EKI micromixers is based upon the movement of fluid ions or particles toward a charged surface [90–95]. EKI mixing can be divided into electroosmosis [95–100], electrophoresis [101,102] and dielectrophoresis [103] categories. Usefian and Bayareh [104] took advantage of the electroosmosis method and proposed a mixer that could work either with AC or DC current. They showed that the DC current was more efficient in generating vortices than the AC current. Daghighi and Li [101] developed an electrophoresis micromixer by connecting a cylindrical chamber to straight channels. A conductive particle (disk) was placed in the middle of the channel. The induction of the electric field resulted in the creation of vortices around the disk and in an enhancement of the mixing performance. Deval et al. [105] studied the possibility to use non-conductive particles in the generation of chaotic vortices and showed that their proposed mixer was able to reduce the mixing time significantly.

In spite of remarkable mixing performance, the electric field driven micromixers are facing some serious limitations. First, the need for a power source might compromise the portability of the system. Second, the introduction of particles (conductive or nonconductive) might cause unwanted changes to the solutions. Finally, the induction of electric, magnetic or electromagnetic fields to the solution and the possibility of influencing the compounds within the solutions seriously limits the applicability of this method to biological, biochemical and chemical assays. Some examples of the developed active micromixers with respect to working range and provided mixing efficiency is demonstrated in Table 1.2.

Heretofore, the literature review showed that the passive micromixers does not require extensive external energy sources, but they lack the ideal performance, especially in biological ranges ($0.1<1$ Re <10). The passive micromixers that could provide significant mixing, either are performing at relatively high Reynolds number or are relying on sophisticated geometry, which would make their fabrication extremely challenging and also exceeds the biological limits on the applied shear stress (50 dynes/cm^2) and pressure drop [106]. On the other hand, the active micromixers are quite capable of providing homogeneous mixtures, but they rely on external energy sources that limits their “out of laboratory” applications. Also, active micromixers (depending on the type) are not always compatible with all the biological compounds and careful consideration (in choosing the type of active micromixer) should be taken.

Table 1.2 A summary of performance and working conditions of active micromixers.

Characteristics	Re	Frequency [kHz]/ Magnetic field strength [G]	Mixing efficiency	Material
Time-pulsed flow [107]	0.002-0.01	0-1 e-3 kHz	53%-82%	PDMS
Multi-bubbled based [108]	0..01	1-5 kHz	93%	PDMS
Surface acoustic wave driven [68]	≈ 0	220-260 kHz	45%	n/r
Permanent parallel magnet [72]	n/r	1750-2500 GHz	88%	PDMS
EHD perpendicular electrode array [89]	0.0174	0.05-100 e-3 kHz	81%	Lexan
Array of rotating magnetic microbeads [83]	n/r	n/r	72%	NiFe
Turbulence mimicking electroosmotic mixer [99]	Re ≤ 1	0.001 – 10 kHz	n/r	Transparent acrylic

With respect to the aforementioned points, in this thesis, we focus on developing a micromixer that is specifically designed to work in physiological range (0.1<1 Re <10) and generate the minimum amount of pressure drop. Also, the micromixer should be versatile towards various fabrication methods and also be adaptable in different POCT, µTAS and LOC platforms (please see Figure 1.4). Computational Fluid Dynamics simulation models will be developed to understand the fluid flow and mixing phenomena and how the geometry and materials enhance this process. These models will be used to optimize the micromixer's performance in biological applications. Finally, the portability and functionality of microfluidic platforms based on the developed methodologies will be studied after optimization, and different fabrication methods will be evaluated to enhance the performance of the proposed platforms.

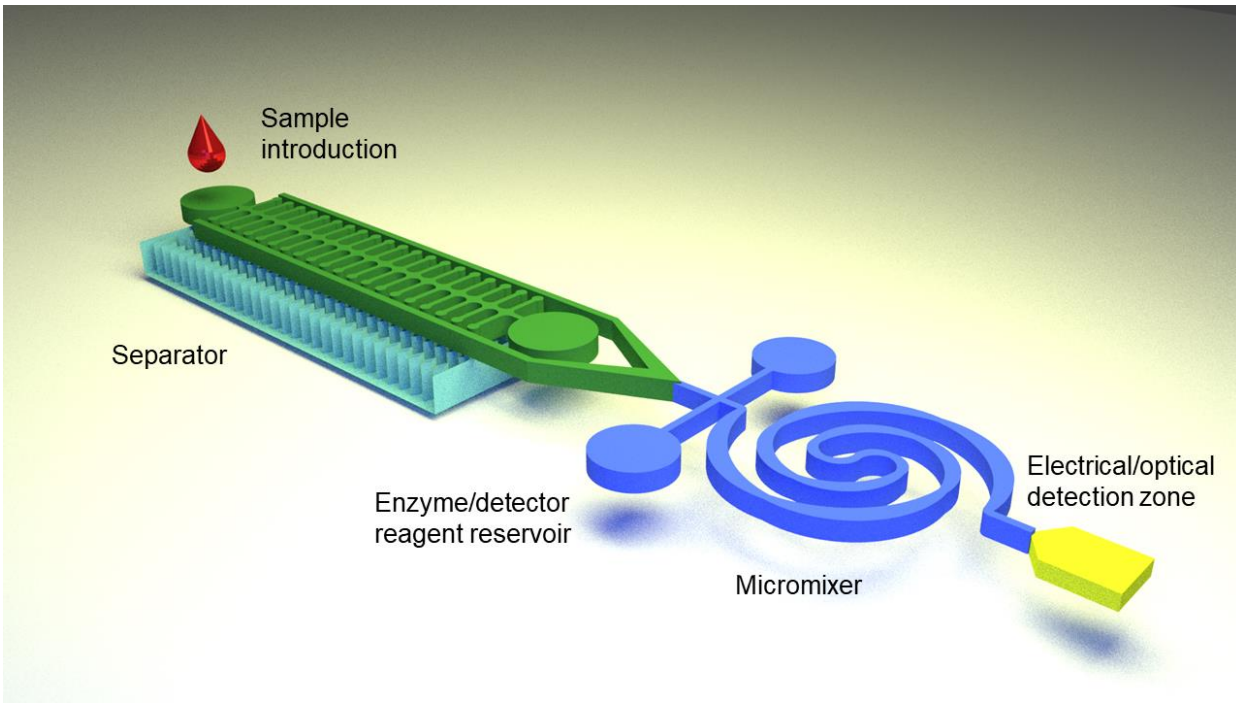

Figure 1.4 A schematic view of the conceptualized microfluidic sensor.

1.4. Conventional fabrication methods

This section introduces current routine technologies available to manufacture microfluidic chips. Special emphasis will be given to those methodologies that can be rapidly adopted for commercial manufacturing of the proposed designs.

1.4.1. Laminates

The need of a low cost method to build the microfluidic devices at an industrial level has further developed the use of adhesive layers as building materials. The cost efficiency and low-demanding nature of this process has gathered the attention of researchers and now is widely known as Laminates. In this method, a microfluidic platform is divided into separate layers. Each layer represents a specific part of the microfluidic device. For instance, the simplest microfluidic platform consists of three layers; a bottom part or support, a channel part, and a ceiling part or cover. Basically, the channel's pattern is cut in the channel layer (middle layer) and later the support and cover layers are stacked and bonded, creating a microfluidic device [8].

The laminates fabrication process and its precision heavily depends on the selection of the material, the cutting process of the pattern (in each layer if there is multilevel microfluidic platform) and the bonding process of the layers.

There is a broad range of materials with great optical features that can be used as layers. Adhesive transfer tapes [109], polymer layers (PMMA and COC) [110], and glass slides are examples of the previously used materials in this method. The main advantage is that there is no necessity to make sure that all the layers are of the same material. In other words, this method offers a wide configuration range of materials to the researchers, so the devices can be developed based on the requirements.

The pattern can be cut in layers by either a knife plotter or a laser cutter (usually CO_2 laser) [111]. Although the quality of the cut depends on the material and the cutting instrument. Several reports claim that laser cutting is more precise [112]. Besides precision, laser cutting is versatile towards a wide range of materials; Adhesive tapes [111], paper sheets (such as Whatman chromatography paper) [112], polymer layers and glass layers [8].

Similar to the cutting process, the bonding step depends on the selected materials, as well. Nevertheless, two bonding methods have been used commonly for all the materials; adhesives and thermal bonding. Adhesives bonding is achieved by using a double-sided tape as either the channel layer or as an excessive layer that holds two successive layers together. On the other hand, in thermal bonding, the temperature of each layer is increased to its glass transition temperature. Then the layers are overlapped and pressure is applied. By letting the parts cool down, the layers merge where contacted and form an individual block [110,113].

This method is quite straightforward and cost-efficient. But since most of the steps (specially bonding) are handled manually, this method suffers from high human errors and is time consuming. Errors such as bubble entrapment, poor alignment of layers, poor bonding, and deformation (especially in the thermal bonding) are common in this method.

1.4.2. Mold manufacturing for soft-lithography or hot embossing techniques

Several micro-manufacturing methods require a first step, which is the creation of a pattern or mold. This pattern of the microfluidic device is created on a solid substrate (usually a glass slide or a silicon or glass wafer). Afterwards, a photoresin (usually SU8) is hardened according to the mask pattern using UV light. The fabricated mold is later used to cast a polymer – usually PDMS: Polydimethylsiloxane- (soft-

lithography) or to stamp the pattern (hot embossing) for creating the microchannels. This method is more accurate compared to laminates, but on the other hand it is more laborious. Moreover, fabricating channels with three dimensional features is quite complex in this method [114].

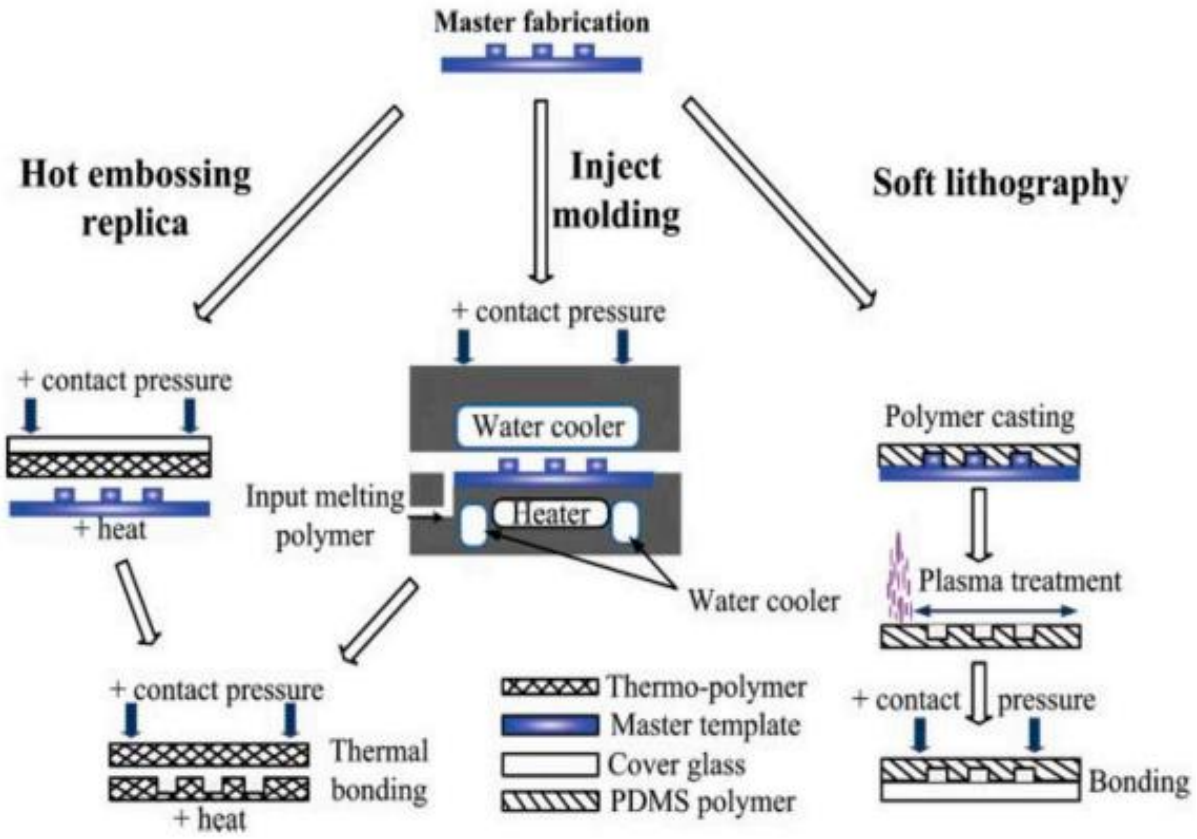

Figure 1.5 An illustration of different molding fabrication methods used for microfluidics [7]*. Figure is reproduced with permission from* [8]*.*

1.4.2.1. Soft-lithography

Soft-lithography is one of the most well established and developed fabrication processes and it is considered as the backbone of microfabrication. The current format of soft-lithography was first introduced by Whitesides [115] in 2007 and requires a first step, which is the creation of a pattern or mold. This pattern of the microfluidic device is created on a solid substrate (usually a glass slide or a silicon or glass wafer). Afterwards, a photoresin (usually SU-8) is hardened according to the mask that has the pattern using UV light. The fabricated mold is later used to cast a silicone (generally PMDS). The casted PDMS is then removed from the mold and is treated with oxygen-plasma (see Figure 1.6 B). Treating the

surface of the PDMS (via oxygen plasma method) activates the hydroxyl (OH^-) groups on the surface and results in a strong (Si-O-Si) covalent bond between the silicon atoms of the PDMS and the glass [115,116].

Although this method offers repeatability and precision in microfabrication, it is laborious and therefore more expensive than the Laminates method. Moreover, creating microchannels with 3D features is extremely challenging via this method and therefore, mostly 2D structures are fabricated through soft-lithography [114]. This is why soft-lithography is normally used in research labs but it is not well accepted for commercialization of the micro devices.

1.4.2.2. Hot Embossing

Even though it requires the manufacturing of a mold as in soft-lithography, this sub-method uses thermoplastics as building material. Therefore, since thermoplastics are commonly used in conventional plastic injection parts, this procedure is normally selected to bring the products to the market.

In this method the mold is heated and a layer of thermoplastic is compressed to the hot mold. As a result, the thermoplastic is melted and adopts the geometrical features of the mold. Finally, the modified part is bonded to a featureless substrate to form the microfluidic device. The common thermoplastics used in this method are polycarbonate, polymethylmethacrylate, cyclic olefin copolymer, and polyethylene terephthalate [117]. If the mold is done using lithographic techniques, an acceptable resolution can be achieved but the durability of the mold is limited. If the mold is micromachined it increases its durability but its dimensional range increases considerably (minimum features around to 500 um and higher).

1.4.2.2. Injection Molding

There are some attempts to create parts by conventional injection molding. However, the mold manufacturing process suffers from the same limitations as previously mentioned in hot embossing. Certain attempts have been made to micromachine molds [118], but assembling the parts still needs a further bonding step.

Briefly in this method, the thermoplastic is melted and conserved in a compressible chamber. Then, the two halves of the mold are joined to create a cavity. Later, the melted thermoplastic is injected into the cavity. Overtime, the thermoplastic cools down and solidifies. Finally, the casts are removed and the plastic part is formed by the microchannel pattern. This part is later bonded to a featureless substrate to create the microfluidic platform.

1.4.3. 3D printing

Compared to other methods, 3D printing is the newest one. This method can be categorized into different techniques. Each technique offers a unique precision, wide range of materials to be used and a special flexibility and capability in creating 3D features in microchannels. These are the leading advantages of this method, however this method is more limited in creating the feature size in state of the art patterns. Current patterns usually benefit from features in the range of 100 µm to 500 µm.

1.4.3.1. Fused Deposition modeling

Fused deposition modeling or FDM is an extrusion-based printing technique. In this method each layer is printed on top of the previous layer by a nozzle. The nozzle melts the printing material and extrudes it on the printing zone with respect to the introduced model and the previous layer. As the melted materials are printed, it is fused into the previous layer and over time it is solidified. The common materials used in this technique are acrylonitrile butadiene styrene (ABS), PLA, polycarbonate, polyamide, and polystyrene [119,120]. Initial attempts have been done to use this technique in microfluidics, but the resolution is too low to achieve successful devices.

1.4.3.2. Stereolithography (SL)

This method relies on the polymerization of resin due to being exposed to UV light. The exposure of UV can be a focused beam of LED laser (SLA method) or can be the emission of the whole pattern on the surface (DLP – digital light projection). Unlike the SLA method, where the printing is carried out spot by spot, the DLP prints the pattern layer by layer. With respect to the described points, this method requires photosensitive polymerizable resin as the printing material, but the resolution is improved and several devices have been successfully built using this technology (see Figure 1.6 A) [8].

1.4.3.3. Multi jet modeling

This method benefits from the same strategy as the stereolithography for printing the structures. However, instead of coating the surface with resin, the inkjet printhead injects a small volume of the resin onto the surface. The UV light source is mounted on the printhead and beams at the zone of interest to create the whole pattern [121,122].

1.4.3.4. Two-photon polymerization (2PP)

This method is the most precise, yet the most expensive printing method. The material used in photon polymerization requires the absorption of a certain wavelength of photon to be polymerized. In the 2PP method, the material requires the simultaneous absorption of two photons. Meaning that it

would be possible to print structures and patterns within an object, if the light is exposed from two perpendicular planes [123].

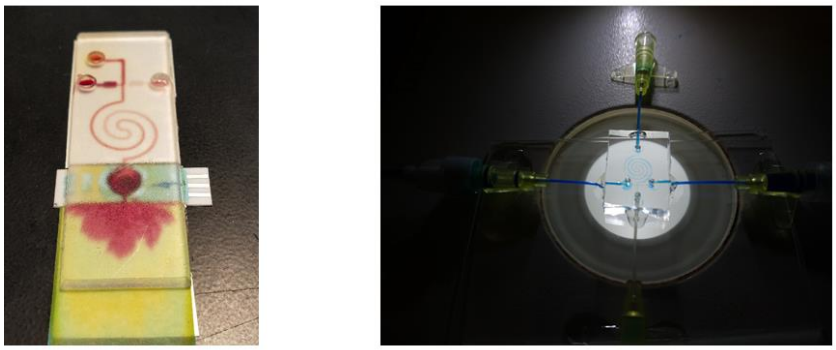

A) B)

Figure 1.6 Examples of microfluidic devices fabricated through different methods. A) 3D printed microfluidic platform versus b) soft-lithography fabricated micromixer.

1.5. Objectives

According to the limitations of the current state of art microfluidic platforms, especially with embedded micromixers and diffusion based-sensors, where there is a lack of easy to manufacture micromixers, operating at low Reynolds numbers (Re 0.1 to 10.0) without external energy sources to develop efficient diffusion-based sensors. This thesis focuses on answering the following questions:

1. Is it possible to introduce a 2D micromixer with optimal performance at biological ranges (Re 0.1 to 10.0), with minimal reliance on external energy sources and with low/minimized pressure drop?
2. Is the micromixer flexible in its fabrication method?
3. Is it possible to use the micromixer as a sensor to detect and quantify the ionic strength and pH of buffered or non-buffered solutions?
4. Is the established detection and quantification method applicable to paper-based microfluidics?
5. Is it possible to use fluids with different properties in a single porous media and achieve an adequate accuracy to develop sensors for biological/agri-food applications?
6. Is it possible to develop a computational fluid dynamic (CFD) model capable to reproduce diffusion phenomenon in porous media and use it for enhancing the performance of the micromixer/sensor, just by modifying the geometry?

2. Introducing the geometries and fabrication methods

This chapter initially presents the geometries of the developed microfluidic platforms. Later, it focuses on the utilized fabrication methods; Soft lithography, 3D-printing and laser cutting.

2.1. Introducing the geometries

2.1.1. Micromixer geometry

The proposed new design of mixer structure should be simple without separation and recombination or obstacles in the flow path and at the same time should not rely on external energy sources to achieve mixing, such as induced vibration or fluctuated flow, to facilitate the manufacturability and its versatility. A three inlet geometry is chosen for future implementation of a self-referencing sensor. To meet these requirements, the chosen design incorporated a cross-shaped inlet with a spiral architecture channel, to take advantage of two diffusion surfaces instead of one in the same real-estate area (please see Figure 2.1). Cross-shaped inlets (or having three inlets in total) is more efficient compared to two inlet geometries, since cross-shaped inlets take advantage of diffusion into two diffusion areas. Besides, this characteristic allows the implementation of self-referencing sensors based on this geometry: on one side the diffusion of the known substance can be measured and compared to the other side. In such systems the reagent that is injected through the middle inlet can either have lower or higher concentration of species than the surrounding reagents. Therefore, it would experience the diffusion twice the conventional T or Y mixers.

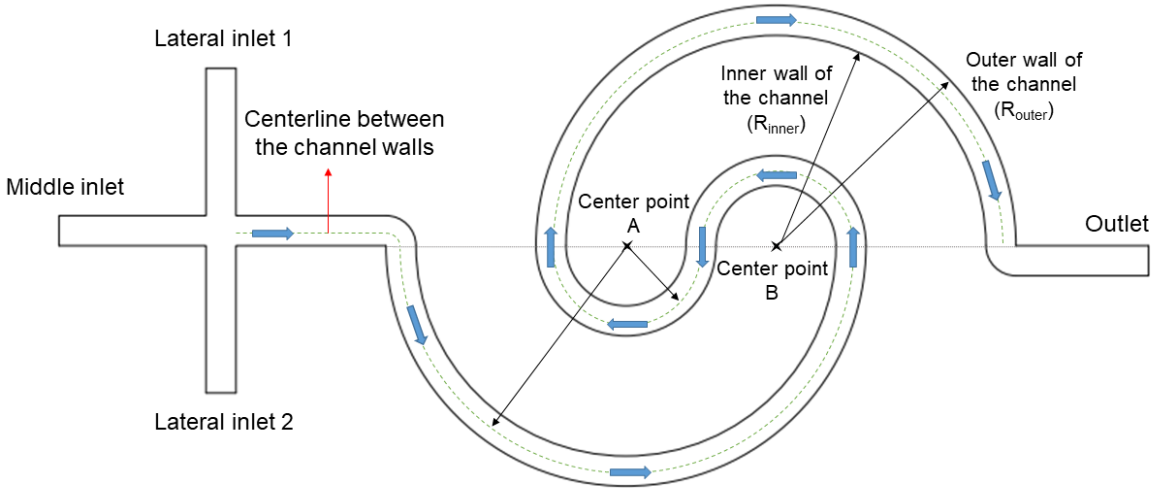

Figure 2.1 The geometry of a one loop spiral micromixer.

The micromixer also benefited from spiral architecture, which provides the minimum real-estate area for the maximum length of diffusion. For achieving this, it was first decided to presume a guiding line (hereinafter; "centerline") right after the inlets' intersection, see Figure 2.1. This line exactly began at the middle of the intersection and continued in the same direction as the middle inlet for 1 mm. In the meantime, two points of A and B were defined in the same path as the centerline. The distance between these points is constant and equal to 1 mm. However, the position of these points relied on the number of loops that were going to be assigned to the micromixer (Please see Table 2.1). For instance, for the 1 loop micromixer, point A and B were located at 1.6 and 2.6 mm of the drawn centerline. Whereas, in the three loops micromixer these points were positioned at 3.6 and 4.6 mm of the initial centerline. After defining the points, the centerline entered an arc of 180° around the point A. After completing the arc, centerline entered another arc of 180° around the point B. By following this procedure, the arc's radius decreased up to a point that it ended at the exact midpoint between points A and B. After that, the arc's radius increased. This process was halted when the arc's radius reached the same value as the first arc. Then the centerline exited the loop and continued towards the outlet. The channel width was defined to be 200 µm for manufacturability reasons.

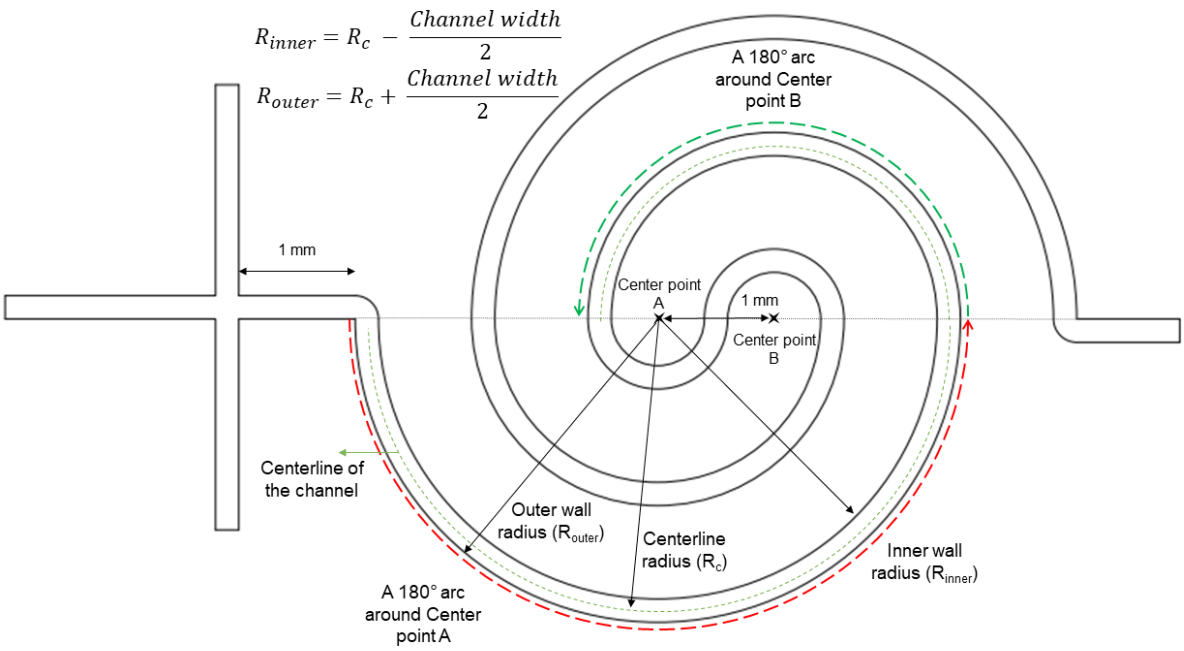

Figure 2.2 The geometry of a two loops micromixer. The 180° arcs around center points A and B are illustrated with red and green dashed lines, respectively. The equations for calculating the radius of inner and outer walls are also displayed in the figure.

A key feature in a diffusion-based mixer is the diffusion length or the line across which the diffusion is produced, see Figure 2.2. To enhance this diffusion length using the same real-estate a successive expansion and contraction part was added and therefore the mixing is enhanced while decreasing the difficulties in manufacturing the device since the channel itself became wider. Figure 2.3 shows the minimum width of the channel (200 um) at 0, π/2, π and 3π/2 positions.

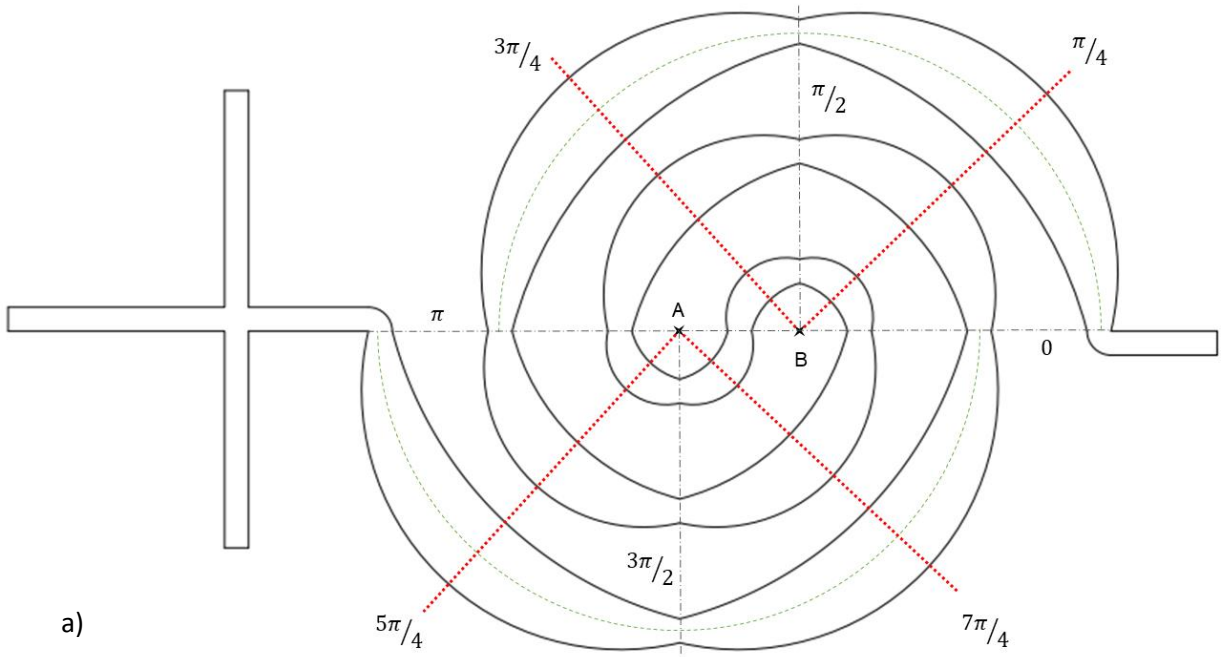

a)

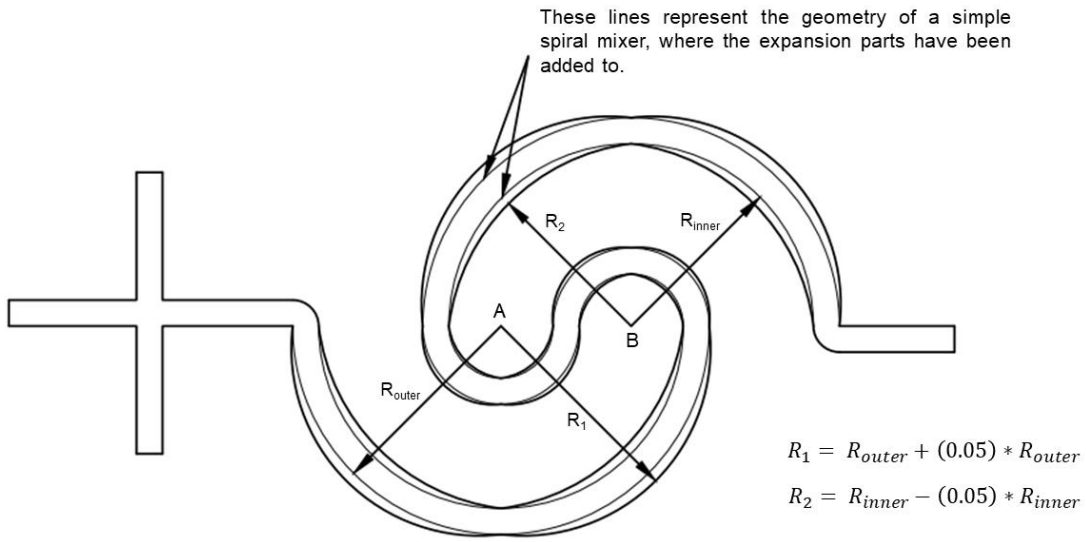

b)

Figure 2.3 The modified geometry of the spiral micromixers are illustrated. a) Shows the placement of maximum channel width on the geometry. b) Demonstrates the differences between the original spiral geometry and the modified geometry.

At the π/4, 3π/4, 5π/4 and 7π/4 positions the outer radius was calculated according to Eq. 2.1 and the inner radius according to Eq. 2.2. The increase of curvature is called expansion and contraction and

we proposed at two levels: 5% and 10%. Equations 2.3 and 2.4 incorporate the expansion and contraction ratio (E), that affect the width of the channel.

$$R_{outer} = R_{centerline} + \frac{Width\ of\ the\ channel}{2} \quad \text{Eq. 2.1}$$

$$R_{inner} = R_{centerline} - \frac{Width\ of\ the\ channel}{2} \quad \text{Eq. 2.2}$$

$$R_1 = R_{outer} + E * R_{outer} \quad \text{Eq. 2.3}$$

$$R_2 = R_{inner} - E * R_{inner} \quad \text{Eq. 2.4}$$

Following this approach, 3 types of micromixer classes were defined. Namely; one loop, two loops and three loops micromixers. Then, three modifications of 0%, 5% and 10% of expansion and contraction were applied to each class of micromixers. Resulting in having nine micromixers in total.

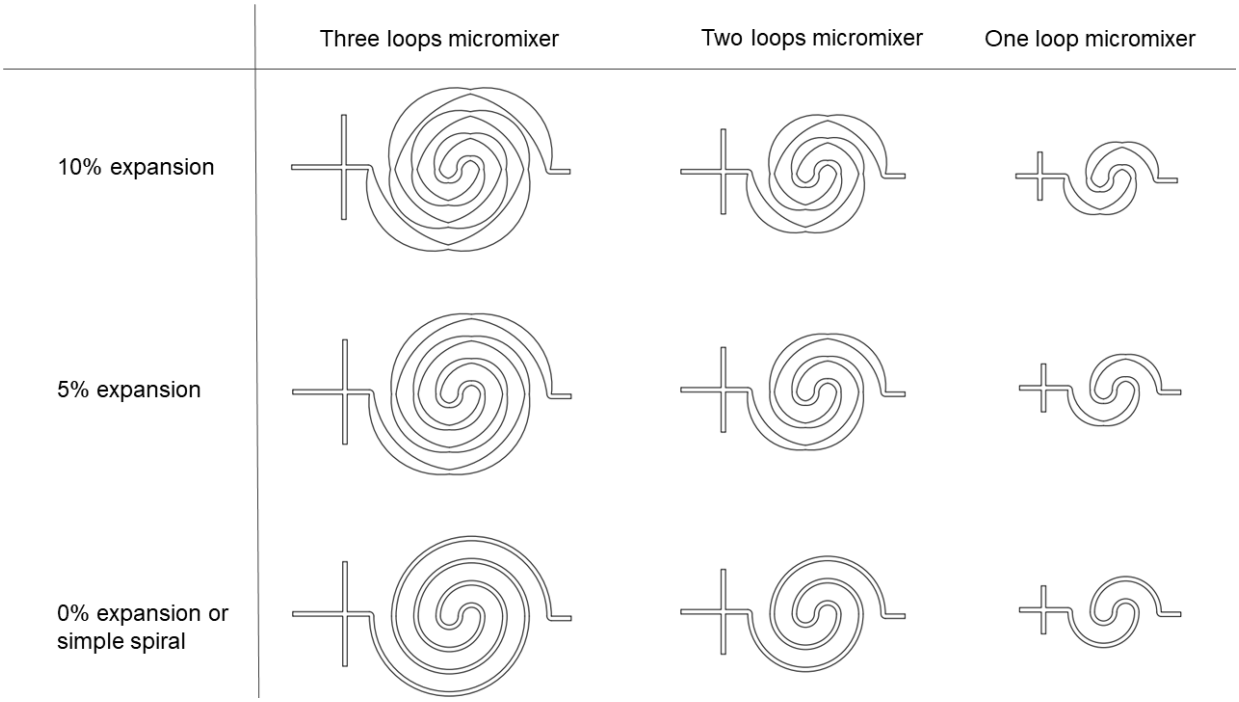

Figure 2.4 The designed and studied spiral micromixers.

The geometrical details of the designs are mentioned in Table 2.1.

Table 2.1 Maximum channel width and the position of Center points A and B with respect to the model.

Micromixer type		Distance from the center point A to the inlets' intersection [mm]	Distance from the center point B to the inlets' intersection [mm]	Maximum channel width [mm]
One loop	0%	1.6	2.6	0.2
	5%	1.6	2.6	0.35
	10%	1.6	2.6	0.5
Two loops	0%	2.6	3.6	0.2
	5%	2.6	3.6	0.45
	10%	2.6	3.6	0.7
Three loops	0%	3.6	4.6	0.2
	5%	3.6	4.6	0.55
	10%	3.6	4.6	0.9

2.1.1.1. Fabrication of the novel micromixer

This method had been considered as the standard procedure for the fabrication of microfluidic platforms from the dawn of microfluidic technology. There are numerous resources that have described this method and its different variations in details [115]. Briefly in this thesis, a negative film of the geometry of the desired microfluidic platform was prepared. Then, a microscopic glass was coated with photoresist SU-8 GM1060 (thickness of 5-27 µm, bought from @GERSTELTEC SARL). The glass was then spun at a 1080 rpm for 40 seconds to make sure that the SU-8 height is 25 µm, according to the manufacturer's instruction. Later, it was exposed to UV light. Exposure to the UV light plus sinking the microscopic slide in the SU-8 developer (PGMEA- Propylene glycol methyl ether acetate-, bought from @GERSTELTEC SARL) produced a coated SU-8 pattern within the microfluidic design's geometry. Therefore, when the microscopic slide was washed with isopropanol the microfluidic pattern remained on the slide and the unexposed areas were removed. Resulting in a mold of the pattern with a height of 25 µm.

After preparing the mold it was time to prepare the microfluidic device. For this purpose, a 10:1 mixture of silicon elastomer of SYLGARD 184 (bought from @Dow corning) and its curing agent was prepared. The microscopic slide was put in a curing box, which fitted the slide perfectly, and the mixture was added to the box. Then, the box was heated to make sure that the mixture was cured. After removing

the cured PDMS from the mold and the connections were created. Finally, the cured PDMS block was bonded (via O_2 plasma treatment) to a blank microscopic slide.

Soft lithography has proved its capabilities in fabricating high resolution microfluidic geometries. However, the complicated and laborious procedure and the emergence of new technologies, such as 3D printing, have reduced the reliance on this technique.

2.1.2. The geometry of the 3D-printed pH and ionic strength sensor and its fabrication method

The proposed geometry was validated as a pH and ion strength diffusion-based sensor, please refer to Paper B [124]. The manufacturability of the proposed pH and ionic strength microfluidic sensor was evaluated, besides investigating the applications of the studied platform. The sensor, which initially was manufactured by soft-lithography, was also manufactured by DLP 3D printing techniques which are more time and cost efficient.

2.1.2.1. Fabrication process of the 3D-printed pH and ionic strength sensor

The 3D printing method can be categorized into numerous techniques. However, the Digital Light Projection technique (DLP) has shown impressive performance regarding the fabrication of the microfluidic devices [125,126]. In the DLP method, the model is sliced up to numerous layers. The printer exposes the layers to the UV beam, successively. Therefore, the resin (or any other appropriate material) is hardened where exposed and remains unchanged in the other areas. Fabrication process began by creating a 3D model of the desired platform in the Solidworks software. Then, the produced model was exported in the .STL format and uploaded to the 3D printer's (Miicraft plus) software. The uploaded file was sliced to 50 µm layers by the built-in Miislicer software. Due to the dependency of the printing setup on the complexity of geometry and the utilized resin (Miicraft BV-007 (clear)), there is not a universal protocol for the printing devices. In this project the UV exposure time and the rest time between the exposures were set to 4.2 and 1.8 seconds, respectively.

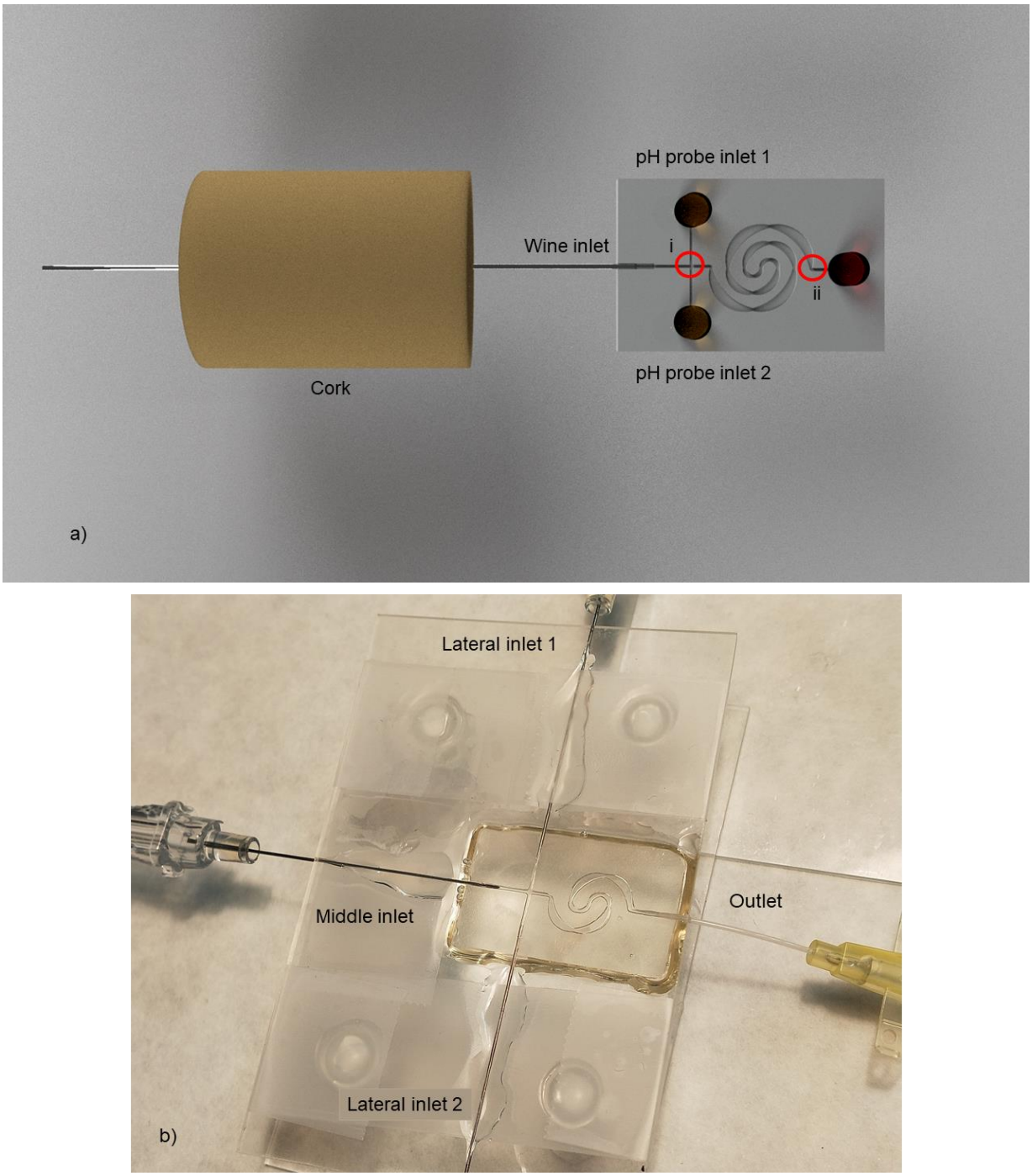

Figure 2.5 a) A schematic view of the proposed pH and ionic strength sensor. Zones i and ii indicate the ionic strength and pH evaluation zones, respectively. b) The 3D printed sensor. The geometry of the one loop with 5% expansion parts is visible inside the device.

Previous trials had shown that the utilized resin is not the best "see through" candidate. Transparency was needed to optically evaluate the performance of the mixture efficiently. Therefore, we

halted the printing process, when the channel structure was completed and remove the uncured resin from the printed platform by rinsing it into isopropanol. The device was then dried and the top of the device, except for the channel part, was covered with resin manually. Then a microscopic glass was placed on top of the printed part and acted as the ceiling of the channel. Exposure to strong UV light for 8 seconds, cured the resin and bonded the printed part to the glass. Then, the connections were installed and sealed with NOA 63, bought from Norland products. As the final step, the whole setup was exposed to gentle UV light for 1800 seconds in order to make sure that the curation has taken place completely and the device is ready to use.

Despite the claim of the 3D printer's producer, we found out that a minimum channel width of 400 µm was required to print a micromixer with BV-007 resin. Therefore, the spiral geometry of the one loop 10% micromixer, which was introduced in section "2.1.1", was 2.5 times scaled up. Meaning that the minimum channel width was increased to 500 µm. Moreover, the trials showed that exposing the freshly printed part to strong UV light causes the model to deform and bend. Therefore, a foundation of 500 µm was considered for the microfluidic platform to address the aforementioned issue, see Figure 2.5.

2.1.3. Inlet geometry analysis in µPAD applications

The cross-shaped inlet geometry had the advantage of double diffusion area in the same real-estate and allowed us to implement self-referencing sensors. Previous authors in [127], reported that the inlet's orientation influences the ratio of diffusion versus convection and therefore the performance of the micromixer. Therefore, we analyzed the effect of the angle-inlet orientation in a porous based-flow to avoid the use of external energy sources. In order to make sure that the inlets orientation does not compromise the key characteristics of the paper strips that influence the characteristics of the flow (such as channel width or distance from the inlet to the encounter zone), it was decided to add a semicircular part to the beginning of the main channel. Even though paper substrate has the advantage of capillary action to move the fluid, the manufacturing processes are limited and with lower resolution. Therefore, the proposed shape for the inlets is shown in FIgure 2.6 where a semicircular part of 10.5 mm in diameter is exactly located at the median point of the main channel width. The inlets were adjusted with respect to the semicircular's center and as a result the width of the main channel and the length of the inlets branches were always the same. The details of the geometrical features are summarized in Table 2.2.

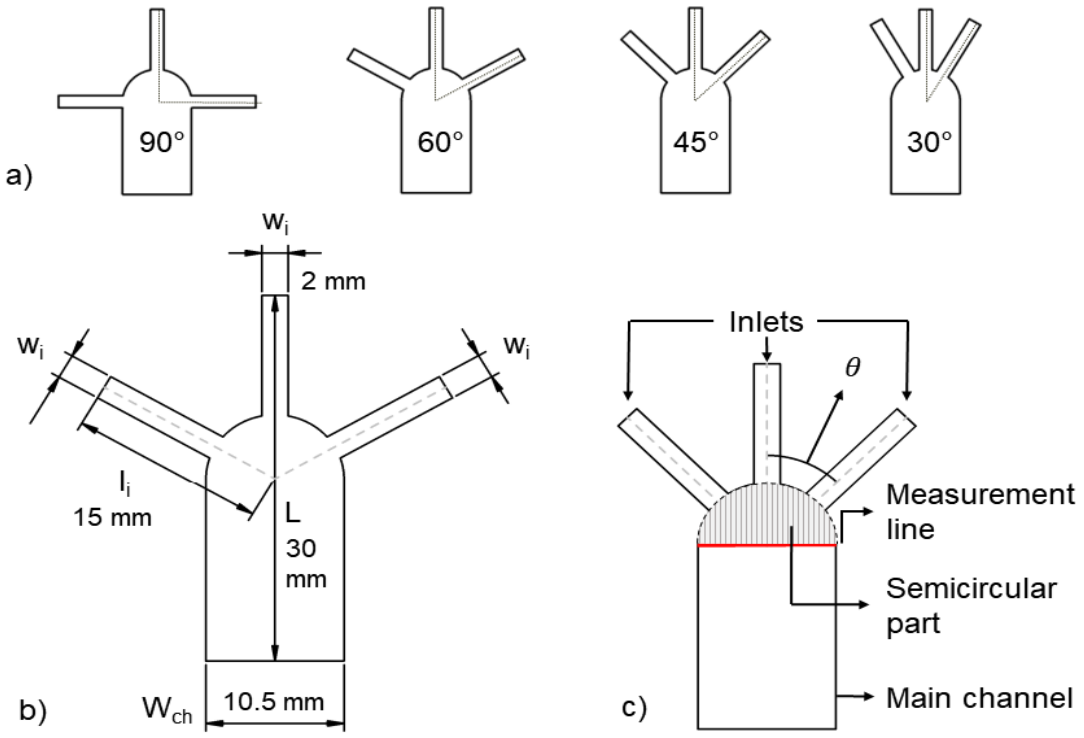

Figure 2.6 a) The studied geometries of the proposed µPAD. b) Geometrical features of the proposed µPADs. c) Displays the inlets orientation, measurement line and the added semicircular part.

Four models with inlets' angles of 90°, 60°, 45° and 30° were designed. Hereinafter, the models are referred to as the 90-degree, 60-degree, 45-degree and 30-degree models.

Table 2.2 Dimensions of the designed paper substrates as illustrated in Figure 2.3 b).

Property	Value
Length of the substrate (L)	30 mm
Substrate main channel width (W_{ch})	10.5 mm
Substrate inlet channel width (w_i)	2 mm
Substrate inlet channel length (l_i)	15 mm

2.1.3.1. Fabrication procedures of the µPAD assay

2.1.3.1.1. Preparing the paper strips

One of the limitations of the diffusion-based microfluidic sensors is the need for external energy sources. Therefore, we introduced a diffusion-based sensor, which could rely on the flow generated by capillarity. The proposed µPAD can function flawlessly with conventional and omnipresent materials. For the proof of concept, the Whatman grade 5 paper was introduced as substrate material to create a new diffusion paper-based sensor. The designs (please refer to "2.1.3." section) were reproduced in the AutoCAD software. Later by using the NEJE7000mW laser, the patterns were cut in the Whatman grade 5 papers. Paper C [128] showed that characteristics such as channel width, inlet branches length and the paper strips length, were vital and therefore equal in all the developed models.

2.1.3.1.2. Manufacturing a 3D-printed support

In order to make sure that the inlets of the paper substrate contact the reservoirs simultaneously, a 3D printed holder was introduced. The described structure was 3D printed to guarantee a synchronized fluid flow in the µPADs. The aforementioned 3D printed support consisted of 5 main parts. As illustrated in Figure 2.7 the parts were: chassis, reservoirs (which were adjusted to conform to the prepared paper strips of different inlets' angles), vertically adjustable arm, paper holder and a screw, which holds the chassis and the adjustable arm together. To ensure that the provided reagent volume to the inlets was repeatable and always the same, the vertically adjustable arm allowed a more reliable, accurate and concurrent contact between the substrate's inlets and the fluid samples. Hence, the use of this 3D printed support minimized the human error factor (synchronization errors) and guaranteed the repeatability.

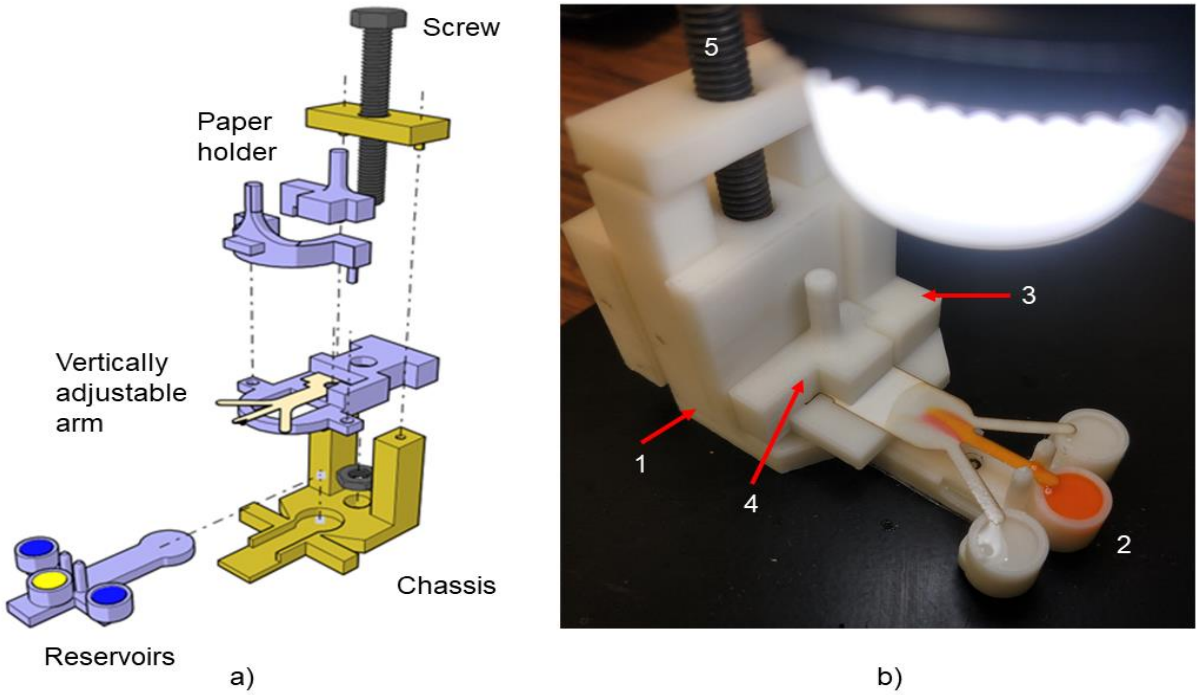

Figure 2.7 a) A schematic view of the proposed 3D printed support. b) The 3D printed support and the proposed under study µPAD.

3. Materials

This section is dedicated to the presentation of the materials and solutions that were used in the assays.

3.1. Micromixer assay

In Paper A [129], distilled water and food color E133 were used as the working reagents of the assay. The assays were conducted at room temperature. The physical properties are described in Table 3.1.

Table 3.1 Physical properties of water and Food color.

Materials	Density [kg/(m^3)]	Viscosity [kg/(m.s)]	Diffusivity in water [m^2/s]
Water	997	0.001	-
Food color E133	≈ 997	≈ 0.001	5.5e-10 [130]

3.2. pH and ionic strength measurement assay

3.2.1. Non-buffered solutions

In Paper B [124], conventional white wine (pH 3.25) was used for playing the role of the solution with unknown ionic strength. The pH of the wine was adjusted by adding limited amounts of NaOH (sodium hydroxide) solutions. For setting the pH of wine to 3.52, 3.5 ml of 0.1 M NaOH solution was added to 30 ml of wine. Achieving the pH 3.74 wine sample required the addition of 0.35 ml of 1.0 M NaOH to 40 ml of wine. All the pH measurements were conducted at room temperature.

To expand the detection range, three concentrations of 0.1, 0.5, and 1.0 M tartaric acid (2,3-Dihydroxybutanedioic acid – molecular mass of 150.087 g/mol), purchased from @Merck Schuchardt, were prepared.

Due to the pH range of the solutions (lower than pH 3.74), Methyl orange (Sodium 4-{[4-(dimethylamino)phenyl]diazenyl}benzene-1-sulfonate) was chosen as the pH identifier. Methyl orange reflects a yellow color in its neutral form, but when it captures hydronium (H_3O^+) it transforms, and its color shifts to red.

3.2.2. Buffered solutions

In Paper B [124], HEPES (4-(2-HydroxyEthyl)-1-pi-PerazineEthaneSulfonic acid), acquired from @Sigma Aldrich, was chosen to be used as a buffer due to its wide utilization in biological and biomedical researches. Three concentrations of 0.1, 0.5, and 1.0 M of HEPES solutions were prepared. Additionally, by following the protocols provided by the HEPES manufacturer, tiny amounts of 1.0 M NaOH were added to each concentration of HEPES solution in order to achieve solutions of pH 6.0, 7.0, and 8.0. Meaning that a total number of 9 solutions were prepared.

Concerning the working solutions and their pH range, it was decided to use Bromocresol purple (5',5"-diBromo-o-CresolsulfoPhthalein, also known as BCP), bought from @Sigma Aldrich. This pH indicator has a transition range of pH 5.2 up to 6.8. In acidic environments, it reflects a dark yellow color. However, by introducing hydroxide (OH^-) to it the color changes to dark blue/purple.

3.3. µPAD assay

In the µPAD development study (Paper C [128]) a similar strategy to the previous assay for detection and quantification of ionic concentration was taken. The used reagents and materials are described as follows.

3.3.1. Reagents

Conventional white wine was used as the unknown ionic concentration solutions. Three concentrations of 0.1, 0.5 and 1.0 M of tartaric acid, bought from @Merck Schuchardt OHG, were prepared. With respect to the pH range of the reagents, Methyl orange was used as the pH indicator.

3.3.2. Porous medium

The substrate to achieve capillarity was chosen to be Whatman grade 5 paper, bought from @Fisher scientific. Porous characteristics of Whatman grade 5 are indicated in the "4.4." section. Some physical characteristics of the Whatman 5 paper is displayed in Table 3.2.

Table 3.2 Physical properties of cellulose fiber and the Whatman5 paper substrate

Property	Value
Density of Cellulose ($\rho_{cellulose}$)	1.5 gr/cm^3 [131]
Density of Whatman grade 5 paper (ρ_{W5})	0.53 gr/cm^3 [131]
Pore shape factor (φ)	140 [131]
Diameter of the cellulose fiber (d)	19.6 µm [131]
Average length of the cellulose fiber (L)	830 µm
Length of the substrate (L_e)	30 mm

4. Physics and chemistry behind the assays

4.1. Physics: Fluid flow mechanics

Without any doubt, a thorough understanding of the flow behavior and its governing equations provide an accurate perspective of the question at hand. Although the mathematical description of the fluid flow is one of the most challenging subjects in mechanical engineering, Navier-Stokes equations can be used for determining the flow behavior. Navier-Stokes equations are a set of partial equations that govern the conservation of momentum, energy, and the continuity equilibrium in a control volume.

One of the universal ways to describe the momentum equation in fluids is by describing it through Newton's second law. Considering the ρ, $\vec{u}$, ∇P and μ are the density, velocity vector, pressure drop and viscosity of the flow, the following equation can be written.

$$\rho \frac{\partial \vec{u}}{\partial t} + \rho \vec{u} . \nabla \vec{u} = -\nabla P + \mu \nabla^2 \vec{u} + \vec{f} \quad \text{Eq. 4.1}$$

Where the left-hand side ($\rho \frac{\partial \vec{u}}{\partial t} + \rho \vec{u} . \nabla \vec{u}$) of the equation represents the momentum term, $-\nabla P$ indicates the pressure drop term, $\mu \nabla^2 \vec{u}$ illustrates the viscous term and $\vec{f}$ shows the body force term (any induced force: gravity and electric/magnetic field).

The previous equation can be nondimensionalized by introducing certain replacements.

The length scales can be described as:

$$x^* = \frac{x}{L} \quad \text{Eq. 4.2}$$

$$y^* = \frac{y}{L} \quad \text{Eq. 4.3}$$

$$z^* = \frac{z}{L} \quad \text{Eq. 4.4}$$

Where L is the characteristic length of our microfluidic system for instance its height.

The equations 4.2, 4.3 and 4.4 can be applied to the divergence operator (∇). Therefore, it can be expressed as:

$$\nabla^* = L\,\nabla \quad \text{Eq. 4.5}$$

$$\nabla^{*2} = L^2\,\nabla^2 \quad \text{Eq. 4.6}$$

Nondimensionalization should be carried out for the velocity (Eq. 4.7), time (Eq. 4.8) and pressure scales and in microfluidic systems. We can assume that pressure drop is dominated by viscous forces, therefore pressure nondimensionalization is done according to (Eq. 4.9):

$$\vec{u}^* = \frac{\vec{u}}{U} \quad \text{Eq. 4.7}$$

$$t^* = \frac{t}{t_{ref}} \quad \text{Eq. 4.8}$$

Whereas U is the characteristic velocity and that can be obtained from the boundary conditions, such as the inlet velocity. t_{ref} is the fastest time scale in the problem and can be obtained from the boundary conditions, such as $\frac{L}{U}$, and for the nondimensionalized pressure:

$$\Delta P \sim \mu \Delta^2 \vec{u}$$

$$\frac{dP}{dx} \sim \mu \frac{d^2u}{dy^2}$$

$$\frac{P^*}{L} = \mu \frac{U}{L^2}$$

$$P^* = \frac{P}{\mu \frac{U}{L}} \quad \text{Eq. 4.9}$$

By replacing the nondimensionalized forms of the variables in the original equation (Eq. 4.1) we can obtain the following equation.

$$\frac{\rho U}{t_{ref}} \frac{\partial \vec{u}^*}{\partial t^*} + \frac{\rho U}{L} \vec{u}^* . \nabla^* \vec{u}^* = -\frac{\mu U}{L^2} \nabla^* P^* + \frac{\mu U}{L^2}\, \nabla^{*2} \vec{u}^* \quad \text{Eq. 4.10}$$

Which can also be written as:

$$\rho \frac{UL}{\mu} \frac{L}{U t_{ref}} \frac{\partial \vec{u}^*}{\partial t^*} + \rho\, \frac{UL}{\mu} \vec{u}^* . \nabla^* \vec{u}^* = -\nabla^* P^* + \nabla^{*2} \vec{u}^* \quad \text{Eq. 4.11}$$

Once dimensionalized, the derivative nondimensionalized terms should be of the order 1. Meaning that the magnitude of these terms is affected by the pre-multiplying factor rather than the derivatives themselves.

By defining the Reynolds number and the Strouhal number as Equations 4.12 and 4.13:

$$Re = \rho \frac{UL}{\mu} \quad \text{Eq. 4.12}$$

$$St = \frac{Ut_{ref}}{L} \quad \text{Eq. 4.13}$$

The Equation 4.11 can be written as:

$$\frac{Re}{St} \frac{\partial \vec{u}^*}{\partial t^*} + Re \,.\vec{u}^*.\nabla^*\vec{u}^* = -\nabla^* P^* + \nabla^{*2}\vec{u}^* \quad \text{Eq. 4.14}$$

In the microfluidics the Reynolds number and changes in the velocity are quite small, therefore the left-hand side of the equation can be neglected and the equation can be rewritten as:

$$\nabla^* P^* = \nabla^{*2}\vec{u}^* \quad \text{Eq. 4.15}$$

And by reversing the nondimensionalization process, we can obtain:

$$\nabla P = \mu \nabla^2 \vec{u} \quad \text{Eq. 4.16}$$

Which is the Stokes equation in low Reynolds numbers and describes the conservation of momentum.

Another important aspect of the Navier-Stokes equations is the continuity, which implies that the total input and output flux of control volume should be equal. This statement can be mathematically expressed as:

$$\frac{\partial \rho}{\partial t} + \frac{\partial (\rho u)}{\partial x} + \frac{\partial (\rho v)}{\partial y} + \frac{\partial (\rho w)}{\partial z} = 0 \quad \text{Eq. 4.17}$$

Let u, v and w be the magnitude of velocity in the x, y and z directions.

By considering the incompressible and steady state flow, the continuity equation can be summarized to:

$$\nabla . \vec{u} = 0 \quad \text{Eq. 4.18}$$

There is another equation that describes the conservation of energy in fluid flows. However, due to the absence of heat exchange and low fluctuations in the velocity (especially in the applications foreseen in this thesis), the energy equation can be neglected.

The equations 4.16 and 4.18 in complex geometries can be solved by adopting the finite element (FEM) or finite volume (FVM) methods. In these methods, the solving domain is discretized into smaller domains and the aforementioned equations are solved in each cell, with respect to boundary conditions

and the neighboring cells. If the difference of the results in successive iterations does not exceed a certain value (residuals) the last result is considered as the flow condition in that certain cell.

4.2. Physical: Transport of species

As it was mentioned in the previous section, flows in the microfluidic systems are usually laminar. Therefore, the transport phenomenon mainly relies on diffusion. The diffusion phenomenon follows the Fick's first law which is described as:

$$\vec{J} = -D\nabla C \qquad \text{Eq. 4.19}$$

Let J be the mass flux of species, D be the diffusion coefficient and C be the concentration of species. It is worthy to note that the flux of species is from the richer regions towards the regions with less concentration. So, if a rich and a poor fluid layer are flowing in parallel, the flux of species would be perpendicular to the general direction of flow. By assuming that the material of interest is conserved, then Eq. 4.19 can be derived into:

$$\frac{\partial C}{\partial t} = \nabla.\vec{J} \qquad \text{Eq. 4.20}$$

By combining Eq. 4.20 and the momentum equation (Eq. 4.16), the seconds Fick's law can be described as:

$$\frac{\partial C}{\partial t} = D\left(\frac{\partial^2 C}{\partial x^2} + \frac{\partial^2 C}{\partial y^2} + \frac{\partial^2 C}{\partial z^2}\right) \qquad \text{Eq. 4.21}$$

Which implies that the rate of concentration depletion/accumulation is proportional to the gradient of concentration distribution.

In addition to molecular diffusion, there is another important transport mechanism in the microfluidics and laminar flow in general, which is called advection. This mechanism is responsible for transporting the species as a bulk and is usually in the direction of the flow. Since the bulk movement depends on the flow velocity, it is expressed as:

$$\vec{J} = \vec{u}\,.C \qquad \text{Eq. 4.22}$$

Where $\vec{u}$ is the velocity along the direction of flow and C is the concentration of species.

Combining equations 4.21 and 4.22 the mass transport equation can be described as:

$$\frac{\partial C}{\partial t} + u\frac{\partial C}{\partial x} + v\frac{\partial C}{\partial y} + w\frac{\partial C}{\partial z} = D\nabla^2 C \qquad \text{Eq. 4.23}$$

In the above equation, u, v and w represent the velocity vector in the x, y and z directions, respectively.

Therefore, the general advection diffusion equation for a 3D problem can be expressed as:

$$\frac{\partial C}{\partial t} + \nabla \cdot (\vec{u} \cdot C) = \nabla \cdot (D \nabla C) \qquad \text{Eq. 4.24}$$

Whereas, $\frac{\partial C}{\partial t}$ is the transient term, $\nabla \cdot (\vec{u} \cdot C)$ is the convective flux, $\nabla \cdot (D \nabla C)$ is the diffusive flux.

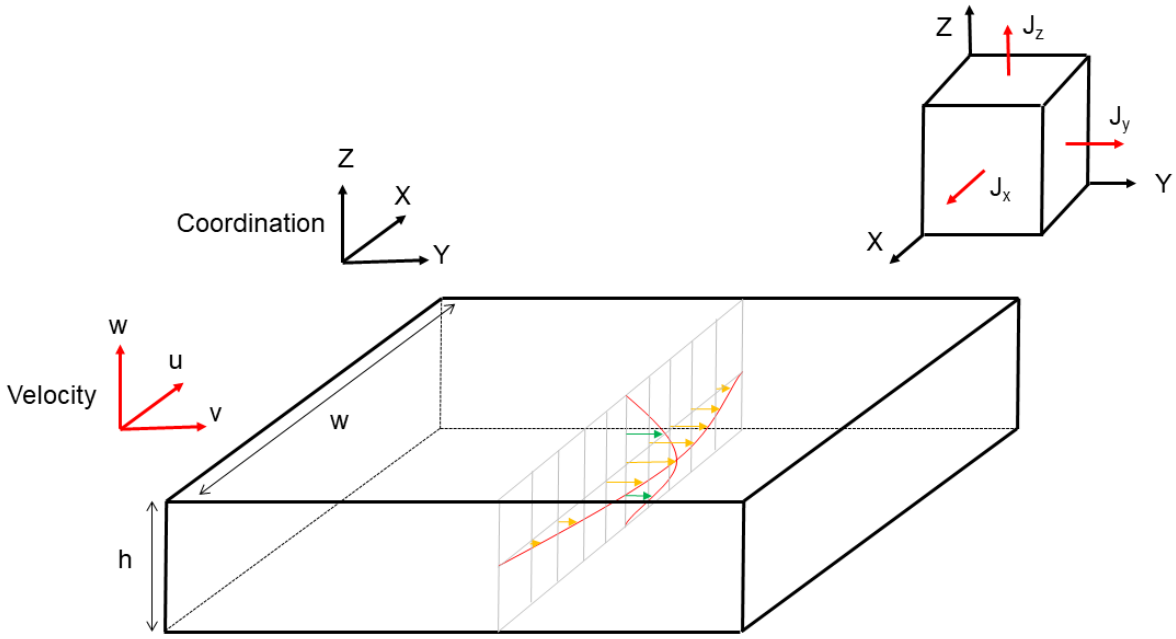

Figure 4.1 A schematic view of the flow and flux in a rectangular channel.

By expanding the Eq. 4.22, the following equation can be written:

$$\frac{\partial C}{\partial t} + \frac{\partial}{\partial x}(u \cdot C) + \frac{\partial}{\partial y}(v \cdot C) + \frac{\partial}{\partial z}(w \cdot C) = D\left[\frac{\partial^2 C}{\partial x^2} + \frac{\partial^2 C}{\partial y^2} + \frac{\partial^2 C}{\partial z^2}\right] \qquad \text{Eq. 4.25}$$

If the channel height (h) is much smaller than the channel width (w) ($-h^2/D << w^2/D$), then time scale in the Z is smaller than diffusion in W and viscous effects are only dominant on the wall, the velocity is almost uniform in the middle of the channel $\vec{U} \approx \vec{u}_x$ and the velocity at the wall is 0. Therefore, assuming this, and looking for a steady-state situation, the equation can be simplified to:

$$u\frac{\partial C}{\partial x} = D\frac{\partial^2 C}{\partial y^2} \qquad \text{Eq. 4.26}$$

Being u the characteristic velocity in the X direction.

A dimensionless number (Peclet number) is defined to illustrate the ratio of advective transport to diffusive transport rates. Peclet number is expressed as:

$$Pe = \frac{Lu}{D} = \frac{Advective\ transport\ rate}{Diffusive\ transport\ rate} \quad \text{Eq. 4.27}$$

Let L, u and D be the characteristic length, velocity, and diffusion coefficient, respectively.

4.3. Porous medium characteristics

Porous mediums are matrices of particles and fibers that are packed together. Between the particles and fibers there are some voids (or pores) which liquid can flow through them. Although the size and shape of these pores play a significant role in determining the flow behavior within the porous medium, the governing equations are similar to the Navier-stokes equations. As it was expressed earlier, by assuming the Newtonian, incompressible and steady state flow, the continuity, and momentum conservation equations can be expressed as:

$$\nabla . \vec{u} = 0, \quad \text{Eq. 4.28}$$

$$\rho\ (\vec{u} . \nabla \vec{u}) = -\nabla P + \mu \nabla^2 \vec{u} \quad \text{Eq. 4.29}$$

Where $\vec{u}$, ρ, ∇P and μ are the velocity vector, density, pressure gradient and viscosity of fluid, respectively.

When the density (ρ) and viscosity (μ) of the working fluid is known, the superficial velocity ($\vec{U}$) for a given pressure gradient (∇P) can be obtained through:

$$\vec{U} = \frac{1}{V_T} \int_{V_f} \vec{u}\ dv = \varepsilon\ .\ \bar{u} \quad \text{Eq. 4.30}$$

$$\varepsilon = \frac{V_f}{V_T}\ , \quad \text{Eq. 4.31}$$

Where V_f, V_T and ε represent the void volume, body volume and porosity of the porous medium and $\bar{u}$ is the average velocity of the flow within the porous medium.

On the other hand, the Darcy equation implies that the superficial velocity is proportional to the pressure gradient.

$$\vec{U} = -\frac{\alpha}{\mu} \nabla P \quad \text{Eq. 4.32}$$

Let α be the permeability of the porous medium.

At the same time, the velocity can be expressed in term of hydraulic diameter (D_h) via the Poiseuille law as:

$$\vec{u} = -\frac{{D_h}^2}{32\mu}.\nabla P \quad \text{Eq. 4.33}$$

Whereas, the Carmen-Kozeny model describes the hydraulic diameter as:

$$D_h = \frac{4\,\varepsilon\,V}{S_v} \quad \text{Eq. 4.34}$$

Where, the S_v represents the total wetted surface and V is the channel's volume. Since the cellulose fibers in the Whatman 5 paper can be presumed as cylinders, the S_v can be calculated through:

$$S_v = \frac{(1-\varepsilon)V}{d} \quad \text{Eq. 4.35}$$

Let d be the diameter of the cylinder (fiber). Therefore, the hydraulic diameter can be described as:

$$D_h = \frac{\varepsilon\, d}{(1-\varepsilon)} \quad \text{Eq. 4.36}$$

Now by combining equations 4.28 and 4.30 the following equation can be obtained [132]:

$$\frac{\alpha}{d^2} = \frac{\varepsilon^3}{\Psi_{ck}\,(1-\varepsilon)^2} \quad \text{Eq. 4.37}$$

Whereas, Ψ_{ck} represents the Carmen-Kozeny factor and it can be expressed in terms of its components; namely the pore shape factor (φ) and tortuosity ($\frac{L_e}{L}$).

$$\Psi_{ck} = \varphi\,(\frac{L_e}{L})^2 \quad \text{Eq. 4.38}$$

Let L_e and L be average effective streamline length and system length, respectively. Therefore, by knowing the physical properties of the porous media, the porosity and permeability of the substrate can be determined.

4.4. Chemical: pH and ionic strength in buffer and non-buffer solutions

In order to evaluate the mixing performance of the developed mixer: the samples will be mixed with different pH indicators and its pH and Ionic Strength will be evaluated. pH measurement is considered as one of the key elements in evaluation of biological and chemical reactions. The acidity or alkalinity can be defined through the presence of hydronium [H_3O^+] or hydroxide [OH^-] ions in the solutions. If a substance readily donates protons in the aqueous media, it is considered an acid and when a substance willingly accepts protons, it is considered a base (Please see reaction 1). Most of the acids and bases are considered weak acids and bases. Meaning that not all the hydronium or hydroxide ions are dissociated

from their parent molecule. Acids and bases have different abilities in releasing the mentioned ions and this ability is quantified in acid ionization constant (Ka), see Eq. 4.39. According to Eq. 4.39, the greater the Ka the more dissociated protons in the solution.

$$HA + H_2O \rightleftarrows A^- + H_3O^+ \quad (1)$$

$$pK_a = -\log \log [K_a] \quad \text{Eq. 4.39}$$

Being HA an arbitrary acid and A^- and H_3O^+ denote the conjugate base and the released proton after the reaction.

In most of the biological applications, maintaining pH in a specific and usually narrow range is of high interest. The buffer solution should be capable of resisting pH alterations, even when strong acids or bases are added to the solution. Buffers can be used to address this requirement. They consist of a weak acid and its conjugate base. When small amounts of acids are added to the buffer, the conjugate base present in the solution captures the hydronium and does not allow the pH to increase. Similarly, when base is added to the buffer, acid donates a proton to the hydroxide group and converts it to water and the acid itself turns to conjugate base [133] (See reactions (1), (2) and (3)).

This reaction is described by Henderson-Hasselbalch Eq. 4.40, used to measure the pH of the buffers after adding acids or bases in the solution.

$$A^- + H_3O^+ \rightarrow HA + H_2O \quad (2)$$

$$HA + OH^- \rightarrow A^- + H_2O \quad (3)$$

$$pH = pK_a + \log \frac{[A^-]}{[HA]} \quad \text{Eq. 4.40}$$

Where HA and A^- are an arbitrary acid and its base conjugate, respectively. [HA] and [A^-] are denoting their concentrations in the solution.

According to reactions (1,2 and 3), there is a balance between the concentration of the acid [HA] and the concentration of the conjugate base [A^-] and the ratio of this concentration modifies the pH. Buffer capacity, or in another word the ability of accepting different concentrations of acid or alkaline, directly depends on the molarity (concentration) of the buffer. The greater the molarity, the higher the capacity to capture the released ions in the solutions.

An effective buffer has a symmetrical range of pH, which is about ±1 units of the pKa of the founding weak acid. Due to the logarithm of acid and free conjugate base concentration (See Eq. 4.40), buffers act as shock absorbers and do not let the pH to escalate or drop dramatically. However, depending

on the initial concentration of the HA and the balance between the acid and the conjugate base, almost any pH can be achieved in a solution.

One of the most accurate methods to determine the capacity of the buffers, through which they can stabilize pH alterations, is by measuring their ionic strength. This measurement reveals the amount of conjugate acid/base ions in the solution. As a result, a solution with higher concentration of conjugate acid/base would show higher tolerance against pH changes.

4.4.1. Limit of detection

Limit of detection (LOD) expresses the minimum amount of a compound that can be detected in comparison to its absence. One of the most conventional methods for determining the LOD in experimental methods is by considering the generated standard deviation. In most of the assays the distribution of results can be illustrated by a regression line, expressed as:

$$y = mx + b \qquad \text{Eq. 4.40}$$

Where m is the slope of the regression line and b is the intersection point of the line with the y-axis.

By determining the regression line formula and obtaining the standard deviation (S) of the assays, the limit of detection can be found through:

$$LOD = 3.3 \times \frac{S}{m} \qquad \text{Eq. 4.41}$$

5. Numerical Models

Equations described in Section 4 can be solved by applying the numerical calculation methods, which is called Computational Fluid Dynamics (as known as CFD). The basis of CFD is founded on dividing the problem domain into smaller sections or cells. The discretized equations are selected and assigned to the equation. Later, with respect to the given information (also known as initial conditions and boundary conditions) and the neighboring cells the equations are solved in every cell, respectively. This process shall continue for the whole problem domain, until to the point that the difference between the answers of two consecutive iterations in every cell is smaller than an acceptable value (also known as Residual). The discretized equations are dependent on the problem and certain simplifications (symmetrical domain) can be assumed to minimize the calculation cost of the problem. CFD has been proven to be a powerful tool in predicting and interpreting the fluid motion and can be considered a legitimate and necessary step in developing the devices that work with fluids. In this work, the finite volume CFD software ANSYS FLUENT was used to carry out the numerical simulation.

5.1. Governing equations in Fluid Dynamics

From the governing equations, the continuity and momentum equations are described in previous chapter (4. Physics and chemistry behind the assays- Eq. 4.16 and Eq. 4.29). Aside from the mentioned equations, there is another equation that registers the energy conservation in the control volume. The energy equation is described as:

$$\frac{\partial(\rho H)}{\partial t} + \frac{\partial \rho}{\partial t} \nabla . (\rho \vec{u} H) = \nabla . (k \nabla T) + \vec{u} . \nabla p \qquad \text{Eq. 5.1}$$

Where H is the convective heat transfer coefficient, k is the conductive heat transfer coefficient and T is the absolute temperature. It should be noted that, since the assays are performed at the same temperature and the velocity fluctuations are minimal and the natural convection is negligible, the energy equation (Eq. 5.1) is neglected during the numerical simulations.

5.2. The Diffusion phenomenon

One of the important features of the ANSYS Fluent software is the capability of coupling various aspects of the fluid (in this work mixing in the form of diffusion) to the Navier-Stokes equations. In other words, it is possible for the software to solve the continuity and the momentum equations at the same

time as the advection-diffusion equation. Therefore, the results of concentration distribution are coupled with the velocity profile.

In order to achieve this goal, an arbitrary user-defined scalar should be defined. Based on the input information of scalar, The ANSYS software solves the following equation to determine the source term (S_{φ_k}):

$$\frac{\partial \rho \varphi_k}{\partial t} + \frac{\partial}{\partial x_i}\left(\rho u_i \varphi_k - \Gamma_k \frac{\partial \varphi_k}{\partial x_i}\right) = S_{\varphi_k} \qquad \text{Eq. 5.2}$$

Where k depends on the number of introduced scalars. Γ_k is the defined diffusion coefficient for the *i*th scalar. ρ and u_i are the fluid density and flow velocity vector.

In the above-mentioned equation, first part of the left-hand side equation ($\frac{\partial \rho \varphi_k}{\partial t}$) illustrates the unsteady term. While the second ($\frac{\partial F_i \varphi_k}{\partial x_i}$) and third parts ($\nabla . \Gamma_k \varphi_k$) represent the convective and diffusive terms, respectively.

By assuming a steady-state problem, the Eq. 5.2 can be summarized as:

$$-\frac{\partial}{\partial x_i}\left(\Gamma_k \frac{\partial \varphi_k}{\partial x_i}\right) = S_{\varphi_k} \qquad \text{Eq. 5.3}$$

5.2.1. Measuring the mixing efficiency

The mixer efficiency is experimentally measured by a normalized ratio (σ). This normalized ratio is the difference of the concentration of species at a given point and the ideal concentration to the difference of the maximum concentration and the ideal concentration. The ratio is expressed as:

$$\sigma = \frac{C_i - \bar{C}}{C_{max} - \bar{C}} \qquad \text{Eq. 5.4}$$

Where, C_i represents the concentration of species at a given pixel (position across the outlet of the channel), $\overline{C}$ denotes the ideal concentration (which can be translated into the median value between the minimum and maximum concentration within the channel) and notably, C_{max} illustrates the maximum concentration of species inside the micromixer.

When the normalized ratio (σ) is calculated for all the pixels (or nodes in the numerical simulation language) over the outlet, the mixing efficiency (M.Q) can be calculated through:

$$M.Q = 1 - \sqrt{\frac{1}{N} \times \sum_{1}^{N} \sigma^2} \quad \text{Eq. 5.5}$$

In the above equation, N represents the number of pixels (or nodes) over the outlet and M.Q is the mixing quality of the investigated device.

5.3 Numerical simulation of porous media

Porous media can be modeled by adding a momentum source term (S_i) to the standard fluid flow equations. The source term consists of two losses in the porous media. Namely; the viscous loss term and inertial loss term.

$$S_i = -\left(\sum_{j=1}^{3} D_{ij}\, \mu\, v_j + \sum_{j=1}^{3} C_{ij}\, \frac{1}{2}\, \rho\, |v|\, v_j\right) \quad \text{Eq. 5.6}$$

Whereas, μ, ρ and $|v|$represent the viscosity, density, and velocity magnitude (in the x, y, and z directions), respectively. Meanwhile, S_i, D and C are the momentum loss and prescribed matrices in the *i*th direction (x, y, z). In the above equation the D_{ij} matrix is responsible for the viscous losses and C_{ij} is responsible for the inertial losses. By assuming a simple homogeneous porous media, the momentum loss term can be expressed as:

$$S_i = -\left(\frac{\mu}{\alpha}\, v_i + C_2\, \frac{1}{2}\, \rho\, |v|\, v_i\right) \quad \text{Eq. 5.7}$$

Let α and C_2 be the permeability and inertial resistance factor.

In the laminar flows within porous media, the viscous loss term dominates the inertial loss term. Therefore, the Darcy law would be sufficient to describe the porous media as:

$$\nabla p = -\frac{\mu}{\alpha}\, \bar{v} \quad \text{Eq. 5.8}$$

Subsequently, the pressure drop in different directions would be expressed as:

$$\Delta p_x = \sum_{j=1}^{3} \frac{\mu}{\alpha_{xj}}\, v_j\, \Delta n_x \quad \text{Eq. 5.9}$$

$$\Delta p_y = \sum_{j=1}^{3} \frac{\mu}{\alpha_{yj}}\, v_j\, \Delta n_y \quad \text{Eq. 5.10}$$

$$\Delta p_z = \sum_{j=1}^{3} \frac{\mu}{\alpha_{zj}} \, v_j \, \Delta n_z \qquad \text{Eq. 5.11}$$

Whereas, $\frac{1}{\alpha_{ij}}$ is the defined permeability in a specific direction, v_j is the velocity components in the x, y, and z directions and Δn_x, Δn_y and Δn_z are the thickness of the porous media in the x, y and z directions, respectively.

It is worthy to note that the permeability can be calculated via different empirical and theoretical methods. In this thesis, we used a theoretical approach (described in section "4.3") to estimate the permeability of the porous substrate.

5.4. Numerical error sources

Simulations mimic real world problems in a mathematical manner and predict the outcome with respect to the initial information. There is no need to mention that this method is prone to several errors, which can drastically affect the results of the simulation. If it is decided to conduct numerical simulation, one should make sure that the mathematical model is as close as possible to the real-world case and the influence of error generating factors are diminished as possible. After taking such care, the researcher can claim that the simulation's results have an acceptable precision. Regarding the abovementioned points, the errors can be divided into 3 categories.

5.4.1. Errors of modeling

These errors are rooted in carelessly setting up the initial and boundary conditions or poorly simplifying the problem. It is obvious that the answer of the numerical simulation would be questionable, if the initial and boundary conditions are set inaccurately.

5.4.2. Errors of discretization

These errors arise when the results of the governing equations are still grid-dependent. Meaning that the size of each cell and the mesh density can affect the results of the whole simulation. This error might seem small and negligible for every individual cell, but the accumulative error can significantly avert the answer from the correct value. Therefore, careful efforts should be taken to make sure that the simulation is mesh-independent and the produced results are reliable regardless of mesh type or size. Several methods have been introduced on how to determine a suitable mesh density. Richardson's extrapolation is one of the most common methods in determining the proper grid and mesh density. According to this method, if the error reduction in at least three consecutive grid sizes is known and the

errors of the two finest grids are in an acceptable range, then the simulation can be considered grid-independent. It should be noticed that this method can be quite expensive from the calculation point of view. Hence, a wise decision should be made in order to make a compromise between the accuracy and the required calculation time and capacity.

5.4.3. Errors of iteration

These errors are rooted in the difference of the iterative results of cells and the results in the real-world problems. In Computational Fluid Dynamics (CFD) the governing equations are solved in every cell from inlet/inlets to outlet/outlets with respect to the initial conditions and neighboring cells. In the following iterations, the governing equations results should be corrected with the help of a correction formulae. But if the difference in the results of two consecutive iterations is smaller than a defined value, the simulation concludes that the governing equations have been converged and moves to the next cell. Like the discretization error, this error can be negligible for the cells close to the inlet and the boundaries, but by resuming the calculations the accumulative error can be serious. One of the most conventional ways to address this issue is by defining a proper value for residual. If a suitable value is set for it, it can reflect an appropriate influence on consecutive iterations and results in producing answers with minimum errors.

6. Detection and quantification methods and experimental setups

This section presents an overview on the methods that are used for detecting certain compounds or evaluating the performance of developed devices. Moreover, the experimental setup of the assay is presented as well.

6.1. Micromixer assay

6.1.1. Evaluation of the numerical simulation results

In Paper A [129], nine micromixers of one loop, two loops and three loops with expansion and contraction parts of 0%, 5% and 10% were modelled. Each model was studied under the Re 0.1, 1.0 and 10 regimes. The distribution of species over the outlet was gathered and analyzed. The mixing quality of the described models was investigated by the method that is explained in section "5.2.1. Measuring the mixing efficiency."

6.1.2. Experimental setup of the micromixer assay

The micromixers have three inlets. The food color (E133) was injected through the lateral channel, and water was injected via the middle inlet. The total discharge of the lateral channels was equal to the flowrate of the middle inlet. The cumulative flow from the inlets were set to 0.4 ml/h to satisfy the Re 1.0 regime requirement. The lateral inlets were connected to the Graseby 3200 syringe pump and the middle inlet was connected to kdScientific 410-CE syringe pump.

Pictures were taken at the outlet of the micromixer by a Leica microscope (LEICA EZ4D) at 30X magnification. The microscope has the capability of beaming light from the bottom, the sides, and the top on the object of interest. In order to eliminate the effect of ambient and background lights, a microscopic slide with a circle (500 µm of diameter) engraved on it was fixed in the microscope. Careful efforts were made to make sure that the outlet of the micromixers was located in the center of the circle. Then, the grey profile of the mixture at the outlet was extracted by ImageJ software. The grey values were processed with the method described in section "5.2.1." to determine the performance of the device under study. Figure 6.1 presents a brief representation of the micromixer assay.

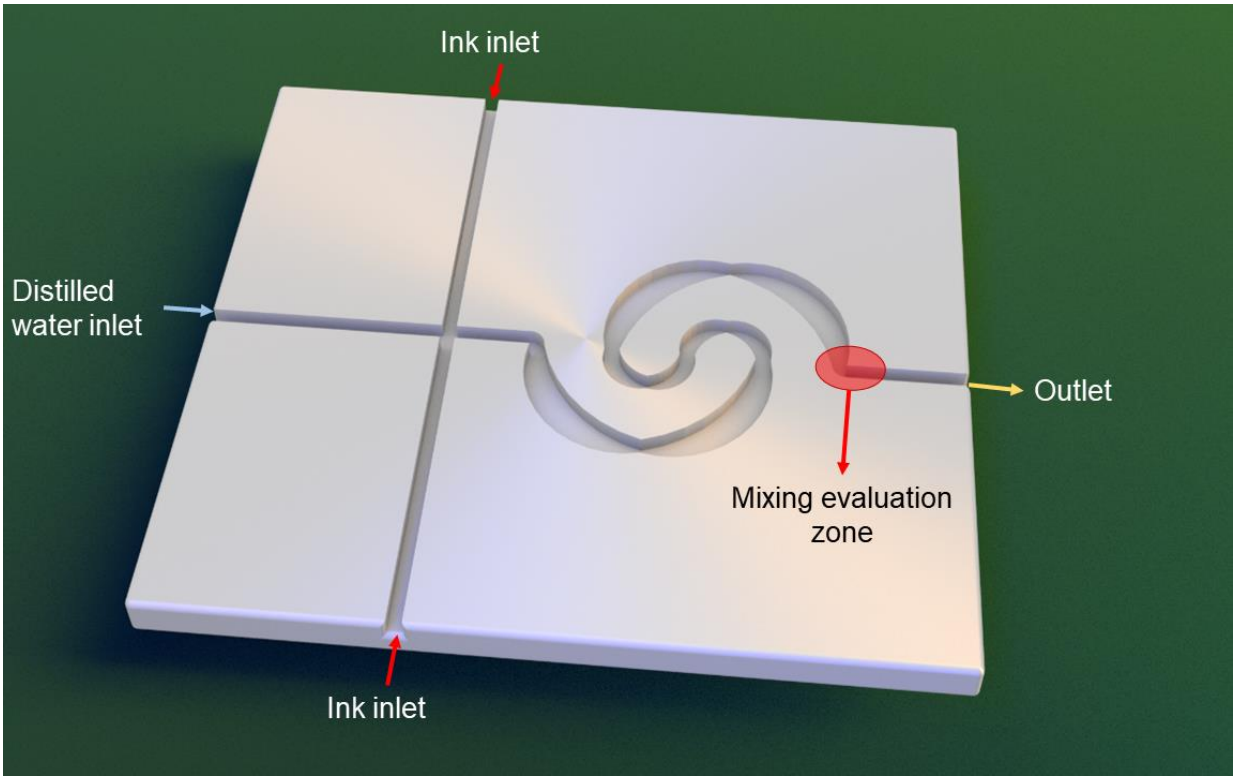

Figure 6.1 Schematic view of the micromixer assay (one loop with 10% expansion and contraction parts. The solutions are entered through the inlets via syringe pumps and pictures are taken at the mixing evaluation zone.

6.2. pH and ionic strength sensor

6.2.1. Buffered solutions assay

In Paper B [124], in order to inject the solutions two syringe pumps of Graseby 3200 and kdScientific were used. The flowrate of the pH indicator (methyl orange) was set to 0.7 ml/h. On the other hand, the flowrate of the wine and/tartaric acid solutions were set to 1.4, 1.7 and 2.1 ml/h, based upon the requirement of the test. Diffusion width investigation was carried out at the intersection of the inlet. Pictures were captured by a Dino-Lite MS325B microscope and were later analyzed by ImageJ software. Color spectrum of the solutions restricted the colorimetric measurements to green profile analysis. The diffusion width was measured based on the drop in the green color indices. pH measurement was carried out after the inlets' intersection to make sure that the diffusion width does not affect the color transform of the pH indicator. Other than measuring the nadir in the green color profiles, Origin software was used to analyze the respective graphs of each solution and to calculate the surface area under the graph in the reaction zones. Please see Figure 6.2.

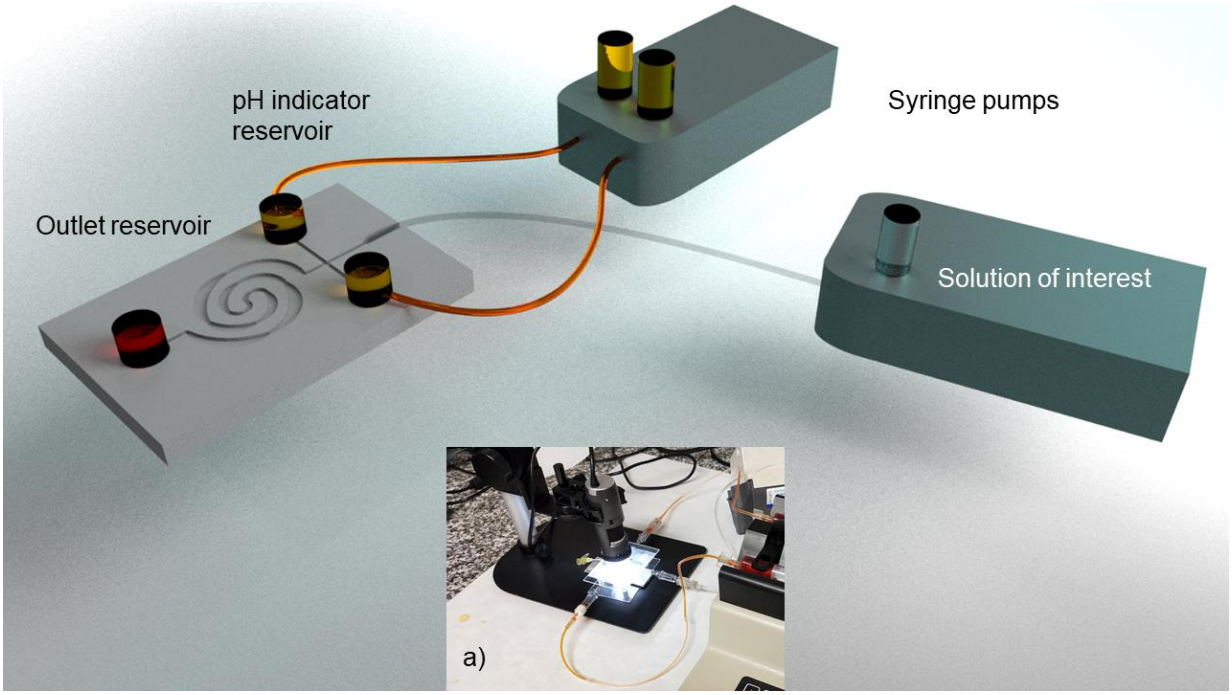

Figure 6.2 Schematic view of the 3D printed pH and ionic strength sensor. a) The developed sensor under study.

6.2.2. Non-buffered solutions assay

This experiment (in Paper B [124]) benefitted from the same arrangements and instruments as the buffered solutions assay (please refer to Figure 6.2). pH indicator was injected through the middle inlet and the buffer solutions (different concentrations of HEPES) were injected through the lateral inlets. The accumulative discharge of lateral inlets is equal to the flowrate of the middle inlet. The total flow rate was set to apply Re 1.0 regime to the flow. Ionic concentration of buffers is/was investigated by measuring the corresponding diffusion widths in the inlets' intersection. The diffusion width was measured by analyzing the blue color profile and studying the drop in it. On the other hand, the pH measurement was carried out at the outlet. The decision was due to the nature of buffers and their resistance against pH alterations. In order to make sure that the buffer solutions and pH indicator are acceptably mixed, the pictures were taken at the outlet of the micromixer. Blue color profiles were then extracted and the mean drops in the blue color profiles in different solutions were compared.

6.3. µPAD assay

6.3.1. Analyzing the numerical simulation results

In the numerical simulation section of Paper C [128], the distribution of scalars at the outlet was measured for studying the effect of inlets' angle on the diffusion. The analysis was carried out by relying on the described method in section "5.2.1."

6.3.2. Experimental setup of the µPAD assay

Due to the uneven capillary motion of fluids in different models, it was decided to establish a reference point for comparing different models (in Paper C [128]), as it is demonstrated in Figure 6.3. It was determined to monitor the green profile of the reaction zone and look for any signs of drop in the green color indices. It is worth remembering that the methyl orange is yellow in its neutral form, but methyl orange transforms and its color changes to red as it captures hydronium (H_3O^+). The color shift can be traced via green color index analysis, since the yellow color has a higher green color index. By following the described procedure for all the models, the "Time zero" benchmark was established. Several trials were conducted to verify its legitimacy and integrity. After defining the benchmark time, several pictures were captured by Dino-lite MS325S microscope of the paper strip at 60, 90, 120, 180 and 240 seconds after the "Time zero". Then, the green profile of the diffusion zone was extracted by the ImageJ software. The diffusion widths were calculated by investigating the drop in the green color indices compared to neutral zones.

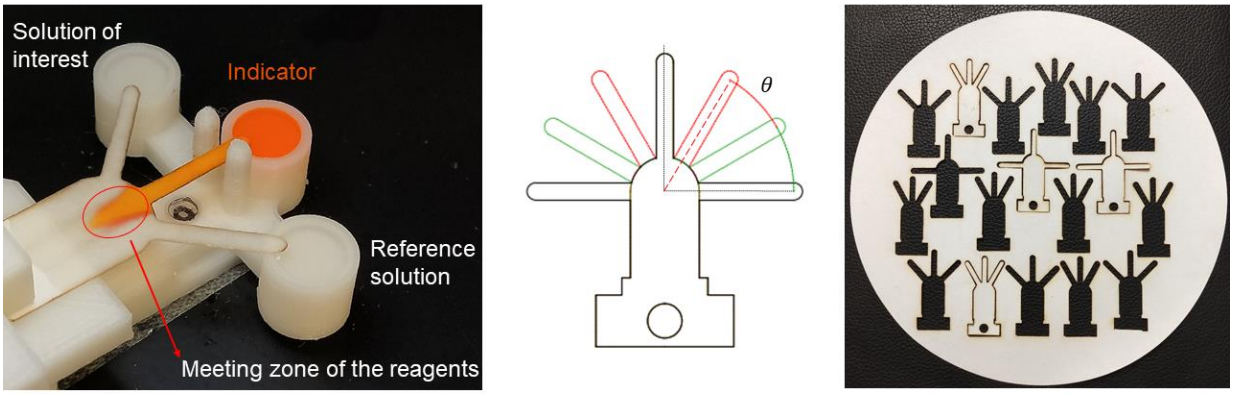

Figure 6.3 An illustration of the understudy µPAD assay, proposed geometries and the laser cut paper-based microfluidic strips in the Whatman 5 paper.

6.4. Data curation and error sources

The errors might have occurred during numerical simulations or experimental sections. The errors regarding numerical study are described in section “5.3 Numerical error sources''. In the experimental part, the errors might have been rooted in mistakes done by staff or devices. In order to minimize these errors, every assay was repeated several times to check the repeatability and eliminate any chance of malfunction. Furthermore, careful efforts were made to make sure that all the assays were carried out in similar temperature, ambient light and magnification rate. Finally, the outliers of all the results were detected at a 0.05 significance level by applying the Grubb’s test to minimize the influence of the abovementioned errors.

7. Conclusion

This thesis aimed to design a micromixer with significant performance in physiological ranges and capable of being integrated in a conceptualized POCT device without an increase of pressure loss that stops the flow and disables the analysis. The novel design should be adaptable to different microfabrication methods, while maintaining its functionality and performance.

The results presented in “paper A” [129] propose a variable radius spiral micromixer that performs in the flow regime range of Reynolds number 0.1 to 10.0. The proposed spiral architecture with modified expansion and contraction parts optimizes the surface area occupation and minimizes the pressure drop. The numerical models have been used to analyze its performance and the models have been validated experimentally at Re 0.1. Experimental results showed an acceptable convergence to numerical analysis.

According to the results, the number of mixer loops increases the homogeneity of the mixture at the outlet. A uniform spiral micromixer (micromixer with 0% expansion and contraction part) at Re 1.0 showed poor mixing performance, even when the number of loops was increased. Although it should be noted that the decrease in the performance at the Re 1.0 regime flow was inevitable.

Therefore, the proposed modified variable radius spiral micromixer, regardless of the number of loops, and at every given inlet flow, provides an improved performance. Combining a two loop or three loop micromixer with expansion and contraction parts achieves mixing efficiencies higher than 90% at low Re Regimes. The proposed micromixer demonstrated mixing efficiencies between 77.6% and 98.5%.

In addition, the proposed expansion and contraction parts decrease the pressure drop by more than 60% compared to spiral micromixer without expansion and contraction parts. Finally, the design is fully compatible with current manufacturing methods, employing a two loop or three loop micromixer with expansion parts is a reliable choice in situations where it is required to ease the fabrication, provide a homogenous outcome, use the surface area efficiently and have a low pressure drop.

In “paper B” [124], we investigated the flexibility of the design to perform in different manufacturing methods. The variable radius micromixer design was manufactured both via soft-lithography and also through the DLP 3D-printing method. Due to the resolution limit of the printer, the dimensions of the micromixer were scaled 2.5 times. Even though we knew that these dimensions would decrease the mixing efficiency, we tested if the diffusion would take place visually fast enough to implement a diffusion-based sensor.

The results achieved in “paper B” demonstrate that we can use 3D printed microfluidics to manufacture a portable pH and ionic strength sensor and we could characterize buffered and non-buffered solutions. The results showed that by comparing the diffusion width of the wine (as a sample) and tartaric acid solutions (as reference solutions), it is possible to estimate the total acid concentration in an unknown solution.

Using colorimetric analysis, we built a calibration plot that correlated the diffusion width of different tartaric acids to their known molarity. The results also illustrated that the sensor was able to detect a broad range of molarities, from 1.0 M to 0.1 M and lower. The proposed design was also capable of measuring the ionic strength of wine solutions, based on monitoring the diffusion width and comparing it to the tartaric acid diffusion widths and the pH by monitoring the mean green intensity profile of the reaction between the pH indicator and the sample at a given flowrate.

Other than the non-buffered solutions, this assay was repeated for the buffered solutions as well. Similar test configurations were adopted for evaluating the buffering capacity of HEPES solutions. The assay showed that the proposed µTAS setup was also able to determine the pH of the solutions as well as their buffering capacity.

“Paper A” and specially “Paper B” had proven the possibility to use diffusion-based sensors to evaluate the concentration of species using a cross-inlet configuration and a diffusive channel (variable radius spiral). However, in both papers a precise control of flow rates was needed to achieve the appropriate Reynolds regime to ensure maximum efficiency and this was achieved thanks to the use of syringe pumps, which limited the portability of the device. Introducing paper as a substrate, would eliminate the need of this equipment but introduces the uncertainty on the flow control.

In “Paper C” [128], we propose to take advantage of 3D printing technologies to gain control on the fluid flow and synchronize the contact time of the paper substrate and the understudy solutions. Also, we use CFD analysis of the flow generated in the porous media for a better understanding of the effects of the inlet geometry on the generated flow.

A CFD model, which was based on the Whatman 5 characteristics, was developed and validated as a useful tool for the design of paper diffusion-based sensors. The model was used to evaluate the effect of the substrate geometry on the flow within the porous medium and to develop a sensor setup that could compare the ionic concentration of an unknown solution to a known solution, quantitatively.

According to the numerical models, decreasing the angles between the inlets resulted in smaller dead zones in the main channel and consequently, providing a wider diffusion width. Whereas, the 30-degree model provided a 14.6% wider diffusion width compared to the 90-degree model.

Other than the diffusion width, the experimental assays also showed that less time was required to develop the diffusion zone measurable with colorimetric analysis if the inlets' angles were smaller. For instance, the 30-degree model required 57% less time to develop a diffusion zone compared to the 90-degree model. Moreover, models with inlet angles larger than 30◦ were unable to detect concentrations below 0.5 M. These models were validated experimentally and the experimental results validated the proposed model.

Therefore, the 30-degree model was implemented in Whatman 5 paper and used as a paper diffusion-based sensor to evaluate the ionic strength of wines (as the sample) by comparison to different tartaric acid solutions (as reference solutions). This novel sensor presents a limit of detection of 6.2 Tartaric Acid g/L and it is capable of evaluating the ionic concentration of commercial wines in 120 s without the need of any external equipment or trained personnel.

8. Future investigations

As it was mentioned in the previous sections, we managed to address the objectives such as, introducing a new micromixer with minimum reliance on external energy sources, probing the appropriate fabrication methods, introducing an ionic strength and pH sensor based on the capabilities of the developed microfluidic platform and extending the flow control experience to the paper-based analytical devices. However, the potential of these studies is not limited to the aforementioned projects.

The model developed in “Paper C” can be modified to analyze the effect of different substrates (i.e. other paper characteristics such as different fiber length, diameter or porosity) to further optimize the turnaround time of the results and increase the sensitivity of the sensor.

The strategy developed in “Paper B” and “Paper C” can be applied to detect other species, maybe in smaller sizes. The results of using the same model but applied to different paper substrates can help us to tune the generated capillary flow and therefore enhance the accuracy and the results turnaround time.

The strategy developed in “Paper C” proposed for wines and in a certain range of acidity levels can be extended to other acidity ranges by enhancing the mixing process or lowering the resolution of the channels and splitting the sample to more detection areas.

The geometry proposed in “Paper A” has shown to be compatible with different manufacturing methods. The proposed geometry was printed using DLP technology, with 3D features only in the XY plane. Exploring the possibility of introducing a third-dimension expansion (Z direction) and fabricating via improved resolution 3D-printers, can enhance even further the mixing efficiency or allow a more compact design with less loops and same efficiency.

The proposed geometry has only been investigated as a sensor, but the need of mixing is not limited to the ionic strength measurements or pH measurements. For instance, in the field of drug delivery, the use of hydrogels that change their viscosity depending on their pH environment that they are growing in. These hydrogels are usually injected at high pH, at which they are liquid, and lowering the pH to human body level (pH 7), solidifies the liquid hydrogel. The micromixers combined with micro particle image velocimetry are two techniques or tools that can help in study of the time evolution of this process and how to improve this discipline.

Similarly, in wearables discipline, nowadays there is the trend to use sweat as a body fluid to analyze different analytes, but some are in huge concentrations in sweat (i.e lactate) and the current blood sensors are out of range. Using compact and efficient mixers to bring the measurement levels close to blood levels will speed up the development of wearable technology.

9. Bibliography

[1] X. Niu, Y.-K. Lee, Efficient spatial-temporal chaotic mixing in microchannels, J. Micromechanics Microengineering. 13 (2003) 454.

[2] H. Van Phan, M.B. Coşkun, M. Şeşen, G. Pandraud, A. Neild, T. Alan, Vibrating membrane with discontinuities for rapid and efficient microfluidic mixing, Lab Chip. 15 (2015) 4206–4216. https://doi.org/10.1039/c5lc00836k.

[3] S. Qian, H.H. Bau, Magneto-hydrodynamic stirrer for stationary and moving fluids, Sensors Actuators, B Chem. 106 (2005) 859–870. https://doi.org/10.1016/j.snb.2004.07.011.

[4] J.J. Huang, Y.J. Lo, C.M. Hsieh, U. Lei, C.I. Li, C.W. Huang, An electro-thermal micro mixer, in: 2011 6th IEEE Int. Conf. Nano/Micro Eng. Mol. Syst., 2011: pp. 919–922.

[5] M. Bayareh, M.N. Ashani, A. Usefian, Active and passive micromixers: A comprehensive review, Chem. Eng. Process. - Process Intensif. 147 (2020) 1–19. https://doi.org/10.1016/j.cep.2019.107771.

[6] G. Cai, L. Xue, H. Zhang, J. Lin, A review on micromixers, Micromachines. 8 (2017). https://doi.org/10.3390/mi8090274.

[7] J. Wu, M. Gu, Microfluidic sensing: state of the art fabrication and detection techniques, J. Biomed. Opt. 16 (2011) 080901. https://doi.org/10.1117/1.3607430.

[8] B.K. Gale, A.R. Jafek, C.J. Lambert, B.L. Goenner, H. Moghimifam, U.C. Nze, S.K. Kamarapu, A review of current methods in microfluidic device fabrication and future commercialization prospects, Inventions. 3 (2018). https://doi.org/10.3390/inventions3030060.

[9] S. Karimi, P. Mehrdel, J. Farré-Lladós, J. Casals-Terré, A passive portable microfluidic blood-plasma separator for simultaneous determination of direct and indirect ABO/Rh blood typing, Lab Chip. 19 (2019). https://doi.org/10.1039/c9lc00690g.

[10] M. Ståhl, B.L. Åslund, Å.C. Rasmuson, Reaction crystallization kinetics of benzoic acid, AIChE J. 47 (2001) 1544–1560.

[11] K. Benz, K.-P. Jäckel, K.-J. Regenauer, J. Schiewe, K. Drese, W. Ehrfeld, V. Hessel, H. Löwe, Utilization of micromixers for extraction processes, Chem. Eng. \& Technol. Ind. Chem. Equipment-Process Eng. 24 (2001) 11–17.

[12] R. Baudoin, A. Legendre, S. Jacques, J. Cotton, F. Bois, E. Leclerc, Evaluation of a liver microfluidic biochip to predict in vivo clearances of seven drugs in rats, J. Pharm. Sci. 103 (2014) 706–718.

[13] G. Czilwik, I. Schwarz, M. Keller, S. Wadle, S. Zehnle, F. Von Stetten, D. Mark, R. Zengerle, N. Paust, Microfluidic vapor-diffusion barrier for pressure reduction in fully closed PCR modules, Lab Chip. 15 (2015) 1084–1091.

[14] S.-J. Kim, F. Wang, M.A. Burns, K. Kurabayashi, Temperature-programmed natural convection for micromixing and biochemical reaction in a single microfluidic chamber, Anal. Chem. 81 (2009)

4510–4516.

[15] R.H. Liu, R. Lenigk, R.L. Druyor-Sanchez, J. Yang, P. Grodzinski, Hybridization enhancement using cavitation microstreaming, Anal. Chem. 75 (2003) 1911–1917.

[16] J. Mok, M.N. Mindrinos, R.W. Davis, M. Javanmard, Digital microfluidic assay for protein detection, Proc. Natl. Acad. Sci. 111 (2014) 2110–2115.

[17] G.A. Cooksey, J. Atencia, Pneumatic valves in folded 2D and 3D fluidic devices made from plastic films and tapes, Lab Chip. 14 (2014) 1665–1668.

[18] A. Moody, Rapid diagnostic tests for malaria parasites, Clin. Microbiol. Rev. 15 (2002) 66–78.

[19] D. Bell, C. Wongsrichanalai, J.W. Barnwell, Ensuring quality and access for malaria diagnosis: how can it be achieved?, Nat. Rev. Microbiol. 4 (2006) 682–695.

[20] M.E. Rafael, T. Taylor, A. Magill, Y.-W. Lim, F. Girosi, R. Allan, Reducing the burden of childhood malaria in Africa: the role of improved, Nature. 444 (2006) 39–48.

[21] M. Stone, J. Bainbridge, A.M. Sanchez, S.M. Keating, A. Pappas, W. Rountree, C. Todd, S. Bakkour, M. Manak, S.A. Peel, others, Comparison of detection limits of fourth-and fifth-generation combination HIV antigen-antibody, p24 antigen, and viral load assays on diverse HIV isolates, J. Clin. Microbiol. 56 (2018).

[22] X. Qiu, L. Sokoll, P. Yip, D.J. Elliott, R. Dua, P. Mohr, X.Y. Wang, M. Spencer, P. Swanson, G.J. Dawson, others, Comparative evaluation of three FDA-approved HIV Ag/Ab combination tests using a genetically diverse HIV panel and diagnostic specimens, J. Clin. Virol. 92 (2017) 62–68.

[23] N.G. Campos, V. Tsu, J. Jeronimo, M. Mvundura, J.J. Kim, Estimating the value of point-of-care HPV testing in three low-and middle-income countries: a modeling study, BMC Cancer. 17 (2017) 1–12.

[24] C. Mahé, L. Gaffikin, Screening test accuracy studies: how valid are our conclusions? Application to visual inspection methods for cervical screening, Cancer Causes \& Control. 16 (2005) 657–666.

[25] L.A. Denny, R. Sankaranarayanan, H. De Vuyst, J.J. Kim, P.O. Adefuye, L. Alemany, I.F. Adewole, O.A. Awolude, G. Parham, S. de Sanjosé, others, Recommendations for cervical cancer prevention in sub-saharan Africa, Vaccine. 31 (2013) F73--F74.

[26] D. Sebba, A.G. Lastovich, M. Kuroda, E. Fallows, J. Johnson, A. Ahouidi, A.N. Honko, H. Fu, R. Nielson, E. Carruthers, others, A point-of-care diagnostic for differentiating Ebola from endemic febrile diseases, Sci. Transl. Med. 10 (2018).

[27] P. Brangel, A. Sobarzo, C. Parolo, B.S. Miller, P.D. Howes, S. Gelkop, J.J. Lutwama, J.M. Dye, R.A. McKendry, L. Lobel, others, A serological point-of-care test for the detection of IgG antibodies against Ebola virus in human survivors, ACS Nano. 12 (2018) 63–73.

[28] S.D. Lawn, M.P. Nicol, Xpert®MTB/RIF assay: development, evaluation and implementation of a new rapid molecular diagnostic for tuberculosis and rifampicin resistance, Future Microbiol. 6 (2011) 1067–1082.

[29] M.G. Mauk, J. Song, H.H. Bau, C. Liu, Point-of-care molecular test for Zika infection, Clin. Lab. Int. 41 (2017) 25.

[30] C.M. Denkinger, I. Nicolau, A. Ramsay, P. Chedore, M. Pai, Are peripheral microscopy centres ready

for next generation molecular tuberculosis diagnostics?, Eur. Respir. J. 42 (2013) 544–547.

[31] N. Nath, C. Wunderlich, F.W. Darr, D.K. Douglas, R.Y. Dodd, Immunoglobulin level in donor blood reactive for antibodies to human immunodeficiency virus., J. Clin. Microbiol. 25 (1987) 364–369.

[32] T.A. Rakusan, R.H. Parrott, J.L. Sever, Limitations in the laboratory diagnosis of vertically acquired HIV infection., J. Acquir. Immune Defic. Syndr. 4 (1991) 116–121.

[33] S. Kellerman, S. Essajee, HIV testing for children in resource-limited settings: what are we waiting for?, PLoS Med. 7 (2010) e1000285.

[34] S.H. Wong, M.C.L. Ward, C.W. Wharton, Micro T-mixer as a rapid mixing micromixer, Sensors Actuators B Chem. 100 (2004) 359–379.

[35] S.S. Hsieh, J.W. Lin, J.H. Chen, Mixing efficiency of Y-type micromixers with different angles, Int. J. Heat Fluid Flow. 44 (2013) 130–139. https://doi.org/10.1016/j.ijheatfluidflow.2013.05.011.

[36] C.-C. Hong, J.-W. Choi, C.H. Ahn, A novel in-plane passive microfluidic mixer with modified Tesla structures, Lab Chip. 4 (2004) 109–113.

[37] A.-S. Yang, F.-C. Chuang, C.-K. Chen, M.-H. Lee, S.-W. Chen, T.-L. Su, Y.-C. Yang, A high-performance micromixer using three-dimensional Tesla structures for bio-applications, Chem. Eng. J. 263 (2015) 444–451.

[38] D. Gobby, P. Angeli, A. Gavriilidis, Mixing characteristics of T-type microfluidic mixers INSTITUTE OF PHYSICS PUBLISHING JOURNAL OF MICROMECHANICS AND MICROENGINEERING Mixing characteristics of T-type microfluidic mixers, J. Micromech. Microeng. 11 (2001) 126–132. http://iopscience.iop.org/0960-1317/11/2/307%0Awww.iop.org/Journals/jm.

[39] H. Wang, P. Iovenitti, E. Harvey, S. Masood, Optimizing layout of obstacles for enhanced mixing in microchannels, Smart Mater. Struct. 11 (2002) 662.

[40] A. Alam, A. Afzal, K.-Y. Kim, Mixing performance of a planar micromixer with circular obstructions in a curved microchannel, Chem. Eng. Res. Des. 92 (2014) 423–434.

[41] K. Karthikeyan, L. Sujatha, N.M. Sudharsan, Numerical modeling and parametric optimization of micromixer for low diffusivity fluids, Int. J. Chem. React. Eng. 16 (2017).

[42] X. Chen, S. Zhang, Z. Wu, Y. Zheng, A novel Koch fractal micromixer with rounding corners structure, Microsyst. Technol. 25 (2019) 2751–2758. https://doi.org/10.1007/s00542-019-04296-4.

[43] X. Feng, Y. Ren, H. Jiang, An effective splitting-and-recombination micromixer with self-rotated contact surface for wide Reynolds number range applications, Biomicrofluidics. 7 (2013). https://doi.org/10.1063/1.4827598.

[44] A. Afzal, K.-Y. Kim, Performance evaluation of three types of passive micromixer with convergent-divergent sinusoidal walls, J. Mar. Sci. Technol. 22 (2014) 680–686.

[45] S. Zhang, X. Chen, Z. Wu, Y.U.E. Zheng, Numerical study on koch fractal baffle micromixer, Fractals. 27 (2019). https://doi.org/10.1142/S0218348X19500269.

[46] T. Scherr, C. Quitadamo, P. Tesvich, D.S.-W. Park, T. Tiersch, D. Hayes, J.-W. Choi, K. Nandakumar, W.T. Monroe, A planar microfluidic mixer based on logarithmic spirals, J. Micromechanics

Microengineering. 22 (2012) 55019.

[47] R. Milotin, D. Lelea, The passive mixing phenomena in Microtubes with baffle configuration, Procedia Technol. 22 (2016) 243–250.

[48] B. Mondal, S.K. Mehta, P.K. Patowari, S. Pati, Numerical study of mixing in wavy micromixers: comparison between raccoon and serpentine mixer, Chem. Eng. Process. Intensif. 136 (2019) 44–61.

[49] A. Afzal, K.-Y. Kim, Passive split and recombination micromixer with convergent--divergent walls, Chem. Eng. J. 203 (2012) 182–192.

[50] T.S. Sheu, S.J. Chen, J.J. Chen, Mixing of a split and recombine micromixer with tapered curved microchannels, Chem. Eng. Sci. 71 (2012) 321–332.

[51] A. Hatch, A.E. Kamholz, K.R. Hawkins, M.S. Munson, E.A. Schilling, B.H. Weigl, P. Yager, A rapid diffusion immunoassay in a T-sensor, Nat. Publ. Gr. 19 (2001) 461–465.

[52] M. Nimafar, V. Viktorov, M. Martinelli, Experimental comparative mixing performance of passive micromixers with H-shaped sub-channels, Chem. Eng. Sci. 76 (2012) 37–44. https://doi.org/10.1016/j.ces.2012.03.036.

[53] B. Hama, G. Mahajan, P.S. Fodor, M. Kaufman, C.R. Kothapalli, Evolution of mixing in a microfluidic reverse-staggered herringbone micromixer, Microfluid. Nanofluidics. 22 (2018) 1–14. https://doi.org/10.1007/s10404-018-2074-0.

[54] M.K. Parsa, F. Hormozi, Experimental and CFD modeling of fluid mixing in sinusoidal microchannels with different phase shift between side walls, J. Micromechanics Microengineering. 24 (2014). https://doi.org/10.1088/0960-1317/24/6/065018.

[55] W. Raza, K.Y. Kim, Unbalanced Split and Recombine Micromixer with Three-Dimensional Steps, Ind. Eng. Chem. Res. 59 (2020) 3744–3756. https://doi.org/10.1021/acs.iecr.9b00682.

[56] J. Yang, L. Qi, Y. Chen, H. Ma, Design and fabrication of a three dimensional spiral micromixer, Chinese J. Chem. 31 (2013) 209–214. https://doi.org/10.1002/cjoc.201200922.

[57] J.W. Wu, H.M. Xia, Y.Y. Zhang, S.F. Zhao, P. Zhu, Z.P. Wang, An efficient micromixer combining oscillatory flow and divergent circular chambers, Microsyst. Technol. 25 (2019) 2741–2750.

[58] Z. Li, S.-J. Kim, Pulsatile micromixing using water-head-driven microfluidic oscillators, Chem. Eng. J. 313 (2017) 1364–1369.

[59] N. Nam-Trung, W. Zhigang, Micromixers: a review, J. Micromechanics Microengineering. 15 (2005) R1.

[60] Z. Yang, S. Matsumoto, H. Goto, M. Matsumoto, R. Maeda, Ultrasonic micromixer for microfluidic systems, Sensors Actuators A Phys. 93 (2001) 266–272.

[61] D. Ahmed, X. Mao, J. Shi, B.K. Juluri, T.J. Huang, A millisecond micromixer via single-bubble-based acoustic streaming, Lab Chip. 9 (2009) 2738–2741.

[62] S.S. Wang, Z.J. Jiao, X.Y. Huang, C. Yang, N.T. Nguyen, Acoustically induced bubbles in a microfluidic channel for mixing enhancement, Microfluid. Nanofluidics. 6 (2009) 847–852.

[63] L.-S. Jang, S.-H. Chao, M.R. Holl, D.R. Meldrum, Microfluidic circulatory flows induced by resonant

vibration of diaphragms, Sensors Actuators A Phys. 122 (2005) 141–148.

[64] G.G. Yaralioglu, I.O. Wygant, T.C. Marentis, B.T. Khuri-Yakub, Ultrasonic mixing in microfluidic channels using integrated transducers, Anal. Chem. 76 (2004) 3694–3698.

[65] Y.Q. Fu, J.K. Luo, N.-T. Nguyen, A.J. Walton, A.J. Flewitt, X.-T. Zu, Y. Li, G. McHale, A. Matthews, E. Iborra, others, Advances in piezoelectric thin films for acoustic biosensors, acoustofluidics and lab-on-chip applications, Prog. Mater. Sci. 89 (2017) 31–91.

[66] A. Qi, L.Y. Yeo, J.R. Friend, Interfacial destabilization and atomization driven by surface acoustic waves, Phys. Fluids. 20 (2008) 74103.

[67] K.M. Ang, L.Y. Yeo, Y.M. Hung, M.K. Tan, Amplitude modulation schemes for enhancing acoustically-driven microcentrifugation and micromixing, Biomicrofluidics. 10 (2016) 54106.

[68] T.-D. Luong, V.-N. Phan, N.-T. Nguyen, High-throughput micromixers based on acoustic streaming induced by surface acoustic wave, Microfluid. Nanofluidics. 10 (2011) 619–625.

[69] M. Ballard, D. Owen, Z.G. Mills, P.J. Hesketh, A. Alexeev, Orbiting magnetic microbeads enable rapid microfluidic mixing, Microfluid. Nanofluidics. 20 (2016) 1–13.

[70] K.Y. Lee, S. Park, Y.R. Lee, S.K. Chung, Magnetic droplet microfluidic system incorporated with acoustic excitation for mixing enhancement, Sensors Actuators A Phys. 243 (2016) 59–65.

[71] D. Nouri, A. Zabihi-Hesari, M. Passandideh-Fard, Rapid mixing in micromixers using magnetic field, Sensors Actuators A Phys. 255 (2017) 79–86.

[72] M. Hejazian, N.-T. Nguyen, A rapid magnetofluidic micromixer using diluted ferrofluid, Micromachines. 8 (2017) 37.

[73] K. Petkovic, G. Metcalfe, H. Chen, Y. Gao, M. Best, D. Lester, Y. Zhu, Rapid detection of Hendra virus antibodies: an integrated device with nanoparticle assay and chaotic micromixing, Lab Chip. 17 (2017) 169–177.

[74] C. Kumar, M. Hejazian, C. From, S.C. Saha, E. Sauret, Y. Gu, N.-T. Nguyen, Modeling of mass transfer enhancement in a magnetofluidic micromixer, Phys. Fluids. 31 (2019) 63603.

[75] L.M. Fu, C.H. Tsai, K.P. Leong, C.Y. Wen, Rapid micromixer via ferrofluids, Phys. Procedia. 9 (2010) 270–273.

[76] F. Liu, J. Zhang, G. Alici, S. Yan, R. Mutlu, W. Li, T. Yan, An inverted micro-mixer based on a magnetically-actuated cilium made of Fe doped PDMS, Smart Mater. Struct. 25 (2016) 95049.

[77] S.K. Saroj, M. Asfer, A. Sunderka, P.K. Panigrahi, Two-fluid mixing inside a sessile micro droplet using magnetic beads actuation, Sensors Actuators A Phys. 244 (2016) 112–120.

[78] S. Boroun, F. Larachi, Enhancing liquid micromixing using low-frequency rotating nanoparticles, AIChE J. 63 (2017) 337–346.

[79] M. Bayareh, A. Usefian, A. Ahmadi Nadooshan, Rapid mixing of Newtonian and non-Newtonian fluids in a three-dimensional micro-mixer using non-uniform magnetic field, J. Heat Mass Transf. Res. 6 (2019) 55–61.

[80] T.G. Kang, M.A. Hulsen, P.D. Anderson, J.M.J. Den Toonder, H.E.H. Meijer, Chaotic mixing induced by a magnetic chain in a rotating magnetic field, Phys. Rev. E - Stat. Nonlinear, Soft Matter Phys.

76 (2007) 1–11. https://doi.org/10.1103/PhysRevE.76.066303.

[81] C.Y. Chen, C.Y. Lin, Y.T. Hu, Inducing 3D vortical flow patterns with 2D asymmetric actuation of artificial cilia for high-performance active micromixing, Exp. Fluids. 55 (2014) 1–9. https://doi.org/10.1007/s00348-014-1765-x.

[82] N. Veldurthi, S. Chandel, T. Bhave, D. Bodas, Computational fluid dynamic analysis of poly(dimethyl siloxane) magnetic actuator based micromixer, Sensors Actuators, B Chem. 212 (2015) 419–424. https://doi.org/10.1016/j.snb.2015.02.048.

[83] D. Owen, M. Ballard, A. Alexeev, P.J. Hesketh, Rapid microfluidic mixing via rotating magnetic microbeads, Sensors Actuators, A Phys. 251 (2016) 84–91. https://doi.org/10.1016/j.sna.2016.09.040.

[84] H.-J. Kang, B. Choi, Development of the MHD micropump with mixing function, Sensors Actuators A Phys. 165 (2011) 439–445.

[85] H. Jeon, M. Massoudi, J. Kim, Magneto-hydrodynamics-driven mixing of a reagent and a phosphate-buffered solution: A computational study, Appl. Math. Comput. 298 (2017) 261–271.

[86] C.Y. Lee, L.M. Fu, Recent advances and applications of micromixers, Sensors Actuators, B Chem. 259 (2018) 677–702. https://doi.org/10.1016/j.snb.2017.12.034.

[87] C. Liu, Y. Li, B.F. Liu, Micromixers and their applications in kinetic analysis of biochemical reactions, Talanta. 205 (2019) 120136. https://doi.org/10.1016/j.talanta.2019.120136.

[88] H.-S. Kim, H.-O. Kim, Y.-J. Kim, Effect of electrode configurations on the performance of electro-hydrodynamic micromixer, in: Int. Conf. Nanochannels, Microchannels, Minichannels, 2018: p. V001T02A005.

[89] A.O. El Moctar, N. Aubry, J. Batton, Electro-hydrodynamic micro-fluidic mixer, Lab Chip. 3 (2003) 273–280.

[90] J. Zhang, G. He, F. Liu, Electro-osmotic flow and mixing in heterogeneous microchannels, Phys. Rev. E. 73 (2006) 56305.

[91] S. Ebrahimi, A. Hasanzadeh-Barforoushi, A. Nejat, F. Kowsary, Numerical study of mixing and heat transfer in mixed electroosmotic/pressure driven flow through T-shaped microchannels, Int. J. Heat Mass Transf. 75 (2014) 565–580.

[92] S. Bhattacharyya, S. Bera, Combined electroosmosis-pressure driven flow and mixing in a microchannel with surface heterogeneity, Appl. Math. Model. 39 (2015) 4337–4350.

[93] R. Peng, D. Li, Effects of ionic concentration gradient on electroosmotic flow mixing in a microchannel, J. Colloid Interface Sci. 440 (2015) 126–132.

[94] A.A. Yazdi, A. Sadeghi, M.H. Saidi, Electrokinetic mixing at high zeta potentials: Ionic size effects on cross stream diffusion, J. Colloid Interface Sci. 442 (2015) 8–14.

[95] A. Shamloo, M. Mirzakhanloo, M.R. Dabirzadeh, Numerical simulation for efficient mixing of newtonian and non-newtonian fluids in an electro-osmotic micro-mixer, Chem. Eng. Process. Intensif. 107 (2016) 11–20.

[96] K. Matsubara, T. Narumi, Microfluidic mixing using unsteady electroosmotic vortices produced by

a staggered array of electrodes, Chem. Eng. J. 288 (2016) 638–647.

[97] Z. Kazemi, S. Rashidi, J.A. Esfahani, Effect of flap installation on improving the homogeneity of the mixture in an induced-charge electrokinetic micro-mixer, Chem. Eng. Process. Process Intensif. 121 (2017) 188–197.

[98] A. Usefian, M. Bayareh, A. Shateri, N. Taheri, Numerical study of electro-osmotic micro-mixing of Newtonian and non-Newtonian fluids, J. Brazilian Soc. Mech. Sci. Eng. 41 (2019) 1–10.

[99] W. Zhao, F. Yang, K. Wang, J. Bai, G. Wang, Rapid mixing by turbulent-like electrokinetic microflow, Chem. Eng. Sci. 165 (2017) 113–121.

[100] K. Zhang, Y. Ren, L. Hou, X. Feng, X. Chen, H. Jiang, An efficient micromixer actuated by induced-charge electroosmosis using asymmetrical floating electrodes, Microfluid. Nanofluidics. 22 (2018) 1–11.

[101] Y. Daghighi, D. Li, Numerical study of a novel induced-charge electrokinetic micro-mixer, Anal. Chim. Acta. 763 (2013) 28–37.

[102] E. Choi, B. Kim, J. Park, High-throughput microparticle separation using gradient traveling wave dielectrophoresis, J. Micromechanics Microengineering. 19 (2009) 125014.

[103] D. Kim, A. Raj, L. Zhu, R.I. Masel, M.A. Shannon, Non-equilibrium electrokinetic nanofluidic mixers, in: 2008 IEEE 21st Int. Conf. Micro Electro Mech. Syst., 2008: pp. 630–632.

[104] A. Usefian, M. Bayareh, Numerical and experimental study on mixing performance of a novel electro-osmotic micro-mixer, Meccanica. 54 (2019) 1149–1162.

[105] J. Deval, P. Tabeling, C.-M. Ho, A dielectrophoretic chaotic mixer, in: Tech. Dig. MEMS 2002 IEEE Int. Conf. Fifteenth IEEE Int. Conf. Micro Electro Mech. Syst. (Cat. No. 02CH37266), 2002: pp. 36–39.

[106] C.P. Cheng, R.J. Herfkens, C.A. Taylor, Abdominal aortic hemodynamic conditions in healthy subjects aged 50-70 at rest and during lower limb exercise: In vivo quantification using MRI, Atherosclerosis. 168 (2003) 323–331. https://doi.org/10.1016/S0021-9150(03)00099-6.

[107] M. Zhang, W. Zhang, Z. Wu, Y. Shen, Y. Chen, C. Lan, F. Li, W. Cai, Comparison of micro-mixing in time pulsed Newtonian fluid and viscoelastic fluid, Micromachines. 10 (2019). https://doi.org/10.3390/mi10040262.

[108] S. Orbay, A. Ozcelik, J. Lata, M. Kaynak, M. Wu, T.J. Huang, Mixing high-viscosity fluids via acoustically driven bubbles, J. Micromechanics Microengineering. 27 (2017) 15008. https://doi.org/10.1088/0960-1317/27/1/015008.

[109] P. Nath, D. Fung, Y.A. Kunde, A. Zeytun, B. Branch, G. Goddard, Rapid prototyping of robust and versatile microfluidic components using adhesive transfer tapes, Lab Chip. 10 (2010) 2286–2291.

[110] D.J. Kinahan, L.A.N. Julius, C. Schoen, T. Dreo, J. Ducrée, Automated DNA purification and multiplexed lamp assay preparation on a centrifugal microfluidic "Lab-on-a-Disc" platform, in: 2018 IEEE Micro Electro Mech. Syst., 2018: pp. 1134–1137.

[111] D.I. Walsh III, D.S. Kong, S.K. Murthy, P.A. Carr, Enabling microfluidics: from clean rooms to makerspaces, Trends Biotechnol. 35 (2017) 383–392.

[112] M.A. Mahmud, E.J.M. Blondeel, M. Kaddoura, B.D. MacDonald, Features in microfluidic paper-based devices made by laser cutting: How small can they be?, Micromachines. 9 (2018) 1–12. https://doi.org/10.3390/mi9050220.

[113] M. Serra, I. Pereiro, A. Yamada, J.-L. Viovy, S. Descroix, D. Ferraro, A simple and low-cost chip bonding solution for high pressure, high temperature and biological applications, Lab Chip. 17 (2017) 629–634.

[114] V.C. Pinto, P.J. Sousa, V.F. Cardoso, G. Minas, Optimized SU-8 processing for low-cost microstructures fabrication without cleanroom facilities, Micromachines. 5 (2014) 738–755.

[115] Y.Xia, G.M.Whitesides, Soft lithography, Annu. Rev. Mater. Sci. 28 (1998) 153–184.

[116] V. Faustino, S.O. Catarino, R. Lima, G. Minas, Biomedical microfluidic devices by using low-cost fabrication techniques: A review, J. Biomech. 49 (2016) 2280–2292.

[117] K.M. Weerakoon-Ratnayake, C.E. O'Neil, F.I. Uba, S.A. Soper, Thermoplastic nanofluidic devices for biomedical applications, Lab Chip. 17 (2017) 362–381.

[118] J. Giboz, T. Copponnex, P. Mélé, Microinjection molding of thermoplastic polymers: a review, J. Micromechanics Microengineering. 17 (2007) R96.

[119] A.K. Au, W. Huynh, L.F. Horowitz, A. Folch, 3D-printed microfluidics, Angew. Chemie Int. Ed. 55 (2016) 3862–3881.

[120] S. Waheed, J.M. Cabot, N.P. Macdonald, T. Lewis, R.M. Guijt, B. Paull, M.C. Breadmore, 3D printed microfluidic devices: enablers and barriers, Lab Chip. 16 (2016) 1993–2013.

[121] Y. He, Y. Wu, J. Fu, Q. Gao, J. Qiu, Developments of 3D printing microfluidics and applications in chemistry and biology: a review, Electroanalysis. 28 (2016) 1658–1678.

[122] A. Pilipović, P. Raos, M. Šercer, Experimental analysis of properties of materials for rapid prototyping, Int. J. Adv. Manuf. Technol. 40 (2009) 105–115.

[123] M. Malinauskas, M. Farsari, A. Piskarskas, S. Juodkazis, Ultrafast laser nanostructuring of photopolymers: A decade of advances, Phys. Rep. 533 (2013) 1–31.

[124] P. Mehrdel, S. Karimi, J. Farre-llados, J. Casals-terré, Portable 3D-printed sensor to measure ionic strength and pH in buffered and non-buffered solutions Pouya Mehrdel, Food Chem. (2020) 128583. https://doi.org/10.1016/j.foodchem.2020.128583.

[125] C.K. Dixit, K. Kadimisetty, J. Rusling, 3D-printed miniaturized fluidic tools in chemistry and biology, TrAC - Trends Anal. Chem. 106 (2018) 37–52. https://doi.org/10.1016/j.trac.2018.06.013.

[126] H. Gong, M. Beauchamp, S. Perry, A.T. Woolley, G.P. Nordin, Optical approach to resin formulation for 3D printed microfluidics, RSC Adv. 5 (2015) 106621–106632. https://doi.org/10.1039/c5ra23855b.

[127] B. Ivorra, J.L. Redondo, J.G. Santiago, P.M. Ortigosa, A.M. Ramos, Two- and three-dimensional modeling and optimization applied to the design of a fast hydrodynamic focusing microfluidic mixer for protein folding, Phys. Fluids. 25 (2013). https://doi.org/10.1063/1.4793612.

[128] P. Mehrdel, H. Khosravi, S. Karimi, J.A. López Martínez, J. Casals-terré, Flow control in porous media: From numerical analysis to quantitative μpad for ionic strength measurements, Sensors. 21

(2021). https://doi.org/10.3390/s21103328.

[129] P. Mehrdel, S. Karimi, J. Farré-Lladós, J. Casals-Terré, Novel variable radius spiral-shaped micromixer: From numerical analysis to experimental validation, Micromachines. 9 (2018). https://doi.org/10.3390/mi9110552.

[130] B. Giri, Laboratory methods in microfluidics, 2017.

[131] J. Casals-Terré, J. Farré-Lladós, J.A. López, T. Vidal, M.B. Roncero, Enhanced fully cellulose based forward and reverse blood typing assay, J. Biomed. Mater. Res. - Part B Appl. Biomater. 108 (2020) 439–450. https://doi.org/10.1002/jbm.b.34400.

[132] K. Yazdchi, S. Srivastava, S. Luding, On the validity of the carman-kozeny equation in random fibrous media, Part. Methods II - Fundam. Appl. (2011) 264–273.

[133] F.A. Bettelheim, W.H. Brown, M.K. Campbell, S.O. Farrell, Introduction to Organic and Biochemistry, 2013.

10. Published articles

The following papers are presented, respectively.

Paper A: *"Novel variable radius spiral–shaped micromixer: from numerical analysis to experimental validation"*

Authors: Pouya Mehrdel, Shadi Karimi, Josep Farré-LLadós, Jasmina Casals-Terré

Journal: Micromachines 9 (11), 552 (IF: 2.523)

https://doi.org/10.3390/mi9110552

The article is presented with permission from "Micromachines" journal.

Paper B: *"Portable 3D-printed sensor to measure ionic strength and pH in buffered and non-buffered solutions"*

Authors: Pouya Mehrdel, Shadi Karimi, Josep Farré-LLadós, Jasmina Casals-Terré

Journal: Food Chemistry 344, 128583 (IF: 6.306)

https://doi.org/10.1016/j.foodchem.2020.128583

The article is presented with permission from "Food Chemistry" Journal.

Paper C: *"Flow Control in Porous Media: From Numerical Analysis to Quantitative µPAD for Ionic Strength Measurements"*

Authors: Pouya Mehrdel, Hamid Khosravi, Shadi Karimi, Joan Antoni López Martínez, Jasmina Casals-Terré

Journal: Sensors 21 (10), 3328 (IF: 3.275)

https://doi.org/10.3390/s21103328

The article is presented with permission from "Sensors" journal.

micromachines

MDPI

Article

Novel Variable Radius Spiral–Shaped Micromixer: From Numerical Analysis to Experimental Validation

Pouya Mehrdel *, Shadi Karimi, Josep Farré-Lladós and Jasmina Casals-Terré

Mechanical Engineering Department—MicroTech Lab., Universitat Politècnica de Catalunya, Colom 7-11 08222 Terrassa, Barcelona, Spain; shadi.karimi@upc.edu (S.K.); josep.farre.llados@upc.edu (J.F.-L.); jasmina.casals@upc.edu (J.C.-T.)

* Correspondence: pouya.mehrdel@upc.edu; Tel.: +34-666-290-677

Received: 24 September 2018; Accepted: 25 October 2018; Published: 27 October 2018

Abstract: A novel type of spiral micromixer with expansion and contraction parts is presented in order to enhance the mixing quality in the low Reynolds number regimes for point-of-care tests (POCT). Three classes of micromixers with different numbers of loops and modified geometries were studied. Numerical simulation was performed to study the flow behavior and mixing performance solving the steady-state Navier–Stokes and the convection-diffusion equations in the Reynolds range of 0.1–10.0. Comparisons between the mixers with and without expansion parts were made to illustrate the effect of disturbing the streamlines on the mixing performance. Image analysis of the mixing results from fabricated micromixers was used to verify the results of the simulations. Since the proposed mixer provides up to 92% of homogeneity at *Re* 1.0, generating 442 Pa of pressure drop, this mixer makes a suitable candidate for research in the POCT field.

Keywords: point-of-care; passive mixer; micromixer; spiral micromixer; mixing

1. Introduction

Microfluidics has opened new horizons in the biological fields [1], such as single cell study [2,3], drug discovery [4], lab-on-a-chip (LOC) and especially in point-of-care testing devices (POCT) development [4–6]. Microfluidics capabilities in flow cytometry has led researchers to conduct assays on evaluating the deformability of cells and permeability of drugs through certain membranes [7,8]. Besides, the controlled nature of the microfluidics has provided the possibility of sorting and sequencing of cells [9,10]. In recent years, development of point-of-care testing devices (POCT) by deployment of lab-on-a-chip (LOC) technology has been found to be noteworthy by the researchers [11]. Reducing the laboratory works and costs, rapid and accurate respond, providing bedside analysis and being user-friendly have been the most well-known characteristics of these devices [11,12]. Micromixers are one of the most important components of such devices. They have proved their efficiency in achieving objectives such as sample preparation, glucose concentration detection, blood plasma mixing, particle concentration detection etc. [13,14].

At high Reynolds number flows, mixing can be enhanced through secondary flows, chaotic advection and Dean vortices, but in microfluidics (laminar flows), mixing relies on diffusion. Therefore, according to the method used to maximize the mixing, micromixers can be classified as active or passive. Active micromixers require an external energy source to stimulate the perturbations in the flow, such as vibrations, and acoustic and electromagnetic stimulations. Passive micromixers do not require an external energy source and hinge on geometrical features of the design for providing a well-mixed mixture [13,14].

A lot of research has been conducted on optimizing the mixing phenomena in micromixers. Some researchers have engaged the features of both types of micromixers in one device. Afzal et al. [15]

investigated the effect of combining pulsatile flow and a bulb-shape geometry on the efficiency of the mixer. In a similar approach, Silva et al. [16] carried out an investigation on a hybrid generation of micromixers, where variable inlet widths were coupled with the pulsed flow. Other researchers focused on the advantage of chaotic advection. For instance, Hermann et al. [17] studied the mixing in three types of split-and-recombine (SAR) micromixers. In the proposed mixers, the 3D structure of the micromixer provided the chance for the flow to split and twist and recombine with the initial flow from another side. Raza et al. [18] showed that a split-and-recombine micromixer with a 3D structure was able to provide high-quality mixtures at Reynolds numbers higher than 30. Chen et al. [19] compared a 3D split-and-recombine micromixer with an in-plane T-mixer and showed the improvement of this method against the simple in-plane mixer. Although hybrid and 3D generation of the mixers are able to provide mixtures with promising homogeneity, the complexity of fabrication and the increased pressure loss practically restricts the applicability of such devices in the development of lab-on-a-chip (LOC) devices and point-of-care tests (POCT).

In planar mixers, researchers mainly follow the increasing contact surface (for low Reynolds number regimes) or induce chaotic advection (for high Reynolds number regimes) to improve the mixing. Julios et al. [20] studied a planar mixer with perpendicular rectangular grooves on the straight microchannel. Alam et al. [21] also performed a similar investigation on the effects of adding rectangular grooves on a curved microchannel. Both studies provided acceptable results, especially on Reynolds number regimes higher than 60. Li et al. [22] studied the impact of putting obstacles on the path of the flow and showed that the placement, size and the angle of the obstacles can determine the performance of mixers in the range of $1 \leq Re \leq 10$, but in higher flow rates the configuration of the obstacles does not play such an important role. Chen et al. [23] included a pattern of pillars in the flow path of the micromixer. The study clarified the relation between the Peclet number and the mixing efficiency. The microchannel with obstacles (higher Peclet number) translated into a higher efficiency mixer. Rahman Nezhad et al. [24] showed that deflecting flow with baffles could be a simple answer for acquiring relatively homogeneous mixtures, when the facilities are not advanced enough to fabricate sophisticated geometries. A study on the combination of gaps and baffles were conducted by Xia et al. [25]. The results showed that the micromixer was able to provide mixtures with significant uniformity at very low Reynolds number ($Re < 1$) and also at high Reynolds numbers ($Re \geq 40$).

An alternative approach analyzed the effect of the geometry and working condition on the flow behavior. Hossain et al. [26] evaluated the mixing phenomena in three planar micromixers in a wide range of Reynolds numbers (0.267–250). This study showed that even though at the Reynolds numbers range of 20–100 the square wave channel provided the highest quality mixture compared to zig-zag and curved channels, at higher Reynolds numbers, the performance of the three mixers was almost identical. Khosravi Parsa et al. [27] investigated the mixing efficiency in a sinusoidal micromixer with respect to the ratio of amplitude to wavelength. The study concluded that at high Reynolds numbers, the geometry of the mixers with higher amplitude and smaller wavelength allowed the Dean vortices to develop in the peak zones. This was later translated into better mixing compared to the other models. Vatankhah [28] evaluated the effect of the channel's cross-section dimensions on the velocity profiles in the channel. An accordion shape micromixer, which is an amended derivation of a zig-zag microchannel, was studied by Cosentino et al. [29]. Their study evaluated the characteristics of the proposed device, with respect to the biological applications and limits. The study indicated that not all the current mixers are suitable for biological and biomedical research, since they cannot provide sufficient mixing and support vital living conditions for cells. Researchers have addressed the problem of providing high quality mixtures at very high or very low Reynolds numbers. The low Reynolds number range ($0.1 \leq Re \leq 10.0$) is the Achilles ankle of micromixers and in all the references the lowest quality is reported in this domain. Moreover, the pressure drop has always been sacrificed in order to achieve a high quality mixture. However, an increased pressure drop might mean increased surface tension, which could damage or modify living cells.

The purpose of this paper is to introduce a micromixer suitable to be mounted on POCTs and LOCs. Since in these applications the Reynolds number is low, diffusion is considered as the main mixing mechanism, and the proposed design enhances the contact surface with a reduced pressure drop to provide tolerable conditions for living cells. The approach used in this study aims to enhance the residence time by enhancing the mixing phenomena using a novel planar spiral shape micromixer with expansion and contraction parts. The purpose of these expansions/contractions is to enhance the diffusion length and modify the velocity profile. Nine different mixers (one-loop, two-loop and three-loops without expansion, with 5% expansion and 10% expansion) have been used in this study to predict an improved performance in the critical working range of Reynolds numbers 0.1 to 10.0.

2. Mixer Design and Numerical Analysis

2.1. Target Models and the Novel Modification

Three different classes of mixers will be studied based on a single loop, two loops and three loops. The successive arc-shaped mixing units are created from two different centers: A and B, see Figure 1a.

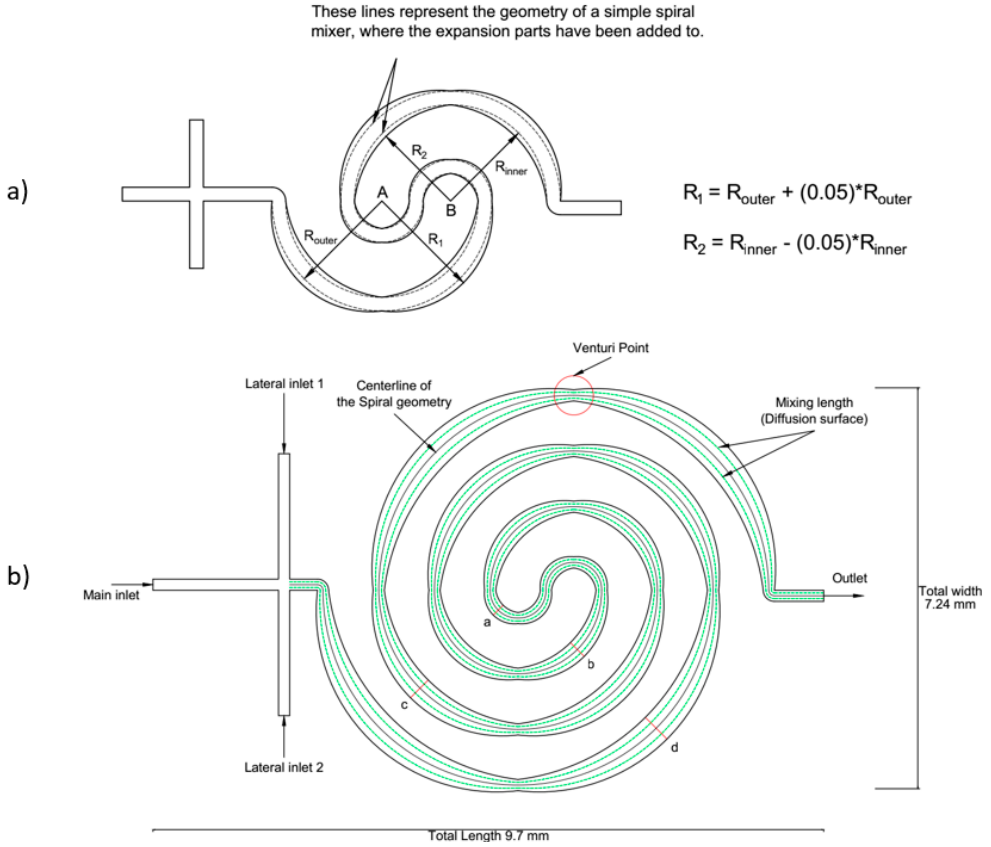

Figure 1. (**a**) Conceptual diagram of the proposed one loop class micromixer, where Rinner and Router represent the radius of inner and outer walls of the basic design of the spiral mixer. (**b**) Schematic view of the three loops mixer with 5% expansion. The width of the channel at the cross-sections a, b, c and d is 250, 350, 450 and 550 μm, respectively.

Expansions will be added to all three mixer classes from the simple spiral design, see Figure 1a (dash line). The initial type is the simple spiral micromixer without expansion (0%). Two more types of expansion/contraction mixers will be studied (5% and 10%). To build this geometry, the outer/inner wall of the microchannel is increased/decreased following a different circle path. These circles have a radius of 5% or 10% (based on the type of the mixer) difference from the original radius. The expansion parts are assumed to reach to maximum values at each arc at the $\pi/4$ and $3\pi/4$ or $5\pi/4$ and $7\pi/4$

(depending on where the curvature is located). In all cases, a minimum width of 200 μm is achieved at nπ/2 points (Venturi point, see Figure 1b).

Shortly after the cross-shaped inlet, the centerline of the microchannel enters in an arc with an angle of 180° around the center point A. Then it continues its path with the same angle, but this time around center point B. This process continues until the arc reaches the exact midpoint between the centerlines A and B. After that, the radius of the arc increases, as the end of the arc recedes from the other center point. This process will go on until the outgoing curvature, which ends at the outlet, reaches the same value of the radius as the ingoing curvature. Table 1 summarizes the overall dimensions of the studied model and the total mixing length.

Table 1. Overall dimensions of the studied models. The height of the channel at all sections is constant and set to 20 μm.

Name of the Device		Device's Length (mm)	Device's Width (mm)	Minimum Mixing Length (mm)
One loop	0% of expansion	5.7	3.2	14
	5% of expansion	5.7	3.23	14
	10% of expansion	5.7	3.26	14
Two loops	0% of expansion	7.7	5.2	29.7
	5% of expansion	7.7	5.22	29.7
	10% of expansion	7.7	5.3	29.7
Three loops	0% of expansion	9.7	7.2	51.7
	5% of expansion	9.7	7.24	51.7
	10% of expansion	9.7	9.36	51.7

The proposed mixer, shown in Figure 1, minimizes the space consumption and does not increase the pressure drop as much as some types of micromixers such as split and recombine mixers and mixers with obstacles on the path of the fluid [17,18,22,23].

Instead of adding commonly used T or Y inlets, a cross-shaped inlet is used in the proposed mixer design. Therefore, a double interfacial area, as depicted in Figure 1b, is achieved by injecting the solvent symmetrically from two sides. The width of the channel in the inlet part is kept constant at 200 μm. The successive arrangement of arc-shape mixing units causes continuous acceleration and deceleration of the fluid flow, i.e., disturbing streamlines and enhancing diffusion.

2.2. Numerical Simulation, Governing Equations and Dimensionless Numbers

Fluid flow in micromixers is generally isothermal, incompressible, Newtonian and laminar. Therefore, it is governed by the continuity equation (Equation (1)), and Momentum (Navier–Stokes) equation (Equation (2)). Convection-Diffusion equation (Equation (3)) is the main physical phenomenon governing the mixing in such systems. In order to calculate the mixing, Equation (3) should be solved together with Equations (1) and (2), so the spreading concentration and the velocity field are coupled. These equations can be expressed, respectively, as:

$$\nabla \vec{U} = 0\,, \tag{1}$$

$$\rho \vec{U} \cdot \nabla \vec{U} = -\nabla P + \mu \nabla^2 \vec{U}\,, \tag{2}$$

$$\rho \vec{U} \cdot \nabla \varphi = D \nabla^2 \varphi\,. \tag{3}$$

In the above equations, $\vec{U}$ is the velocity vector, ρ is the density, P is the pressure, μ is the dynamic viscosity, D is the diffusion coefficient and the φ is the concentration of the species inside the micromixer.

Numerous investigations have established the working conditions of micromixers according to the Reynolds number. This dimensionless number expresses the ratio of the magnitude of the inertial term to the viscous term in the channel.

$$Re = \frac{\rho \vec{U} D_h}{\mu}, \tag{4}$$

where ρ, $\vec{U}$, and μ are density, velocity vector and the dynamic viscosity of the fluid, respectively, and the D_h is the hydraulic diameter of the channel, for which a rectangular duct can be represented as:

$$D_h = \frac{4 \times A_c}{P_w}, \tag{5}$$

where A_c is the surface area of the channel's cross-section, and P_w is the wetted perimeter.

Since the fluid flow in POCT micromixers is within the laminar range, the mixing can therefore be carried out via diffusion and/or advection. Depending on the operating Reynolds number, one of the above-mentioned effects is most likely to be overcome as the leading mixing factor in the device (except for the $Re = 1$, where neither diffusion nor advection has dominance over the other). Peclet number (Pe) denotes the ratio of the advective transport rate to the diffusive transport rate.

$$Pe = \frac{L \times \vec{U}}{D}, \tag{6}$$

where L is the characteristic length.

In order to verify the validity of proposed design, the normalized ratio (σ) of the differences of the mixture and the mixing species to the ideal concentration is measured by analyzing the species distribution along the cross-section at the outlet of the mixer.

$$\sigma = \frac{C_i - \overline{C}}{C_{max} - \overline{C}}, \tag{7}$$

In the above equation, C_i stands for the concentration at each pixel (position on the cross-section of the outlet) and C_{max} is the highest value of concentration in the mixer. Notably, $\overline{C}$ (ideal concentration) represents the median value between the maximum amount and minimum amount of concentration in the mixer, which in this study is set to 0.025 mol/m^3.

$$M \times Q = 1 - \sqrt{\frac{1}{N} \times \sum_{1}^{N} (\sigma^2)}, \tag{8}$$

Mixing quality ($M.Q$) can be obtained through the abovementioned equation, where N is the number of calculating points (evaluating points) over the outlet.

The mixing process is simulated by a commercial CFD-code software, ANSYS FLUENT 15.0 (ANSYS, Inc., Canonsburg, PA, USA), which analyzes the flow and the diffusion in the device. Benefiting from Finite Volume approach, this solver solves the continuity and the momentum equations, at steady-state case, at each control volume with respect to the physical properties of the introduced fluids (such as density, viscosity and diffusivity), initial settings (pressure-induced or given velocity) and boundary conditions (see Table 2 for details about the physical properties). The solver is set to the SIMPLE scheme for Pressure-Velocity coupling. The configuration of the software for solving pressure and momentum modules is set to the second order method and for the scalar to the power law method. The software is capable of introducing scalars as non-reacting agents that do not change the density or the viscosity of the working fluid. The only distinguishing factor of the scalars from the dominant fluid is the different diffusion coefficient, which can be set in the software. The flow is assumed to be in the

laminar range (*Re* smaller than 50) and therefore, Dean vortices are unlikely to take place. The middle inlet is dedicated to water and the diffusive agents are considered to be injected from the side inlets. The accumulative discharge of the side inlets is considered to be the same as the middle inlet.

Table 2. Physical properties of water and diluted ink.

Material	Density (kg/m^3)	Viscosity (kg/(m·s))	Diffusivity in Water (m^2/s)
Water	997	0.001	-
Diluted ink	≈997	≈0.001	5.5×10^{-10} [30]

The 2D geometry is meshed in GAMBIT 2.4.6 software (ANSYS, Inc.) (the device's dimensions are mentioned in Table 1). Therefore, a quadratic mesh scheme followed by a more detailed mesh distribution on the walls and critical points (Venturi points) is adopted. A grid independency analysis is done, based on six different mesh densities and setting the residuals to 10^{-6}. Based on the meshing categories, the number of grid cells varied from 40,000 cells as the low-quality scheme for the one loop model without expansion parts to more than 3.1 million cells as the ultra-fine scheme for the three loops mixer with 10% expansion parts. However, by adopting the fine scheme, these ranges were limited to 289,000 and 1.7 million grid cells. The mean interval size of each cell varied from 10 µm to 2.75 µm (see Table 3). Among those, the meshing configuration that provided 3.75 µm of the mean interval size of each cell resulted in an acceptable answer accuracy (see Figure 2). According to grid independency analysis results, the mesh with cells smaller than 2.75 µm showed no significant change on the results but the required calculation time increased exponentially, see Figure 2.

Table 3. Meshing details of one loop micromixer with 0% of expansion.

Mesh Design	Interval Size of the Mesh	Minimum Orthogonal Quality	Maximum Aspect Ratio	Number of the Cells
Low	10	0.87	2.19	40,223
Medium	7.5	0.872	2.24	71,597
High	5	0.848	2.45	161,473
Fine	3.75	0.818	2.36	289,093
Ultra	3.25	0.83	2.51	383,679
Ultra-fine	2.75	0.839	2.38	537,233

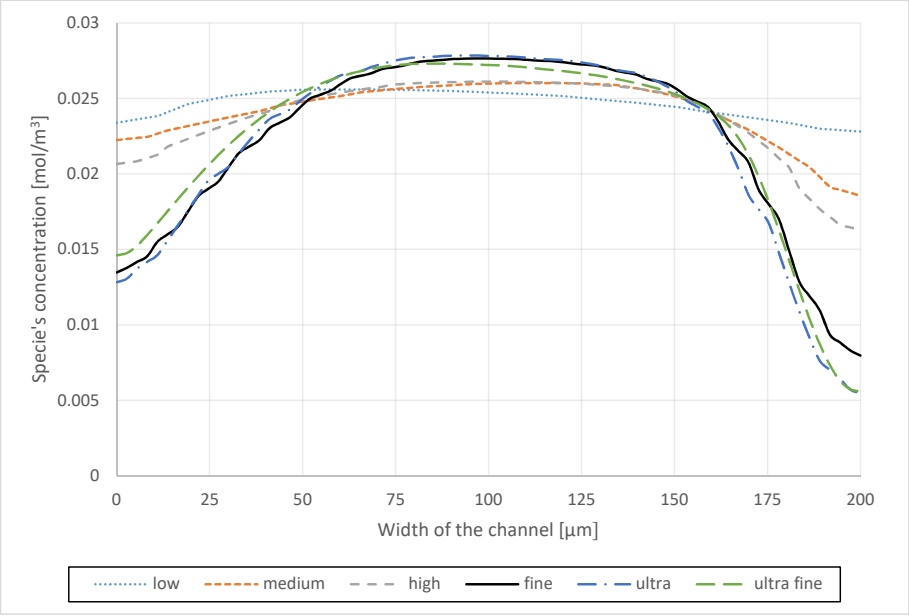

Figure 2. Distribution of the species concentration over a cross-section at the outlet of a simple one loop spiral micro mixer obtained from different meshes.

3. Experimental Section and Fabrication Process

3.1. Fabrication of the Micromixer

Microfluidic mixers can be manufactured following different processes, varying from CO_2 laser ablation to 3D printing techniques. The present investigation uses the soft lithography technique [31]. In this method, a cover glass slide is coated with photo-resist SU-8 (thickness 5-27 µm @GERSTELTEC SARL, Pully, Switzerland) to create a mold with the height of 25 µm. By placing a negative film of the micromixer and beaming UV light on it, the geometry of the device is defined in SU8. The mold fabrication process finishes with sinking the defined pattern in the SU8 developer (PGMEA—Propylene glycol methyl ether acetate @GERSTELTEC SARL, Pully, Switzerland) and cleaning it with propanol. Then, a 10:1 mixture of Silicone Elastomer SYLGARD 184 (@Dow corning, Midland, MI, USA) and its curing agent are poured on the mold, which previously is coated with chlorotrimethylsilane vapor. After baking the polydimethylsiloxane (PDMS) and removing the PDMS from the mold, the connections are created. O_2 Plasma (@Gambetti Vacuum Technology, Binasco (Milan), Italy) is used to bond the hardened PDMS and a cover glass slide. Further precise measurements showed that in some mixers a maximum fabrication error of 2 µm in the width of the channel and 1.5 µm in the height of the channel was occurred.

3.2. Experimental Setup

To generate the flow, two syringe pumps (Graseby 3200- @Smiths, Watford, Hertfordshire, UK- and kdScientific 410-CE- @kdScientific, Holliston, MA, USA) were used. Deionized water and food colorant (a solute of deionized water and food coloring -E133- with the ratio of 2:1) were used as the working fluids. According to the analysis, actual differences of the density and viscosity of the working fluids were negligible. The syringe pumps' calibration was verified by filling a 5-mL container in a determined time, where the container's volume was graded by 0.1-mL lines.

The images of the unmixed and mixed fluids were captured using a Leica microscope (LEICA EZ4D- @Leica, Wetzlar, Germany), with 30× magnification. The microscope was equipped with lights that are able to beam on the top, side and the bottom of the device. The software of the microscope renders the image, varying from black and white view (0% of color saturation), normal view (100% of saturation) and exaggerated view (200% of saturation).

3.3. Image Analysis

Analysis based on images has been widely used in science. It is one of the most common methods to visually illustrate the results of the study. This method has a wide application varying from particle locating and tracking [32], to showing the lysis of cells and to the evaluation of the mixture quality [5].

In this study, pictures obtained of the mixing process are evaluated using ImageJ 1.51k software (National Institutes of Health (NIH), Bethesda, MD, USA). This software analyzes the features of a specified zone or line. In the evaluation process, the pictures are converted to grey scale (through RGB (Red, Green and Blue lights) analysis) and each pixel intensity is evaluated between 0 and 255. To reduce the noise influence, multiple analyses of the same zone from different pictures are carried out, and an average value is obtained as the foundation of the results. Notably, the standard deviation of the analysis is considered as the error range at each pixel.

Furthermore, experimental uncertainty in this work is highly influenced by the image processing section rather than gripping to the established boundary conditions. The results of image analysis showed that the intensity of light in the background varies from center to the corners and in the places where the light intensity was relatively lower compare to the center, higher noise was recorded in the RGB analysis. Background noise due to polarization and light breakdown, when it passed through the cover glass, PDMS layer and microscope lens, was obvious. For tackling this problem, it was decided to manually define a circular zone in the center of the photo capturing area in order to make sure that the minimum and maximum values of grey scale index are the same in the circle for all the

experiments (Dettmer et al. [33] followed a similar process with software for reducing the background noise). This procedure proved to be useful as the reported noise dropped significantly.

4. Results and Discussion

4.1. Simulation Results Based on the Number of Loops

To investigate the influence of expansion in the mixing behavior, a basic spiral mixer was chosen to compare with mixers with different expansion rates up to 10% expansion. Numerical simulations were performed in a range of Reynolds numbers relevant to point-of-care microfluidic devices ($0.1 \leq Re \leq 10.0$). In the range of $Re \leq 0.9$, molecular diffusion is the main mixing factor as discussed in methodology Section 2.2. The other two Reynolds regimes ($Re \approx 1$ and $Re \leq 10$) capture the balance between inertial and viscous terms when they are identical ($Re = 1$) and when the inertial term is dominating the mixing phenomena ($Re = 10$).

Table 4 displays the general efficiency of the mixers calculated according to (Equation (8)), under Reynolds of 0.1, 1.0 and 10.0. The results show that the mixers can provide a mixture with a minimum quality of 62% and a maximum quality of 99.8%. Notably, the minimum quality of the final mixture is reported at the range of *Re* 1.0.

Figure 3 illustrates that by utilizing expansion and contraction, the spiral mixer will increase the mixing length (or in another word the diffusion surface, see Figure 1b dashed line) along the channel. The numerical simulation (Figure 3) shows that since the flow is laminar, the flow lines expand following the profile, and therefore the diffusion surface increases. Therefore, the channel walls' curvature affects the neighboring flow streams. Owing to the tiny scale of the micromixer, any changes in the flow stream's direction and magnitude should not be neglected. As it is illustrated in Table 4, the mixing length of the devices increases by adding expansion parts compared to the basic mixers. The calculated mixing lengths of the studied models increase by a minimum of 27.18%, 17.25% and 9.31% compared to their basic designs. This increased mixing length will improve the performance of the modified spirals compared to simple spiral micromixers, but this will not be the only determining factor in evaluating the mixers' performance.

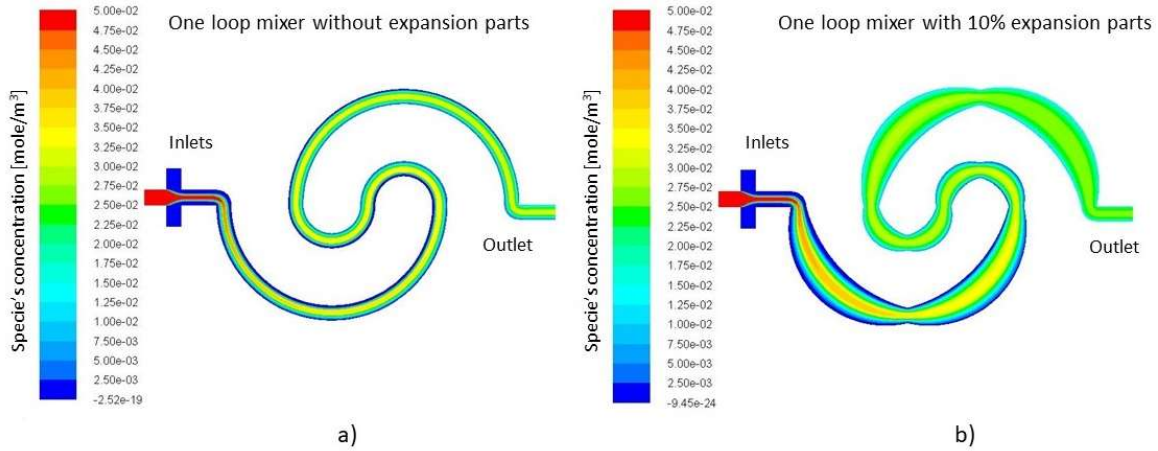

Figure 3. Simulation of the mixing of dyed water injected from inlet 1 and 2 and deionized water from inlet 3 at the Reynolds number of 1.0 (**a**) in one loop mixer without expansion and (**b**) one loop mixer with 10% expansion. The scalar concentration is defined as 0.05 mol for fluid 1 and 0 for fluid 2. The perfect mixing would give a scalar concentration value of 0.025.

Table 4. The efficiency of the mixers calculated according to Equation (8). The Reynolds numbers are based on the accumulative discharge of the inlets at the smallest cross-section of the channel.

Mixer Type		*Re* = 0.1	*Re* = 1.0	*Re* = 10.0
One loop	0% expansion	82.8%	62%	66%
	5% expansion	90.25%	77.6%	81.1%
	10% expansion	93.3%	85%	88.8%
Two loops	0% expansion	90.3%	61.2%	63.3%
	5% expansion	98.3%	96%	96.3%
	10% expansion	98.6%	96.9%	97.7%
Three loops	0% expansion	96%	67%	64.9%
	5% expansion	98.9%	97.9%	98.1%
	10% expansion	99.2%	98.5%	98.9%

In order to analyze the effect of increasing the number of loops and the added expansion parts on the mixing efficiency, the models are tested under similar initial conditions. Figure 4 displays the concentration of species along the cross-section line of the outlet (200 µm). At each graph, the expansion rate and the initial velocity are kept constant. According to the graphs, in the ranges of ($Re < 0.5$) where the viscous term is stronger than the inertial term, the mixing is improved by adding loops. This can be translated into the fact that the species have more time to get diffused inside the channel and that the centrifugal forces are negligible. For the range of ($Re = 1.0$), neither the viscous term nor the inertial term are dominating the flow. Therefore, although adding loops increases the length of the channel, the reinforced inertia of the flow does not allow the components to disperse into its surroundings, and even the added length is not sufficient to provide a significant improvement. This subject is repeated for the cases without expansion parts at ($Re = 10.0$) with a difference. Even though the inertial term is 10 times stronger than the viscous term, it is not enough to cause secondary flows and Dean vortices, which are considered as the main mixing factors in a laminar regime that usually takes place at ($Re > 40.0$) [23].

Table 4 shows that the performance of the mixers at Reynolds 10.0 improves compared to Reynolds 1.0 range; however, this change is not appreciable in Figure 4. Regarding the simulation results (see Table 4), the performance of the simple spiral mixers (without expansion parts) is highly sensitive to the operating conditions. For instance, the efficiency of the mixers may vary from 96% (for 3 loops mixer without expansion parts at *Re* 0.1) to 62% (one loop mixer without expansion parts at *Re* 1.0). This sensitivity is reduced dramatically by adding expansion parts, and a more uniform distribution of the solute can be achieved at the outlet of the mixer in any operation range. In the spiral mixers without expansion parts, the mean difference between the highest quality and the lowest quality is around 20%, while in the one loop mixer with expansion parts, 12% difference is reported between the best and worst performance of the mixer. The difference is minor and around 2% or 1% for two loops and three loops mixers with expansion parts, respectively.

Besides the analysis on the Peclet number at the widest section of the mixers, where the channel reaches its maximum width, it was showed that the increase of the channel width the Peclet number decreases. Due to the definition of the Peclet number, this reduction can be translated into the fact that the diffusive term has been reinforced. In calculation of the Peclet number at the cross section, the characteristic length changes into hydraulic diameter. Due to the fact that the applied modifications on the geometry were in the XY plane and the flow rate was constant, the increase in the hydraulic diameter and the reduction in the flow velocity are not proportional. This description has been well illustrated in Table 5, where by adding 10% expansion parts the advective term has reduced 57% and 76% in one loop mixer and three loop mixers, respectively.

Table 5. Peclet number at the widest cross section of the channel (*Re* 1.0).

Mixer Class	0% Expansion	5% Expansion	10% Expansion
One loop	1836	1092	777
Two loops	1836	859	561
Three loops	1836	708	439

In the methodology, we already described that the initial velocities are set to generate specific Reynolds number regimes based on the minimum cross-section of the channel (Venturi Point). In the expansion and contraction mixers, the flow is driven into sections with larger cross-sections. Nonetheless, the regional Reynolds number reduces according to the definitions of Equations (4) and (5) in these areas. On the other hand, the architecture of the design and the existence of the Venturi points provide a continuous disturbance in the velocity profile. All these factors together will result in an enhanced and improved mixer that can operate in a wide range of Reynolds numbers regimes.

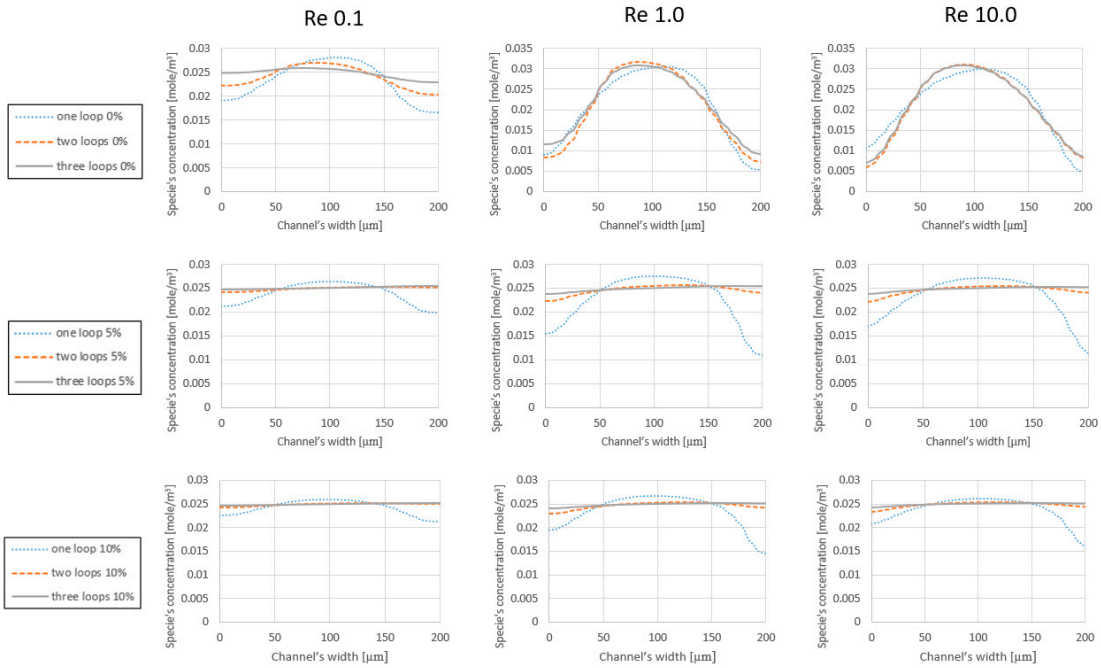

Figure 4. Species concentration at the outlet of the mixer. At each row, mixer types with similar expansion rates are compared with respect to the operating conditions, which are *Re* 0.1, *Re* 1.0 and *Re* 10.0. Regarding the definition of mixing, a straight horizontal line on the level of 0.025 (mol) represents an ideal prepared mixture at the outlet of the device.

4.2. Simulation Results Based on the Expansion Rate

The mixer's performance can be characterized from the expansion rate point of view. According to Figure 5, the one loop class of mixers with 5% and 10% expansion parts prepare the final solute with better quality. Although, regarding the analysis on the effect of the number of loops on the mixer's efficiency, the performance of the different classes decreases in the *Re* 1.0 and *Re* 10.0 regimes. However, the mixer types with 5% and 10% expansion parts show significant improvement toward mixing efficiency. As displayed in all the graphs of Figure 5, the iconic revision in the design of the mixer damps the destructive effect of the inertial term in the mixing and reinforces the diffusion inside the device. Meanwhile, the quality of the one loop mixer without expansion parts is reported as 62% and 66% on *Re* 1.0 and *Re* 10.0 regimes, respectively. The performance of the one loop mixers with 5% and 10% expansion parts for the aforementioned regimes are reported as 85% and 88.8%. Moreover, the comparison between the mixer types in the two loops and three loops classes implies that adopting

expansion and contraction features in the architecture of the mixer improve their efficiency by more than 30%.

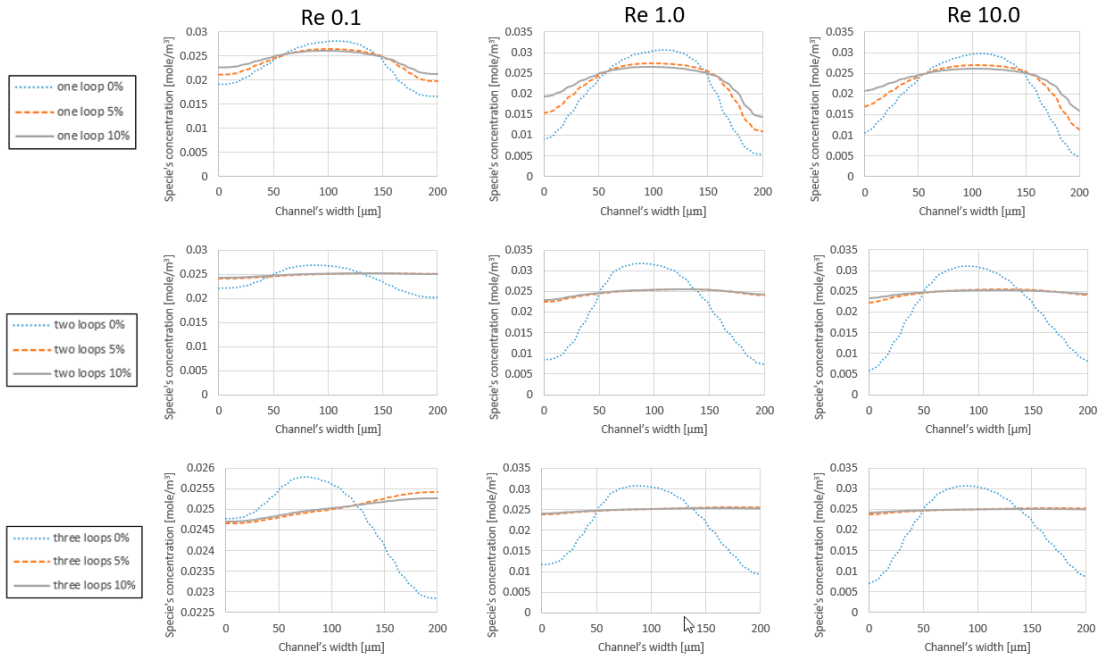

Figure 5. Species concentration along the outlet's cross section. At each row, a specific class of the mixers is represented and at each column the concentration distribution of species at the outlets, regarding the operating conditions.

4.3. Effect of the Expansion on the Diffusion

Adding loops to create as well as to add expansion parts to disturb the flow streams, increases the total mixing length. Both of these factors are key parameters in the Peclet number. Peclet number (Equation (6)) relies heavily on the mixing length and velocity vector; see Equation (6). Figure 6 shows the velocity contours of the one loop mixer without expansion parts and with 10% expansion parts. The distinguishing factor in the efficiency of the above mixers is the velocity profile and the extended mixing length. The combination of these parameters supports the mixing phenomena. The velocity is decreased and the mixing length is increased.

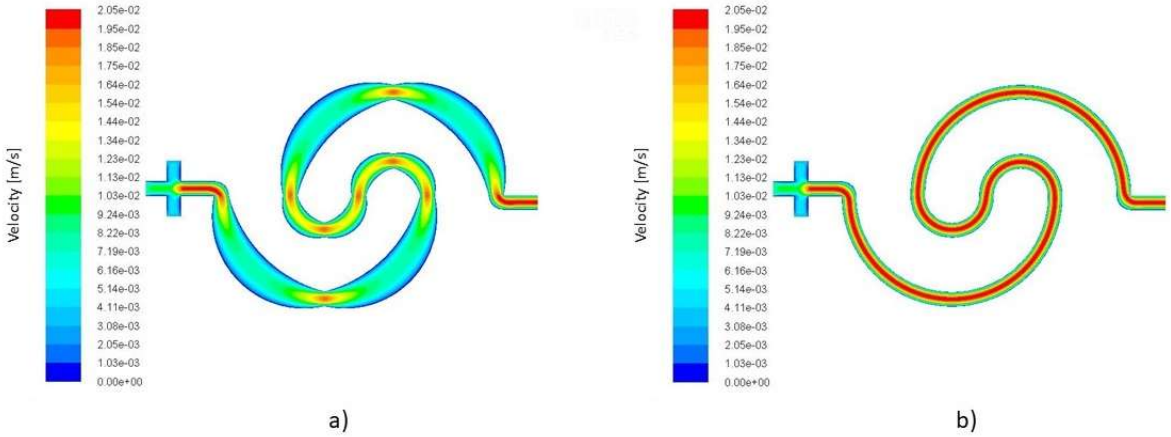

Figure 6. (**a**) Velocity contours of the one loop mixer with 10% expansion and (**b**) the one mixer without expansion parts. The operating condition for both mixers is identical (*Re* 1.0).

The global mixing efficiency at ($Re = 10.0$) is improved toward mixers at ($Re = 1.0$), but this trend changes completely in the mixers with expansion parts. According to the results, as Figure 5 illustrates, adding loops is an effective strategy for prompting the mixing length in the device. Although the device's efficiency reduces at ($Re = 1.0$) compared to other lower and higher initial velocities, the effect of the inertial term and the viscous term being in the same order has been weakened by adopting the expansion and contraction design. Due to the variable width of the channel and the changes in the flow direction at each segment, this geometrical feature causes a disturbance in flow stream and velocity profile continuously.

With respect to the continuity and momentum equations, the velocity at the Venturi points reaches the maximum value, and at the middle of each quarter arc, reduces to the minimum. This fluctuation can be repeated 8 to 16 times, depending on the type of mixer.

On the other hand, the simulation results indicate that the flow lines follow the curvature of the nearest wall, see Figure 6.

This means that the flow should cover more distance in the mixers with expansion parts compared to the models without expansion; see Table 6. Therefore, designs with expansion take advantage of an extended diffusion surface and longer diffusion time. Table 4 and Figure 5 clearly show that adding loops generates better mixing performance at all the mixing ranges.

Table 6. Effect of adding expansion parts on the increase of mixing length in comparison to the mixers without expansion parts.

Mixer Type		ΔL (mm)
One loop	0% expansion	-
	5% expansion	1.71
	10% expansion	1.73
Two loops	0% expansion	-
	5% expansion	2.30
	10% expansion	2.35
Three loops	0% expansion	-
	5% expansion	4.50
	10% expansion	4.63

According to the results (see Table 4, Figures 4 and 5), the quality of the final mixture that is prepared in a one loop micromixer with 5% expansion parts is improved by 33.71% compared to the one loop mixer without expansion parts. These improvements are reported as 88.89% and 94.3% for two loops and three loops mixers with 5% expansion parts, respectively, toward their simple models. Moreover, for devices with 10% expansion parts, these improvements advance further and peak at 52.25%, 93.6% and 96.9% for one loop, two loops and three loops mixers, respectively.

On the other hand, there is another important factor that plays a key role in the practicality and the efficiency of the proposed mixer. A numerous number of mixers are suffering from the considerable amounts of pressure drops in their designs. This feature causes the constant need for an external pump to overcome the pressure drop and keep the flow in a desired Reynolds number range. Besides increasing the chances of structural failure in the device, requiring an external energy source is always a drawback in the Point-of-Care research field. The investigations on the proposed micromixer show that adopting the expansion and contraction parts in the architecture of the design not only improves the mixing quality but reduces the pressure drop in the system. According to Table 7, the pressure loss at each class of the micromixers decreases by adding expansion parts. While the pressure drop for the one loop mixer without expansion parts is reported as 640.85 Pascal, that amount is reported as 442.48 Pa for three loops mixer with 10% expansion part (at $Re = 10.0$). This can be translated into the fact that using the mixers with expansion parts can provide a higher mixing quality with a lower pressure drop.

Table 7. Pressure drop amongst various types of mixers. All the values are in Pascal.

Mixer Type		ΔP at *Re* 0.1	ΔP at *Re* 1.0	ΔP at *Re* 10.0
One loop	0% expansion	6.17	61.97	640.85
	5% expansion	3.26	32.78	352.9
	10% expansion	2.44	24.58	275.18
Two loops	0% expansion	12.6	126.23	1284.21
	5% expansion	4.78	47.96	506.84
	10% expansion	3.24	32.59	359.29
Three loops	0%expansion	21.61	216.3	2181.24
	5% expansion	6.03	63.48	664.153
	10% expansion	4.03	40.48	442.48

4.4. Validating the Numerical Results Based on Real Case Experimental Models

Since the validity of the suggested idea should be verified, a series of experiments are designed and conducted to test the performance of the mixer. The devices from Table 8 (one loop without expansion parts, one loop with 10% expansion parts, three loops without expansion parts and three loops with 10% expansion parts) were fabricated and tested according to the simulated boundary and initial conditions. The constant flow rate of 0.2 mL/h was set for the main channel (water) and 0.1 mL/h was allocated to the side inlets (ink). Since the microscope beams the light from below and the dimensions of the channel are small, determining the borders of the channel is challenging. For a better contrast of the channel walls, the ink is injected from the lateral inlets. This allows a better identification of the channel walls and more accurate analysis of the device. Moreover, since the weakest performance of the micromixer was predicted to be in the *Re* 1.0 regime, the flow rate of the inlets was set to a value that mimics this regime.

Figure 7 shows the image of the one loop mixer without expansion parts, which achieved a 58.28% mixing quality.

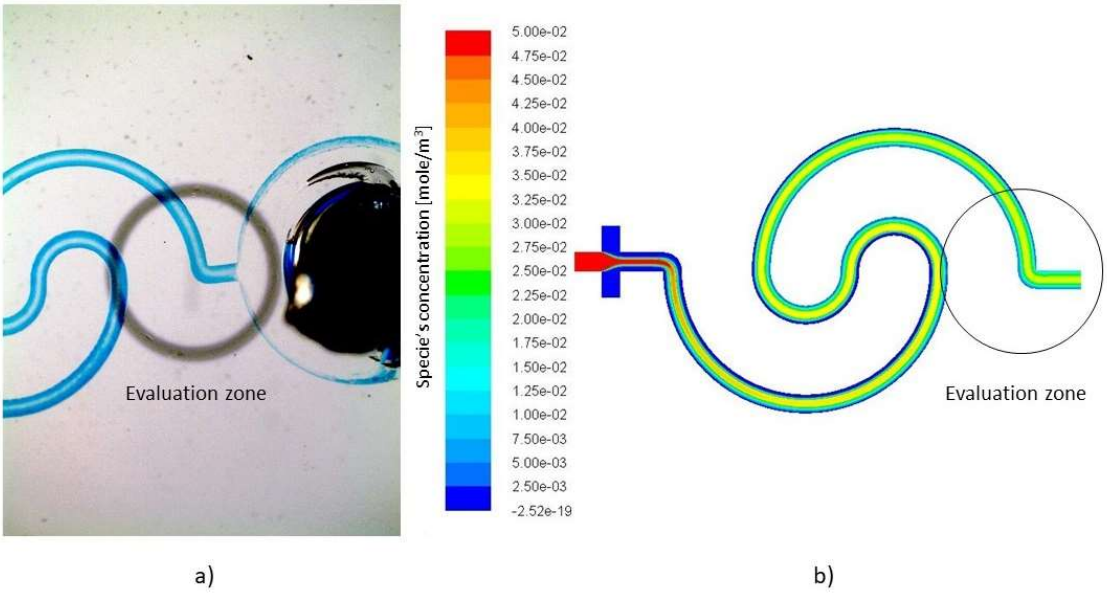

Figure 7. One loop simple spiral mixer: (**a**) Manufactured device species concentration, (**b**) Numerical simulation of the species concentration.

Table 8 summarizes the comparison between simulation and experimental results. Several tests (at least three tests of each device and multiple pictures were captured during each test) provided the average standard deviation of the results, which can be translated into the error margin between the experimental and numerical results. The standard deviation increases in sample devices with larger

geometries. This is due to the fact that to evaluate the mixture, the captured image should contain the inlets and the outlet. Therefore, the magnification, which is suitable for one loop mixer, is not adequate for the three loops class of spiral mixers. All in all, the average reported homogeneity of the fabricated mixers, obtained from pixel to pixel analysis, remains in a maximum 7% difference from the predicted numerical results. Thus, the numerical simulation and experimental results are in good agreement with experimental results. Figure 8 shows a comparison of the species concentration at the outlet (see evaluation zone in Figure 7). In this figure, the mean value of the greyscale at each pixel (analysis of multiple pictures of the evaluation zone) is considered as the result of the experimental evaluation and the error bars for each segment are determined through calculating the standard deviation of the analysis of the pictures in the related pixel. Due to the presence of noise in all the images, the calculations are carried out for the same spot from different pictures.

Table 8. Comparison of numerical and experimental mixer's efficiency at *Re* 1.

Mixer Type		Simulation Results (*Re* 1.0)	Experimental Results
One loop	0% expansion	62%	58.2% ± 8.57%
	10% expansion	85%	78.9% ± 9.13%
Three loops	0% expansion	68%	66.3% ± 13.11%
	10% expansion	98.5%	91.8% ± 14.74%

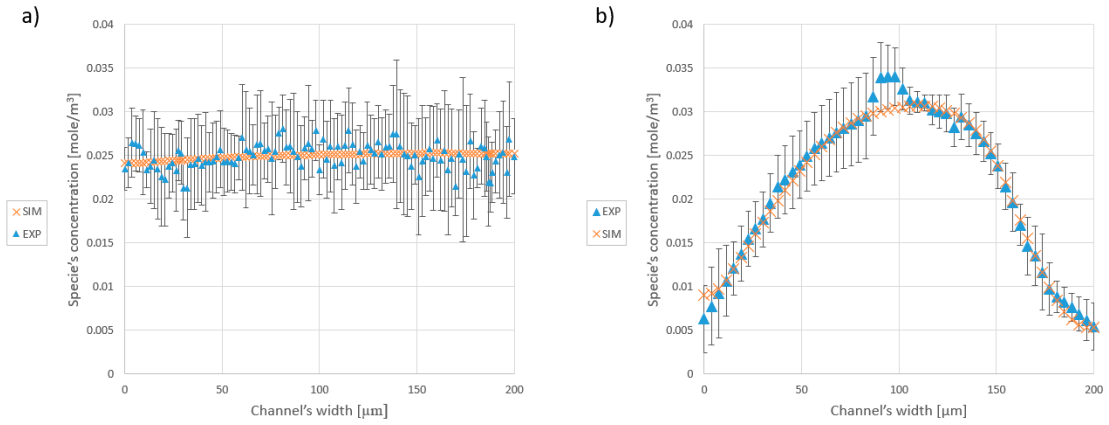

Figure 8. Concentration of the species at the cross-section of the outlet. (**a**) The graph represents the distribution of species at the outlet of the three loops mixer with 10% expansion. (**b**) Species distribution at the outlet of the one loop mixer without the expansion part.

According to the results (Figure 8), not only is the global efficiency of the fabricated models in a reasonable range, but it also proves that the predictions about the concentration distribution, which were made by the software, are correct.

5. Conclusions

The purpose of this study was to design an improved micromixer for low Reynolds regimes useful for LOCs and POCTs devices with high efficiency and low pressure drop. The results of this paper propose a variable radius spiral micromixer as an excellent candidate. This paper studies the performance of the proposed designs in the flow regime range of Reynolds number 0.1 to 10.0. The numerical analysis was validated experimentally at *Re* 0.1.

Therefore, according to the results, the homogeneity of the mixture at the outlet is improved by adding loops to the mixer at low Reynolds numbers. By increasing the Reynolds number to 1.0, the efficiency of the micromixers without modified geometry dramatically drops, while in the variable radius micromixers, the decrease in performance at this flow regime is negligible. Both designs improved their performance at Reynolds 10.

This work demonstrates that regardless of the number of loops, and at every given inlet flow, the performance of the variable radius micromixers improves by increasing the expansion rate. Combining a two loop or three loop micromixer with expansion and contraction parts achieves mixing efficiencies higher than 90%.

In addition, the proposed expansion and contraction parts decrease the pressure drop by more than 60%. This means that employing a two loop or three loop micromixer with expansion parts is a reliable choice in situations where it is required to ease the fabrication, provide a homogenous outcome, use the surface area efficiently and have a low pressure drop.

Author Contributions: This research has been defined and supervised by J.C.-T. All the authors were involved in the conceptualization. Numerical simulations and software configurations were performed by P.M. S.K. took care of Fabrication process. The validation of results was completed by P.M. and S.K. P.M. prepared the original draft and the authors were involved in editing and reviewing the draft. The investigation was performed by P.M. and S.K. Necessary resources were gathered and introduced by J.F.-L. and J.C.-T.

Funding: This research was funded by Spanish Ministry of Economy and Competitivity, grant numbers CTQ2017-84966-C2-1-R and CTQ2016-77936-R (funding also from Federacion Española de Enfermedades Rares "FEDER").

Acknowledgments: The authors are grateful of Universitat Politècnica de Catalunya (UPC) for providing technical support and the required materials.

Conflicts of Interest: The authors declare no conflict of interest.

References

1. Moraes, C.; Mehta, G.; Lesher-Perez, S.C.; Takayama, S. Organs-on-a-Chip: A focus on compartmentalized microdevices. *Ann. Biomed. Eng.* **2012**, *40*, 1211–1227. [CrossRef] [PubMed]
2. Pagliara, S.; Dettmer, S.L.; Keyser, U.F. Channel-facilitated diffusion boosted by particle binding at the channel entrance. *Phys. Rev. Lett.* **2014**, *113*, 1–5. [CrossRef] [PubMed]
3. Bamford, R.A.; Smith, A.; Metz, J.; Glover, G.; Titball, R.W.; Pagliara, S. Investigating the physiology of viable but non-culturable bacteria by microfluidics and time-lapse microscopy. *BMC Biol.* **2017**, *15*, 1–12. [CrossRef] [PubMed]
4. Dittrich, P.S.; Manz, A. Lab-on-a-chip: Microfluidics in drug discovery. *Nat. Rev. Drug Discov.* **2006**, *5*, 210–218. [CrossRef] [PubMed]
5. Mansur, E.A.; Mingxing, Y.E.; Yundong, W.A.; Youyuan, D.A. A State-of-the-Art Review of Mixing in Microfluidic Mixers. *Chin. J. Chem. Eng.* **2008**, *16*, 503–516. [CrossRef]
6. Yager, P.; Domingo, G.J.; Gerdes, J. Point-of-care diagnostics for global health. *Annu. Rev. Biomed. Eng.* **2008**, *10*, 107–144. [CrossRef] [PubMed]
7. Gossett, D.R.; Tse, H.T.K.; Lee, S.A.; Ying, Y.; Lindgren, A.G.; Yang, O.O.; Rao, J.; Clark, A.T.; Di Carlo, D. Hydrodynamic stretching of single cells for large population mechanical phenotyping. *Proc. Natl. Acad. Sci. USA* **2012**, *109*, 7630–7635. [CrossRef] [PubMed]
8. Cama, J.; Chimerel, C.; Pagliara, S.; Javer, A.; Keyser, U.F. A label-free microfluidic assay to quantitatively study antibiotic diffusion through lipid membranes. *Lab Chip* **2014**, *14*, 2303–2308. [CrossRef] [PubMed]
9. Gossett, D.R.; Weaver, W.M.; MacH, A.J.; Hur, S.C.; Tse, H.T.K.; Lee, W.; Amini, H.; Di Carlo, D. Label-free cell separation and sorting in microfluidic systems. *Anal. Bioanal. Chem.* **2010**, *397*, 3249–3267. [CrossRef] [PubMed]
10. Zilionis, R.; Nainys, J.; Veres, A.; Savova, V.; Zemmour, D.; Klein, A.M.; Mazutis, L. Single-cell barcoding and sequencing using droplet microfluidics. *Nat. Protoc.* **2017**, *12*, 44–73. [CrossRef] [PubMed]
11. Jung, W.; Han, J.; Choi, J.W.; Ahn, C.H. Point-of-care testing (POCT) diagnostic systems using microfluidic lab-on-a-chip technologies. *Microelectron. Eng.* **2014**, *132*, 46–57. [CrossRef]
12. Luppa, P.B.; Müller, C.; Schlichtiger, A.; Schlebusch, H. Point-of-care testing (POCT): Current techniques and future perspectives. *TrAC Trends Anal. Chem.* **2011**, *30*, 887–898. [CrossRef]
13. Lee, C.Y.; Wang, W.T.; Liu, C.C.; Fu, L.M. Passive mixers in microfluidic systems: A review. *Chem. Eng. J.* **2016**, *288*, 146–160. [CrossRef]
14. Lee, C.Y.; Fu, L.M. Recent advances and applications of micromixers. *Sens. Actuators B Chem.* **2018**, *259*, 677–702. [CrossRef]

15. Afzal, A.; Kim, K.Y. Optimization of pulsatile flow and geometry of a convergent-divergent micromixer. *Chem. Eng. J.* **2015**, *281*, 134–143. [CrossRef]
16. Silva, J.P.; dos Santos, A.; Semiao, V. Experimental characterization of pulsed Newtonian fluid flows inside T-shaped micromixers with variable inlets widths. *Exp. Therm. Fluid Sci.* **2017**, *89*, 249–258. [CrossRef]
17. Hermann, P.; Timmermann, J.; Hoffmann, M.; Schlüter, M.; Hofmann, C.; Löb, P.; Ziegenbalg, D. Optimization of a split and recombine micromixer by improved exploitation of secondary flows. *Chem. Eng. J.* **2018**, *334*, 1996–2003. [CrossRef]
18. Raza, W.; Hossain, S.; Kim, K.Y. Effective mixing in a short serpentine split-and-recombination micromixer. *Sens. Actuators B Chem.* **2018**, *258*, 381–392. [CrossRef]
19. Chen, X.; Shen, J. Numerical analysis of mixing behaviors of two types of E-shape micromixers. *Int. J. Heat Mass Transf.* **2017**, *106*, 593–600. [CrossRef]
20. Julius, L.A.N.; Jagannadh, V.K.; Michael, I.J.; Srinivasan, R.; Gorthi, S.S. Design and validation of on-chip planar mixer based on advection and viscoelastic effects. *Biochip J.* **2016**, *10*, 16–24. [CrossRef]
21. Alam, A.; Kim, K.Y. Analysis of mixing in a curved microchannel with rectangular grooves. *Chem. Eng. J.* **2012**, *181–182*, 708–716. [CrossRef]
22. Li, T.; Chen, X. Numerical investigation of 3D novel chaotic micromixers with obstacles. *Int. J. Heat Mass Transf.* **2017**, *115*, 278–282. [CrossRef]
23. Chen, X.; Zhao, Z. Numerical investigation on layout optimization of obstacles in a three-dimensional passive micromixer. *Anal. Chim. Acta* **2017**, *964*, 142–149. [CrossRef] [PubMed]
24. Rahman Nezhad, J.; Mirbozorgi, S.A. An immersed boundary-lattice Boltzmann method to simulate chaotic micromixers with baffles. *Comput. Fluids* **2018**, *167*, 206–214. [CrossRef]
25. Xia, G.D.; Li, Y.F.; Wang, J.; Zhai, Y.L. Numerical and experimental analyses of planar micromixer with gaps and baffles based on field synergy principle. *Int. Commun. Heat Mass Transf.* **2016**, *71*, 188–196. [CrossRef]
26. Hossain, S.; Ansari, M.A.; Kim, K.Y. Evaluation of the mixing performance of three passive micromixers. *Chem. Eng. J.* **2009**, *150*, 492–501. [CrossRef]
27. Khosravi Parsa, M.; Hormozi, F.; Jafari, D. Mixing enhancement in a passive micromixer with convergent-divergent sinusoidal microchannels and different ratio of amplitude to wave length. *Comput. Fluids* **2014**, *105*, 82–90. [CrossRef]
28. Vatankhah, P.; Shamloo, A. Parametric study on mixing process in an in-plane spiral micromixer utilizing chaotic advection. *Anal. Chim. Acta* **2018**, *1022*, 96–105. [CrossRef] [PubMed]
29. Cosentino, A.; Madadi, H.; Vergara, P.; Vecchione, R.; Causa, F.; Netti, P.A. An efficient planar accordion-shaped micromixer: From biochemical mixing to biological application. *Sci. Rep.* **2015**, *5*, 1–10. [CrossRef] [PubMed]
30. Syms, R. Rapid evaporation-driven chemical pre-concentration and separation on paper. *Biomicrofluidics* **2017**, *11*, 1–17. [CrossRef] [PubMed]
31. Xia, Y.; Whitesides, G.M. Whitesides Soft lithography. *Annu. Rev. Mater. Sci.* **1998**, *28*, 153–184. [CrossRef]
32. Crocker, J.C.; Grier, D.G. Methods of digital video microscopy for colloidal studies. *J. Colloid Interface Sci.* **1996**, *179*, 298–310. [CrossRef]
33. Dettmer, S.L.; Keyser, U.F.; Pagliara, S. Local characterization of hindered Brownian motion by using digital video microscopy and 3D particle tracking. *Rev. Sci. Instrum.* **2014**, *85*. [CrossRef] [PubMed]

Food Chemistry 344 (2021) 128583

Contents lists available at ScienceDirect

Food Chemistry

journal homepage: www.elsevier.com/locate/foodchem

Portable 3D-printed sensor to measure ionic strength and pH in buffered and non-buffered solutions

Pouya Mehrdel *, Shadi Karimi, Josep Farré-LLadós, Jasmina Casals-Terré

Mechanical Engineering Department – Microtech Lab, Universitat Politecnica de Catalunya, C/Colom 7-11, CP 08222, Terrassa, Barcelona, Spain

ARTICLE INFO

Keywords:
Diffusion
3D printed sensor
Ionic strength
Buffer solutions
Non-buffer solutions
pH measurement
Wine
Colorimetric detection

ABSTRACT

A miniaturized 3D-printed device has been designed, manufactured and validated to perform as a low-cost sensor for compositional analysis of buffered and non-buffered solutions in industrial or remote areas.

The proposed sensor takes advantage of the transport phenomenon and colorimetric measurements. The novel design can simultaneously detect the ionic strength of the solution by measuring the diffusion width of the ions and the pH by image analysis of the pH indicator color change. The results showed that it can detect pH variations of 0.25 and ionic measure difference of 0.1 M in non-buffer solutions. In addition, the design showed its adaptability to be used as a self-referencing sensor.

The 3D-printed sensor presented here is not only successful in the evaluation of some important chemical characteristics but also brings flexibility, cost-effectiveness, swiftness and user-friendliness.

1. Introduction

Historically, the agri-food industry, the processing of agricultural raw materials or their preprocessing for future use in food preparation, has been the sustaining industry for humanity. Among various proceedings, grape processing is an ancient activity. Viticulture has been an old, but thriving tradition in Spain and has an appreciable economic impact. Wine's importance for Spanish culture, economy, and industry is undeniable. As far as, January 2020, Spain was the third producer of wine worldwide and hosted about 13% of worldwide vineyards. Spanish wine-making tradition has followed strict standards to always maintain its unique wine quality and taste. Sustaining these qualities would not have been possible without an important effort of innovation.

Must extracted from the grapes is mostly composed of tartaric, malic and citric acids (Prenesti et al., 2004, 2012), which can slightly change during the ripening and depends on the species of the grapes as well. Besides, the climate of the vineyard can influence the composition of the must too. During the ripening and fermentation process, different acids are formed and the identification of such characteristics is extremely relevant for an enologist (Angelkov & Martinovska, 2018; Sanz, 2014). Enologists not only monitor the pH, but also track the titratable acidity due to the necessity of controlling the wine stability, in accordance with the regulations and producing the unique features of each wine.

Disclosing the precise composition of unknown solutions or finding the concentration of a specific substance has always been an interesting topic for the researchers and industry, especially for the industries that are attending to humans' health and sustenance. Numerous physical and chemical methods are used for quantitation of solutions (Fukuhara, 2020). The most common laboratory techniques include electrophoresis (Fuguet et al., 2009), titration (Honorato et al., 1999) or enzyme-linked immunosorbent assay (ELISA) (Grigore et al., 2018). The standardization of the production of agri-food products has introduced analytical complex technologies. The most common procedures utilized to study the composition and the chemical structure of the solutions are High-Performance Liquid Chromatography (HPLC) (Boukhobza & Crans, 2020; Sahu et al., 2018), Fourier-Transform InfraRed (FTIR) (Versari et al., 2014) and Nuclear Magnetic Resonance(NMR) spectroscopy (Sobolev et al., 2019). However, all these analytical techniques have large turnaround times and require trained staff and equipment.

Recently, the possibility to miniaturize these processes using microelectronics and microfabrication, has enabled the use of multiple gas and odor sensors in the so-called e-nose biomimetic approach to obtain special characteristics of each desired wine, but not the exact composition (Matthews et al., 1990; Preedy, 2016; Rodríguez-Méndez et al., 2016; Wilson, 2013). This is an important step towards miniaturization and it definitely reduces the required time for the analysis. However, e-

* Corresponding author.
E-mail addresses: pouya.mehrdel@upc.edu (P. Mehrdel), shadi.karimi@upc.edu (S. Karimi), josep.farre.llados@upc.edu (J. Farré-LLadós), jasmina.casals@upc.edu (J. Casals-Terré).

https://doi.org/10.1016/j.foodchem.2020.128583
Received 23 June 2020; Received in revised form 1 October 2020; Accepted 4 November 2020
Available online 18 November 2020

noses require functionalized surfaces to detect compounds and they are normally single-use or have a short life-cycle. E-noses are consisted of a series of sensors to detect different gases or components of wines, which provides a large array of data but on the other hand, increases the complexity.

Two of the essential characteristics of wines in the winemaking process are pH and ionic strength (acid concentration). Therefore, a portable device that provides both in short time and near the product is of huge interest. There is a reasonable amount of approaches to measure pH with short turnaround time that are miniaturized i.e. electrochemical or optical approaches with novel materials as coatings or paper indicators (Ghoneim et al., 2019; Rodríguez-Méndez et al., 2016), which have a broad range of price and accuracy. However, there are few methods to measure the ionic strength of solutions, either buffered or non-buffered ones, in a cost-effective and fast approach.

Microfluidics uses minimum amounts of fluids, which provides specific characteristics to the ionic transport in the microfluidic flow. The surface to volume ratio is important at micron-scale and we can take advantage of laminar flow or fast diffusion of molecules at this scale. Previous researchers have started to take advantage of such possibilities, while some others have regulated the usage of microfluidics in chemistry (Persat et al., 2009). Dzebic et al. proposed a microfluidic design that was able to determine the unknown concentration of an analyte (titration) on a chip, using microliters instead of milliliters (Dzebic et al., 2017). Other researchers have focused on the use of microfluidics to take advantage of the fast diffusion of protons. For instance, there are reports that study the stomach mucus barrier function (Li et al., 2012) or determine the pK_a through capillary electrophoresis (Cabot et al., 2015). Specially, Yager research group pioneered the use of *T*-sensors for pH determination (Osborn et al., 2011).

In this paper, we present for the first time a microfluidic 3D-printed design capable of measuring ionic-strength and pH near the product, by taking advantage of fast diffusion and mixing in the design. The design has been validated in buffer solutions (by using HEPES) and non-buffered solutions (white wine). The accuracy, fast responsiveness, minimum analyte requirement and user-friendliness are the noteworthy characteristics of the proposed device and makes it an ideal choice for laboratory and industrial approaches.

2. Methodology

2.1. Proposed geometry

*Fig. 1 presents a schematic implementation of the proposed device to evaluate the pH and ionic strength of a non-buffered solution such as wine in a remote environment such as a winery. The proposed geometry

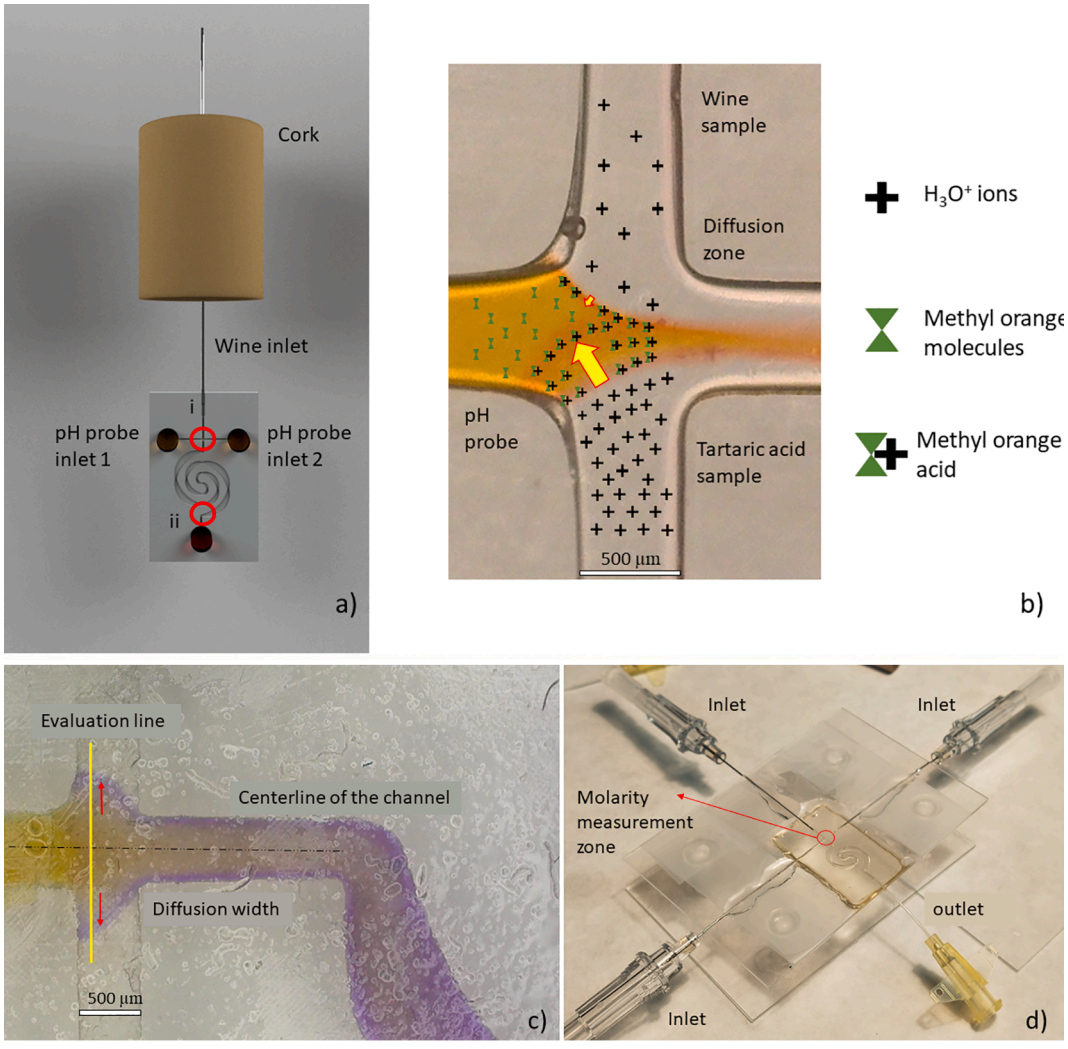

Fig. 1. a) Vision of sensor implementation for wine evaluation (pH and ionic strength). i) Ionic strength evaluation zone and ii) pH evaluation zone. b) The diffusion phenomenon is illustrated here. Wine sample (pH 3.52) is injected through the upper inlet and the 1.0 M tartaric acid solution is injected through the bottom inlet. The flowrate of the both lateral inlets is identical and equal to 2.1 ml/h. Yellow arrows represent the diffusion flux in the reaction zone. c) Picture of the diffusion phenomena at the intersection of the inlets. Evaluation line: where the buffer diffusion is measured over. d) Picture of the 3D printed manufactured device.

takes advantage of laminar flow established at the microscale. Hence, the diffusion is enhanced within the channel and enables the establishment of the relation between the diffusion and the ionic strength of the species in both buffered and non-buffered solutions.

Diffusion is best traceable when the solutions are first met. Therefore, the diffusion is evaluated at the intersection of the inlets, see Fig. 1-a point *i*. A diffusion zone will be created because of the encounter and the analysis of the diffusion zone can reveal the ionic strength of the solutions (Fig. 1 – c). On the other hand, the pH analysis is performed at the outlet of the device, at this point the pH indicator and the solutions are uniformly mixed, see Fig. 1-a point *ii*. However, for the experiments that are susceptible to crystallization, the pH can be evaluated right after the intersection to avoid the interference of the crystals on the image processing.

2.2. 3D printing fabrication

The manufacturing process uses Digital Light Projection Technique (DLP) (Gong et al., 2015). Briefly, a 3D model of the geometry, previously designed in our research group (Mehrdel et al., 2018), is modeled using @Solidworks software and exported to *.stl format to be introduced to the @MiiCraft Plus printer. The built-in @MiiSlicer software of the 3D printer later slices up the 3D model. After adjusting the settings, such as UV light exposure time (4.2 s) and the rest time between exposures (at least 1.8 s), the model is printed. The layers of photosensitive resin are successively exposed to UV light to define the pattern. In this process, every layer is hardened where exposed and deposited on the top of the previously printed layer.

Once the channel structure is printed, the process is halted and the excess resin is removed via gentle air blow in order to guarantee that no resin has remained inside the channel. The channel can be either covered by further printing on the top or by attaching it to a glass slide. In any case, a UV light exposure of 1800 s is needed for a perfect cure. Finally, the connectors are installed and fixed in the inlets and outlet by a photocurable resin @NOA 63. Please see Fig. 1 – d.

The width of the channel in the narrowest section is set to 500 μm. The channel's height is 500 μm and as mentioned before, it is sealed either by printing a top layer with a thickness of 300 μm or attaching a microscope glass slide to facilitate the analysis of the images. The material used in the printing procedure is @MiiCraft BV-007 (Clear) – MiiCraft.

2.3. Materials and the experimental setup

2.3.1. Non-buffered solutions

Conventional white table wine was used. NaOH (sodium hydroxide) was purchased from @PanReac AppliChem and it was used to prepare two different concentrations of NaOH solution (1 M and 0.1 M). The pH of wine was adjusted to pH 3.52 by adding 3.5 ml NaOH [0.1 M] to 30 ml of wine and 0.35 ml of NaOH [1 M] to 40 ml of wine to achieve pH 3.74. All pH measurements were performed at room temperature- T^a (20 °C).

Tartaric acid (2,3-Dihydroxybutanedioic acid) was purchased from @Merck Schuchardt OHG. Three tartaric acid concentration were prepared (0.1 M, 0.5 M and 1 M).

Methyl orange (Sodium 4-{[4-(dimethylamino)phenyl]diazenyl} benzene-1-sulfonate) was selected as the pH indicator. Methyl orange has a transition range of pH 3.0 up to pH 4.0 (Ethier & Simmons, 2007) being red at pH 3.0 or inferior values and remaining yellow at pH 4.0 or higher. Therefore, it is suitable for the expected pH values in white wines.

2.3.2. Buffered solutions

4-(2-HydroxyEthyl)-1-pi-PerazineEthaneSulfonic acid, HEPES was purchased from @Sigma Aldrich was selected as an example of buffer due to its wide used in the biomedical and biomechanical studies (Chen et al., 2019).

Bromocresol purple (5′,5″-diBromo-o-CresolsulfoPhthalein, BCP) was acquired from @sigma Aldrich, and used as the pH indicator for the buffer solutions. This indicator has a transition range from pH 5.2 to pH 6.8 (Kim et al., 2012), suitable for HEPES solutions.

Three different concentrations of HEPES buffer were prepared (0.1 M, 0.5 M, and 1 M). The pH of the solution was adjusted by adding small volumes of 1 M NaOH according to the protocol provided by the HEPES manufacturer and pH was validated in the laboratory at room temperature.

2.4. Diffusion phenomenon

Diffusion is considered as the most influential transport factor of species in laminar flows. This phenomenon, which is expressed in Eq.1, is described by Fick's law (Ethier & Simmons, 2007).

$$J = -D\frac{d\varphi}{dx} \tag{1}$$

where J denotes the diffusion flux and D represents the diffusion coefficient of species. In the above equation, φ shows the concentration of the desired species at a given point.

Focusing on equation (1), this study aims at monitoring the concentration of the solutions based on their diffusion. The main difference among the solutions is their ionic concentration or in other words the number of H_3O^+ (Hydronium) ions. Although the diffusion can be modified by other properties, it should be noticed that all the analytes are at the same temperature and the differences in the dynamic viscosities of the solutions are negligible compared to their ionic concentration differences. According to equation (1), the species (in this case hydronium) diffuse from the rich region to the poor region, see *Fig. 1 – b. When hydronium ions diffuse into the pH indicator region, the pH indicator captures the hydronium, transforms and changes the color. The amount of advance of the species from one region to the other is directly proportional to the concentration of species, and the color itself can be correlated to the pH.

2.5. Evaluation techniques and instruments

Tartaric acid is one of the key components of white wine and has a determining role in the wine's savior and odor (Oliveira et al., 2010). Therefore, it can be considered as a legitimate candidate to compare the behavior of wine to it. For the non-buffered solutions, the diffusion width of tartaric acid was compared to the diffusion width of the wine sample with unknown concentration. This comparison was later used as the foundation of ionic strength measurement.

Two syringe pumps were used to settle the flow rates (Graseby 3200-@Smiths, Watford, Hertfordshire(UK) and kdScientific 410-CE-@kdScientific, Holliston (US)). Depending on the evaluation, different flow rates were used i.e. methyl orange in the middle inlet at a flowrate of 0.7 ml/h and wine in lateral inlets at different flow rates (2.1–1.7 and 1.4 ml/h) to evaluate the most suitable flow rate to achieve accurate results. Nevertheless, the assay showed the flexibility of altering the arrangement of the inlets, for instance by injecting the pH indicator from the lateral channels, please see Fig. 2 – a and c. Choosing the proper arrangement of the inlets depends on the feature or substance that is under evaluation. For pH, it is recommended to inject the pH indicator from the lateral inlets. However, measuring the ionic strength requires two symmetrical inlets for the tartaric acid (or calibrated sample) and the wine sample and leaves only one inlet for the pH indicator.

Fig. 2 – a and c, show the diffusion width when the pH indicator and the solution (or solutions) are first met at the intersection of the inlets. The diffusion width depends on the concentration of hydronium ions and their interaction with the pH indicator's molecules. The higher the concentration of hydronium ions, the wider the diffusion width and in other words the stronger ionic strength. Therefore, the measurement of

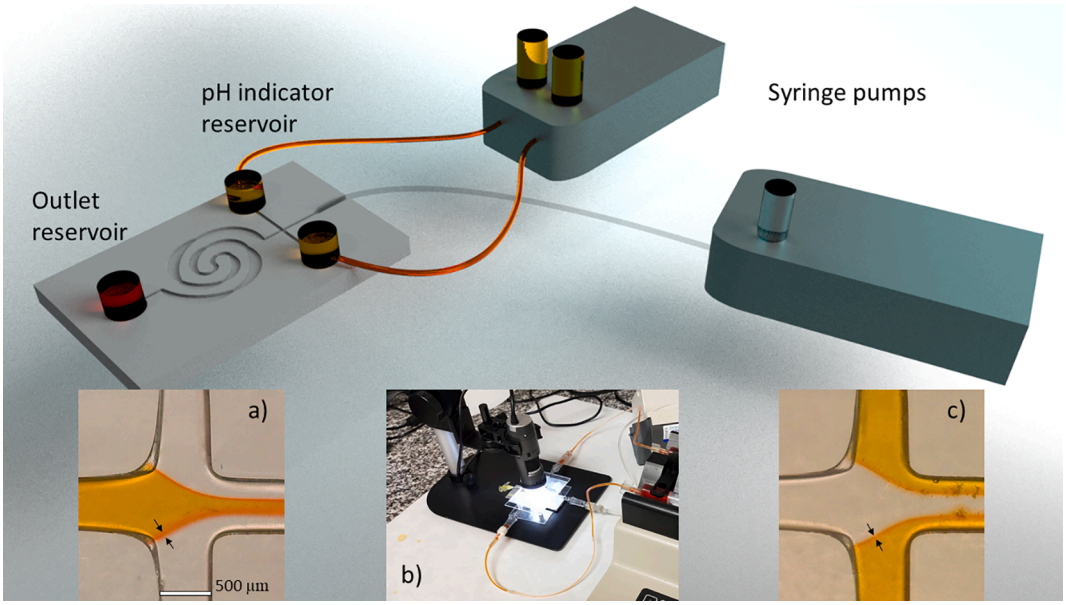

Fig. 2. Schematics of the experimental setup: pH indicator injected through both lateral channels. Dimensions are not to scale. a) 0.5 M tartaric acid solution injected from the bottom inlet and the wine sample at pH 3.52 injected through the upper inlet. The diffusion width is pointed by the black arrows. This arrangement is ideal for comparing the diffusion width of different solutions. b) Real picture of the experimental setup. c) pH 3.74 wine sample is injected through the middle inlet. An ideal arrangement for pH measurement, even in the presence of precipitated salts.

the molarity/concentration/ionic strength is carried out at the intersection to avoid possible interaction with the salt precipitates in non-buffered solutions. (See Fig. 2 – c).

The diffusion width is measured and correlated to pH and ionic strength, by taking advantage of the RGB profile of the pictures captured using a Dino-Lite MS325B and analyzed by Image-J software.

For the buffered solutions, measuring pH is as important as measuring the ionic strength. Determination of the HEPES pH level depends on the homogeneity of the indicator and solution mixture, therefore the pH measurement is done at the outlet of the mixer, see Fig. 1 – a) ii.

In all the experimental evaluations and especially in optical measurements, there will always be errors introduced by the light reflections due to the poor surface finishing of the device or light refraction because of the different layers of material. To minimize the impact of these errors during the data analysis, the Grubbs' test was applied to detect outliers at a 0.05 significance level. Therefore, experimental errors were calculated as mean and standard deviation in agreement with the respective standards.

3. Results and discussion

3.1. Evaluating the characteristics of the Non-buffered solutions

Non-buffered solutions such as wine are a mixture of different substances where the ionic concentration and pH are essential to define its taste, state and chemical characterization in general.

3.1.1. Optimization of flow rate ratio between samples and indicators

In this work, the transport of species is a balance between the convective and the diffusive term. The convective transport, caused by the syringe pump, is responsible for moving the bulk of species along the channel. Whereas, the diffusive term tries to uniform the concentration of species across the channel. Hence, a proper balance between the convective and diffusive term can enhance the accuracy of the sensor. Therefore, the effect of the flow rate ratio between the middle inlet and the lateral inlets is analyzed. To achieve this purpose, pH indicator (methyl orange) was injected through the lateral inlets at 0.7 ml/h, kept constant and the wine samples were injected through the middle inlet at different flow rates: 1.4, 1.7 and 2.1 ml/h.

Investigation showed that (please see supplementary materials Fig. 1), as expected, when the flow rate ratio between lateral inlet/middle inlet was increased the diffusion effect decreased. When the ratio was increased, not only the hydronium ions had less time to diffuse across the channel width, but they also needed to overcome a stronger bulk inertia in the direction of the flow. In other words, the increased flow rate occupied more space in the center of the channel and pushed the pH indicator more to the sides. Consequently, as the inertial term grew the diffusive term shrank.

It should be mention that, although the blue intensity profile is ideal for analyzing the bright and dark regions, the experiments showed that the blue intensity profile is not the best choice for analyzing the reactions or analytes with warm colors. Therefore, the green intensity profile was used in these cases, in order to cover both sides of the color spectrum.

Furthermore, the results indicated that increasing the flowrate of the wine to 2.1 ml/h reduces the chance of precipitation in the measurement zone, but at the same time drastically influences the reaction zones and pushes them to the walls of the channel. On the other hand, setting the flowrate to 1.4 ml/h provided the opportunity of capturing images of wider diffusion zones and improved the accuracy and resolution of the measurements, but at the same time increased the chances of precipitation.

Choosing the optimum flowrate depends on the aim of the study and the precipitation rate during the assay. In this study for ionic strength measurements, the lateral inlets to middle inlet flowrate ratio was set to 3.

In the case of pH measurement, the analysis was performed on the intensity of the reaction between the pH indicator and the solution (the color change of the pH probe). Fig. 3 – a shows that, even though the flow ratio between inlets was varying in the assay, the intensity of the mean green value remained constant. Therefore, it was concluded that the optimum flow rate ratio for ionic strength evaluation is also compatible with an accurate measurement of the pH.

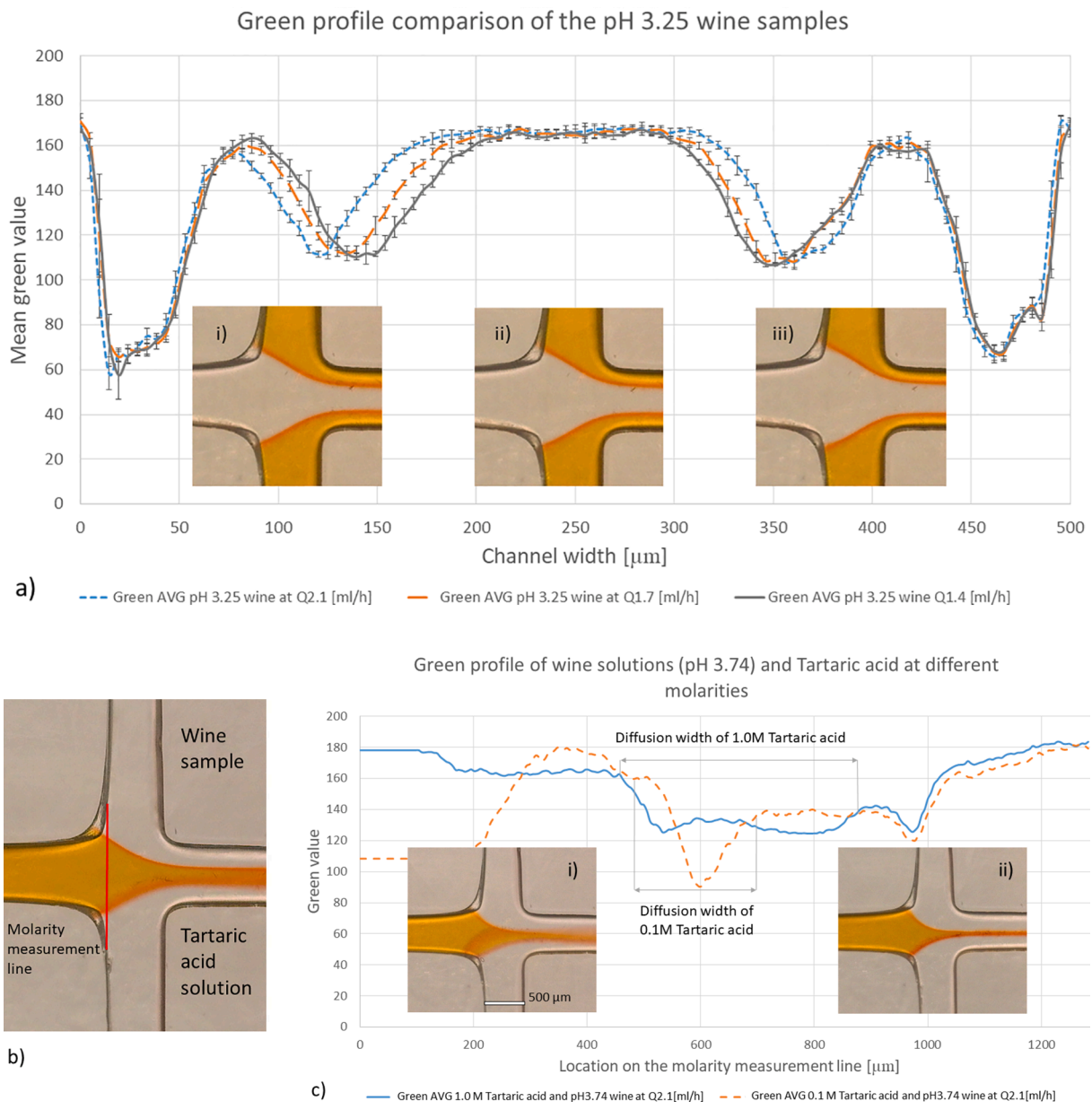

Fig. 3. a) Mean green intensity profile of the same wine sample (pH 3.25) at different flowrates. Flowrate a) 1.4 ml/h, b) 1.7 ml/h and c) 2.1 ml/h. b) Picture of the molarity measurement line. c) Colorimetric green intensity value analysis of the wine sample (pH 3.74) and the tartaric acid solutions. The difference between the diffusion width of tartaric acid and different solutions are illustrated. i) Wine sample (pH 3.25) and 1.0 M tartaric acid and ii) wine sample (pH 3.25) and 0.1 M tartaric acid.

3.1.2. Non-buffered solutions ionic strength measurements

For the non-buffered solutions, the pH indicator (Methyl orange) is injected through the middle inlet at 0.7 ml/h. The upper inlet is dedicated to the wine solution (pH 3.25, pH 3.52 and pH 3.74) and it is injected at 2.1 ml/h. Three different concentrations of tartaric acid (0.1 M, 0.5 M and 1.0 M) are injected through the bottom inlet at the same flowrate as the wine sample. Please see Fig. 2 – a and Fig. 3 – b.

Initial results showed that the setup is vulnerable to crystallization inside the channel; therefore, the measurements were performed at the intersection after the stabilization of the flow.

According to the results, the evaluation of the diffusion width using the green intensity profile of the experimental assays (see Fig. 3 – c) is correlated to the concentration of tartaric acid. Furthermore, a linear relationship between diffusion width and ionic strength/molarity of tartaric acid was observed during the assays (Please see supplementary materials Fig. 2.).

Due to the fact that the ionic concentration of healthy wine is mostly due to tartaric acid (Prenesti et al., 2004, 2012), tartaric acid was used as the calibration standard for the wine samples.

The three different wine samples, which their pH had been adjusted by adding NaOH solution, were tested following the abovementioned procedure. The addition of NaOH (strong base) decreased the total amount of free H_3O^+ ions. The results, see Table 1 in the supplementary materials, showed that increasing the pH eventuated in a decrease in the diffusion width.

The reported results can be justified by the analytical chemistry and acid-base equilibria. Wines are a mixture of different acids and there is an abundance of hydronium in them. When a limited amount of base is added to the acid solution, the hydronium ions (H_3O^+) attach to the hydroxide ions (OH^-) and form a water molecule. The conjugate base and the conjugate acids present in the medium also react with each other and form a salt. The described process is also illustrated in Eq.2 to Eq.4.

$$HA \xrightarrow{H_2O} H_3O^+ + A^- \quad (2)$$

$$BOH \xrightarrow{H_2O} OH^- + B^+ \quad (3)$$

$$H_3O^+ + A^- + OH^- + B^+ \rightarrow H_2O + BA \quad (4)$$

where HA and BOH are arbitrary acid and base. While A^- and B^+ represent the conjugated base and conjugated acid, respectively.

Therefore, by adding the NaOH to the wine, not only some of the hydronium ions are removed from the solution, but they are also used to form water molecules. Therefore, the ratio of hydrogen ions to the total volume of the sample decreases. This phenomenon decreases the hydronium concentration in wine and it consequently reduces the ionic strength of the solution.

Tartaric acid solutions only vary in concentration (and hence the ionic strength). Fig. 3 – c (i) and (ii) clearly show a different diffusion width for 0.1 M and 1 M solutions. The dashed line, see Fig. 3 – c can be used as the calibration plot for the evaluation of wine's ionic strength, since it shows the reaction width of the tartaric acid (0.1 M). The diffusion width of the three different concentrations of tartaric acid samples is summarized in supplementary materials (please see Table 2). Notice that when the ionic strength of tartaric acid increases the measured width increases as well.

The calibration plot can be used to estimate the ionic strength adding the value of diffusion width on the plot, (see supplementary materials Fig. 2 - orange dots). The wine's (pH 3.25) diffusion width is in the same range as the results of 0.1 M tartaric acid and it can be concluded that the concentration of ions in both solutions are in the similar order. The rest of the samples (different pH of wine), according to equation (4), had narrower diffusion width and therefore less ionic concentration (see supplementary materials Fig. 2).

During the winemaking process, the same approach can be used with a benchmark wine to monitor the fermentation or the characteristics (overall molarity (ionic strength) and pH), to make sure that the preparing wine qualities are equivalent to the benchmark wine's standard.

3.1.3. Non-buffered solutions pH measurements

As mentioned earlier, pH variations can reveal whether if a product is still safe to consume or not. In the case of wines, fermentation continuously modifies the pH and the amount of alcohol in the solution. This value can be considered as a borderline between a consumable wine or vinegar.

For the pH measurement, the same sensor setup arrangement was respected except for the dedication of the inlets. Where the pH indicator reagent was injected from the lateral inlets and the wine sample was injected through the middle inlet. The flowrate of the pH indicator was constant and set to 0.7 ml/h. Meanwhile, the wine samples were injected at 1.4 ml/h.

Analysis shows a decrease in the mean green color value in wine samples as the pH increases (plese refer to the Table 3 in the supplementary materials). The value is achieved by comparing the minimum point in the reaction region to the maximum points surrounding the reaction region. Please see the dashed line and points i, ii and iii in Fig. 4. Whereas, the arrows i, ii and iii represent the differences in wine samples with pH values of 3.25, 3.52 and 3.74, respectively.

However, as mentioned in subsection 3.1.1, the best contrast (for pH evaluation) was achieved when the flowrate ratio was set to 2. Nonetheless, if the flow rate ratio had to be increased due to the presence of precipitates, the method was responsive to pH variations even at the highest flow rate ratio (2.1/0.7 ml/h). Since the methyl orange pH indicator produces a red color for pH 3 or lower and yellow color for pH 4 or higher, Fig. 4 - a-*b*-c show the color evolution from red at pH 3.25 to light orange at pH 3.74. Hence, an increase in the pH turns in a higher mean green intensity value (or higher nadir, see point (iii) in Fig. 4 and a decrease in the pH turns in a lower mean green intensity value (or a deeper nadir, see point (i) Fig. 4). Further studies, please see Appendix A, were implemented to correlate the surface area of different wine samples to the pH.

3.2. Buffered-solutions analysis

3.2.1. Buffer ionic strength analysis

Nine different HEPES solutions with known pH and molarities were prepared. The lateral channels were dedicated to HEPES and the middle inlet to the pH indicator to evaluate the diffusion width between BCP and the different buffer molarities, see Fig. 5. Fig. 5 – a shows the

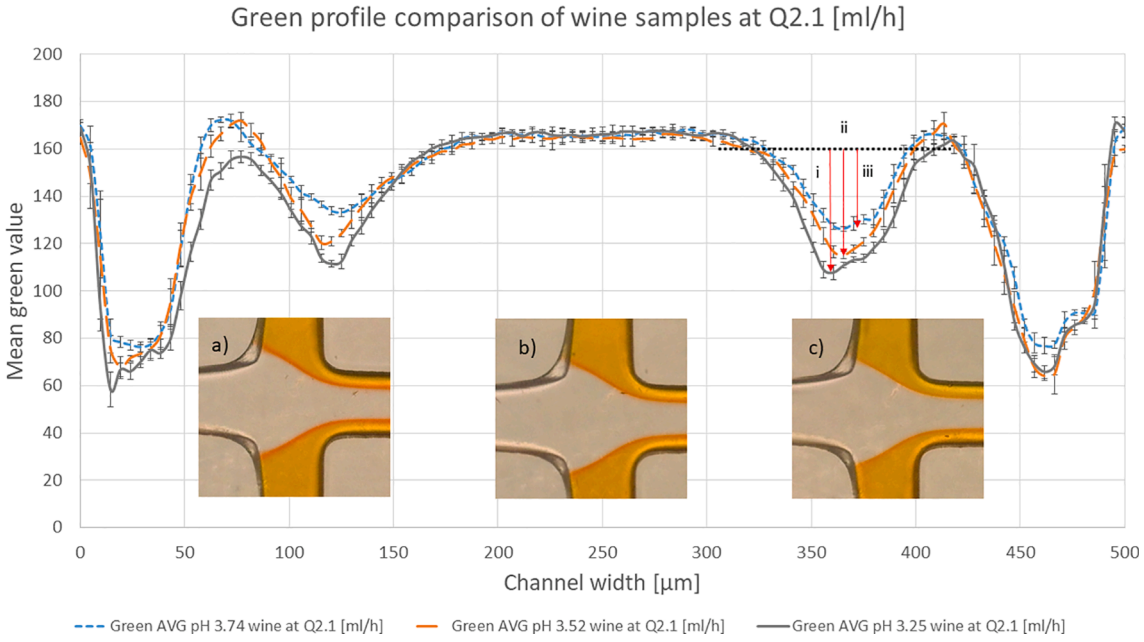

Fig. 4. Mean green intensity value of different pH wine solutions (flow rate ratio between the inlets of 2). The drop in the reaction region i, ii and iii, correlate to the change of intensity due to pH 3.25, pH 3.52 and 3.74, respectively. The reaction between the mentioned samples and the pH identifier is illustrated in Images a), b) and c).

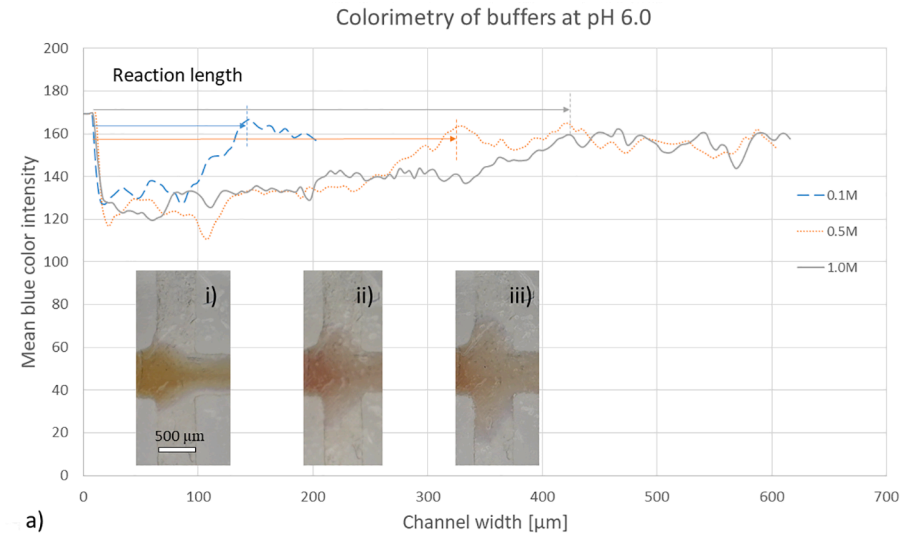

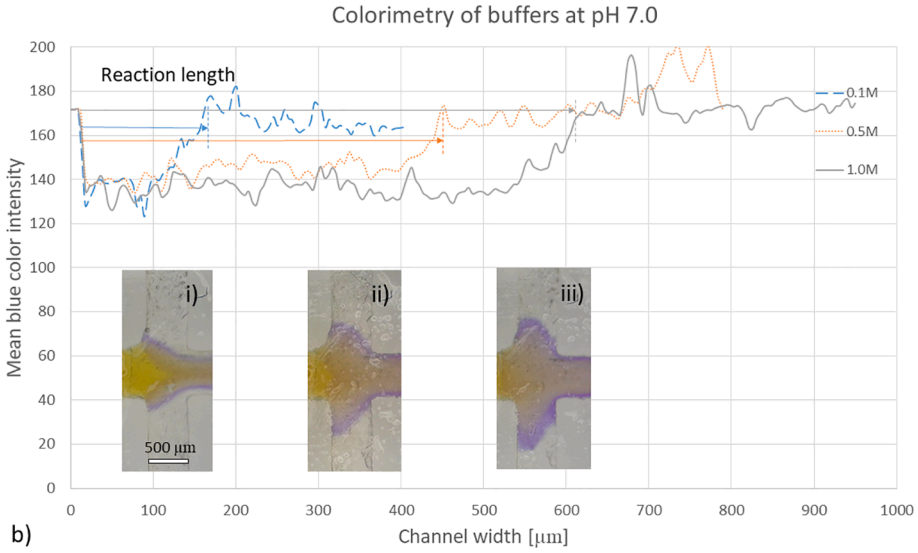

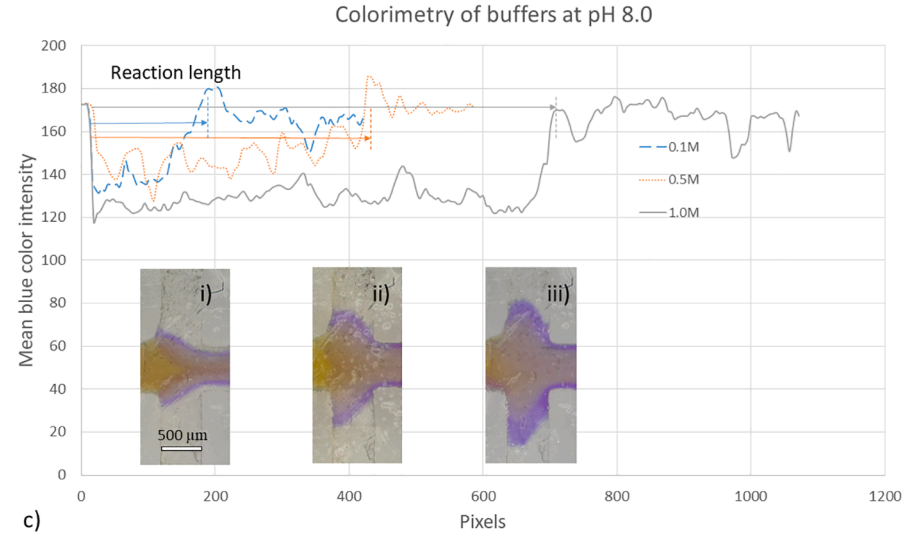

Fig. 5. a) Colorimetric analysis of the diffusion of a HEPES buffer solution of pH 6.0. Pictures (i), (ii) and (iii) depict the diffusion width of three different solutions of 0.1, 0.5 and 1.0 M of HEPES molarities, respectively. b) Colorimetric analysis of the diffusion of a HEPES buffer solution (pH 7.0). Pictures (i), (ii) and (iii) depict the diffusion width of three different HEPES solutions: 0.1, 0.5 and 1.0 M. The color change at this pH level is detectable to naked eye. c) Colorimetric analysis of the diffusion of HEPES buffer solutions (pH 8.0). This level is beyond BCP's capacity to demonstrate the alkalinity of buffers and the color change and diffusion widths are at their maximum. Reactions of BCP and buffer solutions with 0.1, 0.5 and 1.0 M of HEPES are shown in pictures (i), (ii) and (iii), respectively.

colorimetric analysis of buffer solutions at pH 6.0 with different HEPES molarity. The evaluation line was drawn from the intersection of the main channel and the lateral channel up deep into the lateral channel, until no reaction was visible (please check Fig. 1 – c)). The results showed that at the same pH, the interaction length (in other words the diffusion width) was highly dependent on the HEPES molarity. While the changes in mean blue intensity value were negligible, the reaction advanced further into the lateral channel as the HEPES molarity was increasing. According to results (please see Table 4 in the supplementary materials), the mean diffusion width of the buffer solution (pH 6.0, HEPES 0.1 M) was reported to be 172.56 μm, whereas the same measurement marked 355.42 and 471.43 μm for the analytes with 0.5 M and

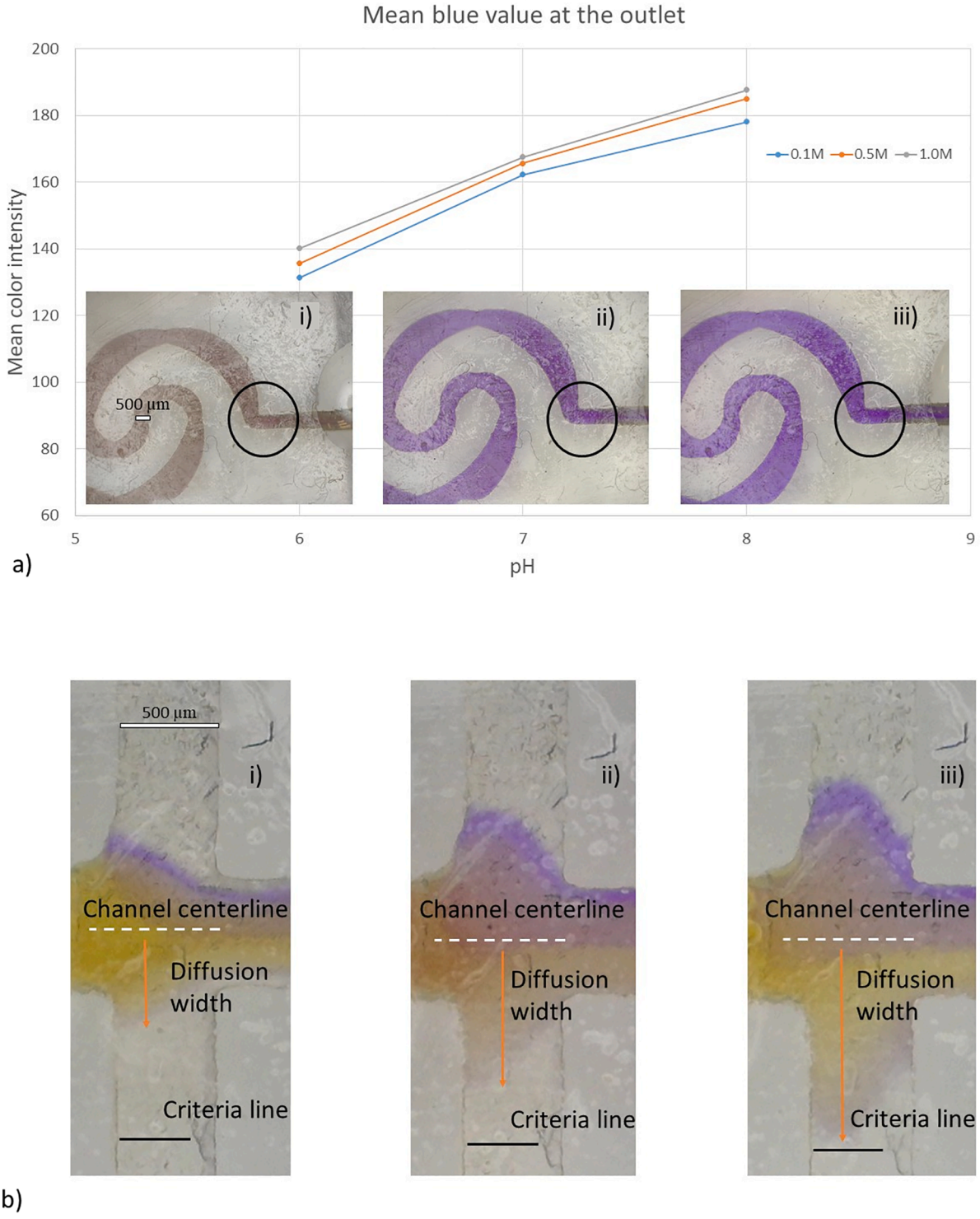

Fig. 6. a) Colorimetric analysis of the mixture of the BCP and the buffer solutions at the outlet. The transition of color in the range of pH 6.0 to 7.0 is quite obvious, but for the range of pH 7.0 to 8.0 further investigation and accurate measurements are necessary. Pictures (i), (ii) and (iii) show the final mixture of the BCP and buffer solutions with 0.5 M of HEPES at pH 6.0, 7.0 and 8.0, respectively. b) shows the reaction of BCP and buffers with different pH levels at the intersection of the inlets. The upper inlet was dedicated to the buffers with pH 8.0 and through the bottom inlet, the buffer with pH 6.0 was injected. Pictures (i), (ii) and (iii) show the reaction of buffers with 0.1, 0.5 and 1.0 M of HEPES, respectively.

1.0 M of HEPES, respectively.

The same procedure was carried out for the buffer solutions at pH 7.0 level. Predictably, the assay provided similar results to the previous test. Since the resulted color change from the reaction of BCP and HEPES solution at pH 7.0 is more vivid as the pH rises, it was less complicated to track the reaction inside the lateral channel. This claim is also supported by the calculated standard deviations. The reported errors were showing a meaningful retrenchment as the pH was increasing. With respect to Fig. 5 – b, higher molarities resulted in an increase in the diffusion width. Furthermore, the results showed that the mean diffusion width for the buffer with 0.1 M of HEPES remained at 172.566 μm. On the other hand, the mean diffusion width for the other buffer solutions (0.5 and 1.0 M of HEPES) incremented to 427.71 and 633.33 μm. According to the results, the diffusion width of the 0.1 M HEPES solution didn't experience a change during the assay. This can be interpreted into the fact that solution with 0.1 M of HEPES has a limited amount of free conjugate ions and they are already saturated at pH 6.0 level, even though the reaction is more detectable at pH 7.0 rather than pH 6.0. With the same interpretation, the cause of increase in the diffusion width of the other solutions can be inferenced. In other words, buffer solutions (with 0.5 and 1.0 M of HEPES) have not yet reached to their capacity limits and due to their higher molarities, they can intensify the diffusion inside the channel. As a result, the indicator molecules can diffuse deeper inside the lateral channel. The results are also indicating that the capacity of 0.1 M buffer solution is limited for tests at pH levels lower than 6.0, since tracking the color change would be quite challenging in those ranges and also the solution's pH would be very close to the BCP's lower transition range and this can considerably affect the errors (see Table 4 in the supplementary materials).

The procedure was repeated for the buffer solutions at pH 8.0 level. The mentioned pH level is beyond the BCP's upper transition range and this maximizes the blue color intensity of the reaction. As it is displayed in Fig. 5 – c, by increasing the HEPES molarity, the mean diffusion width increased in the buffers with 0.5 and 1.0 M of HEPES. However, the reported increase for the 0.5 M HEPES buffer solution was quite limited (439.76 μm at pH 8.0 in comparison to the 427.71 μm at pH 7.0). Warning that the buffer is on the verge of being saturated. On the other hand, for the solution with 1.0 M of HEPES the mean diffusion width was increased to 700 μm, showing a 10% growth in the diffusion. The mean diffusion width for the buffer solution with 0.1 M of HEPES was in agreement with the reported values for the lower pH levels, supporting the previously provided justifications.

3.2.2. pH buffer analysis

The buffer solutions' pH was evaluated at the outlet of the spiral mixer. As it had been previously reported (Mehrdel et al., 2018), the spiral micromixer can provide mixtures with high homogeneity at Reynolds number range of 0.1 to 10.0. Since the pH indicator's color change needs to be done at the point where the solutions and the BCP are acceptably mixed. Thus, the mixture was analyzed at the outlet of the mixer. According to Fig. 6 – a, solutions with the same pH level retained to the same domain of mean blue color intensity, regardless of their HEPES molarity. It should be mentioned that, increasing the HEPES molarity resulted in a slight rise in the mean blue color intensity. However, those rises were negligible compare to the jumps in the color intensity due to the pH increase. At pH 6.0, the mixtures' mean blue color intensity stood at 135.681, while for the solutions with 0.1 M of HEPES the reported value was 131.32 and for the buffer with 1.0 M of HEPES the mentioned value was 140.078. Meaning that a difference of $\pm$ 4.4 units (of mean blue color intensity) was observed in analyzing the solutions with different HEPES molarities at the same pH. But when the pH was increased to 7.0, the mean blue color intensity dramatically increased to 165.144. Whereas, the maximum and the minimum reported values were 162.28 and 167.532 for the buffer solutions with 0.1 and 1.0 M HEPES, respectively. Subsequently, by increasing the pH to 8.0, the mixtures showed the highest blue color intensity. The average value for the mixtures' mean blue intensity color incremented to 183.612, while the solutions with 0.1 and 1.0 M of HEPES showed 178.13 and 187.725 units, respectively. The trend of increase in the mean blue color intensity does not show a linear growth. This behavior can be explained by the fact that the maximum pH level of the BCP's transition range is lower than 8.0 and the mixture cannot illustrate higher pH levels by changing color.

3.2.3. Self-referencing sensor assay

Heretofore, the assay showed that the device is sensitive to changes in HEPES molarity and pH levels. Due to the known behavior of the buffers and also the symmetrical nature of the micromixer, this device is able to be utilized as a self-referencing sensor. In other words, even by visual checking of the BCP and buffers reaction at the evaluation zone (intersection of the inlets) the relative comparison of the buffers can be carried out. The HEPES molarity can be compared via measuring the diffusion width inside channels. Deeper diffusion inside the lateral channels can be translated into higher HEPES concentration or molarity.

If instead of comparing diffusion width, the mean blue color intensity of the peak was compared, the pH of the buffers can be obtained. According to the previous results, as the pH rose up, the mean blue color intensity would be more intense, meaning that it can be utilized for determining which channel is containing a more alkaline buffer (Check Fig. 6 – b). Both of these comparisons can be carried out at the same time and in the same evaluation zone. This technique provides a simple environment to compare buffer concentration and the pH level of two unknown solutions.

4. Conclusion

The use of 3D printed microfluidics provides portability to pH and ionic strength measurements and also the opportunity to control the buffer capacity by evaluating its molarity/concentration.

The results showed that by comparing the diffusion width of the wine (sample) and tartaric acid solutions, it is possible to estimate the total acid concentration in an unknown solution. Whereas the diffusion width of the 1.0 M tartaric acid was reported to be 416.34 μm and for the 0.1 M tartaric acid, the mentioned value was 134.6 μm, while the diffusion width for the pH 3.25 wine sample was 142.54 μm. Indicating that the total acid concentration of the untreated wine (pH 3.25) is close to 0.1 M. The results also illustrated that, the sensor was able to detect a broad range of molarities, from 1.0 M to 0.1 M and lower. Whereas, the reported detection error never went beyond 20 μm. A value that could comfortably fit within the diffusion width of conventional wines.

The proposed design was also capable of measuring the pH of wine solutions, based on monitoring of the mean green intensity profile of the reaction between the pH indicator and the sample. The results showed that even slight changes in the pH value could be interpreted by monitoring the color change of the pH indicator at a given flowrate. According to the investigations, the mean green value difference was reported as 51.01 for wine samples at pH 3.25. Whereas, that value was reported as 36.26 for the wine solutions at pH 3.74. The standard deviation for pH measurement never went beyond 1.84, meaning that the setup could easily detect the pH variations of 0.25 units.

The same approach was applied to study buffered solutions. The proposed methodology was successful in measuring buffer capacities from 0.1 M to 1 M. At the lowest resolution, the sensor was able to detect the 471.43 μm of diffusion width for the 1.0 M buffer solution at pH 6.0 and displayed a maximum detection error of 39.38 μm. Increasing the pH and as a result, intensifying the color change of the pH probe, enhanced the resolution and lowered the detection error to 11.50 μm (172.56 μm for the 0.1 M buffer solution at pH 8.0). Besides, pH evaluation was conducted as well at the outlet of the mixer. This study showed that the 3D printed device could be successfully employed in order to detect buffers in the pH range of 6.0 up to 8.0, as the investigation showed a 21.7% mean blue color difference between buffer

solutions with pH 6.0 and 7.0. All in all, the investigation showed that the proposed sensor opens the opportunity to measure some key chemical characteristics, such as ionic strength, pH and buffering capacity, with minimum requirement of samples and equipment in industrial or production sites.

Funding

This study was partially supported by the Health Institute Carlos III (ISCIII): Health Technological Development project grant number DTS16/00133 from the Spanish Government together with the European regional development Funds (FEDER) and the Spanish Ministry of Economy and Competitivity, grant nos. CTQ2016-77936-R (funding also from FEDER) and CTQ2017-84966-C2-1-R.

CRediT authorship contribution statement

Pouya Mehrdel: Methodology, Software, Validation, Formal analysis, Investigation, Data curation, Writing - original draft, Visualization. **Shadi Karimi:** Conceptualization, Validation, Resources, Visualization, Writing - review & editing. **Josep Farré-LLadós:** Conceptualization, Resources, Writing - review & editing. **Jasmina Casals-Terré:** Conceptualization, Resources, Writing - review & editing, Supervision, Project administration, Funding acquisition.

Declaration of Competing Interest

The authors declare that they have no known competing financial interests or personal relationships that could have appeared to influence the work reported in this paper.

Acknowledgments

The authors are thankful of Universitat Politecnica de Catalunya (UPC) for providing the required materials. We are also highly grateful of CELBIOTECH Lab., and particularly Prof. Teresa Vidal Llucia for the assistance and providing the technical support.

Appendix A. Supplementary data

Supplementary data to this article can be found online at https://doi.org/10.1016/j.foodchem.2020.128583.

References

Angelkov, D., & Martinovska, B. (2018). Sensor Module for Monitoring Wine Fermentation Process. *Applied Physics, System Science and Computers, 428*, 245–251. https://doi.org/10.1007/978-3-319-53934-8.

Boukhobza, I., & Crans, D. C. (2020). Application of HPLC to measure vanadium in environmental, biological and clinical matrices. *Arabian Journal of Chemistry, 13*(1), 1198–1228. https://doi.org/10.1016/j.arabjc.2017.10.003.

Cabot, J. M., Fuguet, E., Rosés, M., Smejkal, P., & Breadmore, M. C. (2015). Novel Instrument for Automated pKa Determination by Internal Standard Capillary Electrophoresis. *Analytical Chemistry, 87*(12), 6165–6172. https://doi.org/10.1021/acs.analchem.5b00845.

Chen, S. H., Chao, A., Tsai, C. L., Sue, S. C., Lin, C. Y., Lee, Y. Z., … Wang, T. H. (2019). Utilization of HEPES for Enhancing Protein Transfection into Mammalian Cells. *Molecular Therapy - Methods and Clinical Development, 13*(5), 99–111. https://doi.org/10.1016/j.omtm.2018.12.005.

Dzebic, M., Kurikov, O., Dobroliubov, O., & Nava, O. C. A. (2017). Design and Fabrication of a PDMS Microfluidic Device for Titration of Biological Solutions. *IFMBE Proceedings, 62*. https://doi.org/10.1007/978-981-10-4166-2_18.

Ethier, C. R., & Simmons, C. a. (2007). Introductory Biomechanics From Cells to Organisms. In Introductory Biomechanics - from Cells to Organisms. https://doi.org/10.1017/CBO9780511809217.

Fuguet, E., Ràfols, C., Bosch, E., & Rosés, M. (2009). A fast method for pKa determination by capillary electrophoresis. *Chemistry and Biodiversity, 6*(11), 1822–1827. https://doi.org/10.1002/cbdv.200900120.

Fukuhara, G. (2020). Analytical supramolecular chemistry: Colorimetric and fluorimetric chemosensors. *Journal of Photochemistry and Photobiology C: Photochemistry Reviews, 42*. https://doi.org/10.1016/j.jphotochemrev.2020.100340.

Ghoneim, M. T., Nguyen, A., Dereje, N., Huang, J., Moore, G. C., Murzynowski, P. J., & Dagdeviren, C. (2019). Recent Progress in Electrochemical pH-Sensing Materials and Configurations for Biomedical Applications [Review-article]. *Chemical Reviews, 119*(8), 5248–5297. https://doi.org/10.1021/acs.chemrev.8b00655.

Gong, H., Beauchamp, M., Perry, S., Woolley, A. T., & Nordin, G. P. (2015). Optical approach to resin formulation for 3D printed microfluidics. *RSC Advances, 5*(129), 106621–106632. https://doi.org/10.1039/c5ra23855b.

Grigore, A., Albulescu, A., & Albulescu, R. (2018). Current methods for tumor-associated macrophages investigation. *Journal of Immunoassay and Immunochemistry, 39*(2), 119–135. https://doi.org/10.1080/15321819.2018.1488727.

Honorato, R. S., Araújo, M. C. U., Lima, R. A. C., Zagatto, E. A. G., Lapa, R. A. S., & Costa Lima, J. L. F. (1999). A flow-batch titrator exploiting a one-dimensional optimisation algorithm for end point search. *Analytica Chimica Acta, 396*(1), 91–97. https://doi.org/10.1016/S0003-2670(99)00366-9.

Kim, M. J., Jung, S. W., Park, H. R., & Lee, S. J. (2012). Selection of an optimum pH-indicator for developing lactic acid bacteria-based time – temperature integrators (TTI). *Journal of Food Engineering, 113*(3), 471–478. https://doi.org/10.1016/j.jfoodeng.2012.06.018.

Li, L., Lieleg, O., Jang, S., Ribbeck, K., & Han, J. (2012). A microfluidic in vitro system for the quantitative study of the stomach mucus barrier function. *Lab on a Chip, 12*(20), 4071–4079. https://doi.org/10.1039/c2lc40161d.

Matthews, M. A., Ishii, R., Anderson, M. M., & O'Mahony, M. (1990). Dependence of wine sensory attributes on vine water status. *Journal of the Science of Food and Agriculture, 51*(3), 321–335. https://doi.org/10.1002/jsfa.2740510305.

Mehrdel, P., Karimi, S., Farré-Lladós, J., & Casals-Terré, J. (2018). Novel variable radius spiral-shaped micromixer: From numerical analysis to experimental validation. *Micromachines, 9*(11). https://doi.org/10.3390/mi9110552.

Oliveira, S. M., Lopes, T. I. M. S., Tóth, I. V., & Rangel, A. O. S. S. (2010). Simultaneous determination of tartaric acid and potassium in wines using a multicommuted flow system with dialysis. *Talanta, 81*(4–5), 1735–1741. https://doi.org/10.1016/j.talanta.2010.03.032.

Osborn, J. L., Marshall, L., Holstein, C., Ball, C., Lutz, B., Fu, E., & Yager, P. (2011). A self-referencing paper T-sensor for analyte detection. 15th International Conference on Miniaturized Systems for Chemistry and Life Sciences 2011, MicroTAS 2011, 1 (January), 479–481.

Persat, A., Chambers, R. D., & Santiago, J. G. (2009). Basic principles of electrolyte chemistry for microfluidic electrokinetics. Part I: Acid-base equilibria and pH buffers. *Lab on a Chip, 9*(17), 2437–2453. https://doi.org/10.1039/b906465f.

Preedy, V. (2016). Electronic Noses and Tongues in Food Science Series Editor.

Prenesti, E., Berto, S., Toso, S., & Daniele, P. G. (2012). Acid-base chemistry of white wine: Analytical characterisation and chemical modelling. *The Scientific World Journal, 2012*. https://doi.org/10.1100/2012/249041.

Prenesti, E., Toso, S., Daniele, P. G., Zelano, V., & Ginepro, M. (2004). Acid-base chemistry of red wine: Analytical multi-technique characterisation and equilibrium-based chemical modelling. *Analytica Chimica Acta, 507*(2), 263–273. https://doi.org/10.1016/j.aca.2003.11.025.

Rodríguez-Méndez, M. L., De Saja, J. A., González-Antón, R., García-Hernández, C., Medina-Plaza, C., García-Cabezón, C., & Martín-Pedrosa, F. (2016). Electronic noses and tongues in wine industry. *Frontiers in Bioengineering and Biotechnology, 4*(OCT), 1–12. https://doi.org/10.3389/fbioe.2016.00081.

Sahu, P. K., Ramisetti, N. R., Cecchi, T., Swain, S., Patro, C. S., & Panda, J. (2018). An overview of experimental designs in HPLC method development and validation. *Journal of Pharmaceutical and Biomedical Analysis, 147*, 590–611. https://doi.org/10.1016/j.jpba.2017.05.006.

Sanz, D. T. (2014). Wine and its analysis. Universidad Complutense de Madrid. https://eprints.ucm.es/29446/8/PIMCD No 243. ANEXO 2. E-BOOK- WINE AND ITS ANALYSIS.pdf.

Sobolev, A. P., Thomas, F., Donarski, J., Ingallina, C., Circi, S., Cesare Marincola, F., … Mannina, L. (2019). Use of NMR applications to tackle future food fraud issues. *Trends in Food Science and Technology, 91*(July), 347–353. https://doi.org/10.1016/j.tifs.2019.07.035.

Versari, A., Laurie, V. F., Ricci, A., Laghi, L., & Parpinello, G. P. (2014). Progress in authentication, typification and traceability of grapes and wines by chemometric approaches. *Food Research International, 60*, 2–18. https://doi.org/10.1016/j.foodres.2014.02.007.

Wilson, A. D. (2013). Diverse applications of electronic-nose technologies in agriculture and forestry. *Sensors (Switzerland), 13*(2), 2295–2348. https://doi.org/10.3390/s130202295.

sensors

MDPI

Article

Flow Control in Porous Media: From Numerical Analysis to Quantitative µPAD for Ionic Strength Measurements

Pouya Mehrdel [1,*], Hamid Khosravi [1], Shadi Karimi [1], Joan Antoni López Martínez [2] and Jasmina Casals-Terré [1]

[1] Mechanical Engineering Department—Microtech Lab., Universitat Politecnica de Catalunya, C/Colom 7-11, CP 08222 Terrassa, Spain; hamid.khosravi@upc.edu (H.K.); shadi.karimi@upc.edu (S.K.); jasmina.casals@upc.edu (J.C.-T.)

[2] Department of Mining, Industrial and ICT Engineering (EMIT), Universitat Politecnica de Catalunya, AV. Bases de Manresa 61-73, CP 08240 Manresa, Spain; joan.antoni.lopez@upc.edu

* Correspondence: pouya.mehrdel@upc.edu; Tel.: +34-666-290-677

Abstract: Microfluidic paper-based analytical devices (µPADs) are a promising technology to enable accurate and quantitative in situ assays. Paper's inherent hydrophilicity drives the fluids without the need for external pressure sources. However, controlling the flow in the porous medium has remained a challenge. This study addresses this problem from the nature of the paper substrate and its design. A computational fluid dynamic model has been developed, which couples the characteristics of the porous media (fiber length, fiber diameter and porosity) to the fluidic performance of the diffusion-based µPAD sensor. The numerical results showed that for a given porous membrane, the diffusion, and therefore the sensor performance is affected not only by the substrate nature but also by the inlets' orientation. Given a porous substrate, the optimum performance is achieved by the lowest inlets' angle. A diffusion-based self-referencing colorimetric sensor was built and validated according to the design. The device is able to quantify the hydronium concentration in wines by comparison to 0.1–1.0 M tartaric acid solutions with a 41.3 mM limit of detection. This research showed that by proper adjustments even the simplest µPADs can be used in quantitative assays for agri-food applications.

Keywords: microfluidic paper-based analytical devices; colorimetric detection; quantitative assay; numerical simulation; computational fluid dynamics; ionic strength; diffusion assay

Citation: Mehrdel, P.; Khosravi, H.; Karimi, S.; Martínez, J.A.L.; Casals-Terré, J. Flow Control in Porous Media: From Numerical Analysis to Quantitative µPAD for Ionic Strength Measurements. *Sensors* **2021**, *21*, 3328. https://doi.org/10.3390/s21103328

Academic Editors: Pedro Luis Miribel Catala, Manuel Puig-Vidal and Jordi Colomer-Farrarons

Received: 13 April 2021
Accepted: 6 May 2021
Published: 11 May 2021

1. Introduction

In the past decades, microfluidic technology has proven its capabilities to be used in the chemical, biochemical, food, agri-food, pharmaceutical and medical fields [1–4]. Their fast-responsiveness, low reagent requirement, accuracy and user-friendliness persuade both the researchers and entrepreneurs to focus more on this technology and expand its applicability to new fields and, specifically into the field of Micro Total Analysis Systems (µTAS) [5–8]. Although the microfluidic platforms are extremely efficient, they mostly rely on the utilization of external energy sources to control the flow, and they require the incorporation of sophisticated detection techniques. Therefore, in situ measurements or the use in less developed regions is seriously limited. Researchers have tried to address this last issue by taking advantage of the generated capillary flow in the porous media, which introduced the microfluidic paper-based analytical devices (µPAD) [9–12]. However, the capillary flow is linked to its complex control, which is related to the paper characteristics. This fact restricts the µPADs applications mainly to qualitative detection if they are not supported by sophisticated detection techniques.

Porous media are tangled matrices of fibers (normally cellulosic) that provide an ideal environment for functionalization. However, their intrinsic variability is a challenge for microfluidic designers, and most current successful devices are qualitative or yes/no

assays. Some researchers have taken advantage of the fiber matrix to trap nanoparticles and enhance the surface-to-volume ratio [13–16]. This fact has increased its reliability and repeatability. However, the use of μPADs (by non-trained personnel) as quantitative assays is still in development. For instance, the most conventional and well-known μPADs applications are paper-based pH indicators and pregnancy tests (hCG; human Chorionic Gonadotropin hormone test) [9]. Both use markers (either pH indicator or antibody) immobilized within the porous media. The interaction within the understudy solution and the coated marker causes the expected color change. Nevertheless, there are reports of developed paper-based sensors that can be used in diverse applications by taking advantage of interdisciplinary methods. Examples of such application are reported in the literature, for instance in electrochemical (EC) [17,18], chemiluminescence (CL) [14,18,19] and electrochemiluminescence (ECL) [18,20] methods to quantify different compounds. These quantification methods increase the assays' accuracy and widen the applicability horizon. However, the use of the aforementioned methods does not help to simplify the tests and conflicts with the idea of using μPADs in less developed regions.

Even though, there are numerous reports of developed quantitative μPAD platforms based on laborious detection techniques. There are also remarkable μPADs that provide quantitative or semi-quantitative measurements without the need to use such complex methods. For instance, Kim et al. [21] developed a quantitative colorimetric assay for the detection of Tropinin I, which enhanced the results due to the use of gold nanoparticles. A similar approach was used by Parolo et al. [22] that took advantage of Lateral Flow Immunoassay (LFIA) and used gold nanoparticles to capture human IgG and presented the results through colorimetric techniques. Walczak et al. (2009) [23] proposed a colorimetric assay capable of quantifying down to 5 ng/mL of cocaine in the samples. Gerold et al. [24] managed to distinguish 1.0–2.5 mM of potassium ion on a paper-based microfluidic device by taking advantage of the selective distance-based quantification method. Additionally, there have been reports about the simultaneous detection of several compounds [25,26] or employing smart-phones for the evaluation of the assays [27,28]. However, in most of the aforementioned studies, the research relied on the attachment of the analyte to the pre-treated particles/detectors/substrates, and the effects of the substrate on the devices themselves were not considered.

Other than the requirement of pre-treated substrates or particles, certain assays, such as enzyme-linked immunosorbent assay or ELISA, require a sequential flow of the reagents to the detection zone. Since the fluid movement is not controllable in a porous media, careful strategies should be considered to achieve the sequential arrival of the reagents to the reaction zones. The strategies to control the flow can be categorized into three types: geometrical-based, chemical-based and mechanical-based [29,30]. The geometrical-based methods rely on the change of the channel length, the channel width and any obstruction of the flow path that can delay the fluid arrival to the detection zone. Apilux et al. [31] managed to perform an automatic ELISA for hCG (human Chorionic Gonadotropin hormone) determination by using a baffled paper-based microfluidic channel. Another geometrical-based flow control method is based on the successive placement of fluid sources on the channel to create a paper network. The fluid from the closest source arrives faster than the other sources, and this enables a programmed delivery of reagents to the detection zone. Fu et al. [32] took advantage of this method and introduced a μPAD, which detected malaria proteins in a sandwich immunoassay. Geometrical-based flow control can also be achieved by using shunts. As the fluid is absorbed by a fluid shunt, the flow is slowed down. Once the shunt is filled, the flow gains its initial velocity [29]. Chemical-based flow control relies on altering the porous characteristics of the substrate when compounds are deposited in the voids (pores). For instance, Lutz et al. [33] deposited different amounts of dissolvable sugar to the paper substrate and showed that the fluid flow could be delayed significantly. The mechanical-based flow control is extremely useful for three-dimensional μPADs. This method enables the possibility to place mechanical valves, which create connections between paper-substrates at different levels. In summary, the abovementioned

strategies are ideal for sequential flow assays. However, they do not focus on applications, where co-laminar flows are required, and they do not study the effect of porous media characteristics and geometry on the fluids' interaction.

In one of the well-studied but rare researches, Osborn et al. [34] investigated the effect of the source position in a T-mixer and its influence on the flows within the porous medium. The study displayed that if one of the sources (in the inlets) is placed closer to the inlets' intersection, the respective flow would become dominant in the main channel and overcome the flow from the other inlet. The study pointed out the complexity of controlling the flow in porous media. However, the need for manual positioning and therefore the flow synchronization would decrease the accuracy of this type of device if used in assays.

This study aims to investigate the influence of paper properties and geometry on the flow characteristics. Specifically, the influence on the diffusion in paper-based microfluidic platforms. First, we have modeled the flow behavior in a given porous media, by taking into account the porous media characteristics (fiber length, fiber diameter, porosity) and also the geometry of the porous media microfluidic circuit. Later, based on the outcome, we have conceptualized a self-referencing sensor with a straightforward 3D-printed structure to guarantee the simultaneous contact between the reagents and paper strip that could be utilized everywhere and characterized its accuracy and sensitivity.

The novel proposed sensor can measure the sample's unknown ionic concentration (wine) by comparing its diffusion width to the diffusion width of a solution with a known ionic concentration (tartaric acid). The diffusion width is measured using colorimetric analysis. The optimization of the porous media substrate avoids the use of pre-treated substrates/particles and more sophisticated detection techniques and brings quantification capacity to a paper-based sensor.

2. Methodology

In this section, we present an overview of the governing equations of the flow in porous media. We describe the model of the different studied geometries as well as the materials and experimental approach.

2.1. Sensor Description

The colorimetric sensor measures the diffusion width of hydronium ions [H_3O^+]. The main goal is to monitor the diffusion width through the color change across the measurement line and compare it to the diffusion width of a known sample (self-referencing approach).

The use of the proposed sensor as a threshold sensor or a comparative sensor to a given known ionic strength solution, brought the need to use three inlets: one for the unknown solution, one for the known ionic strength solution and a third solution as a mediator or label (in this study pH indicator). The pH indicator transforms the ionic concentration into a colorimetric signal and enables a simultaneous comparison between the diffusion widths of both solutions (with known and unknown ionic strengths).

With respect to the abovementioned points, the proposed sensor has three inlets: the left one for the sample of interest, the middle one for indicator and the right one for the reference sample. In order to achieve a proper performance of the sensor, the device uses a 3D-printed support, see Figure 1. This support and inlets' geometry have been designed to guarantee that the inlets of the paper substrate contact the fluid reservoirs at the same time and the fluids flow within the porous medium, simultaneously. Therefore, the solutions encounter at the main channel (meeting zone) when required, and the chemical reaction can be monitored. When the H_3O^+ ions of the solution diffuse into the pH indicator, they show a certain color change. If the ionic strength is higher, there will be more ions and therefore more diffusion. If the ionic concentration of the reference solution is known, then the ionic concentration of the solution of interest can be found by comparing its diffusion width to the reference one, as it is shown in Figure 1.

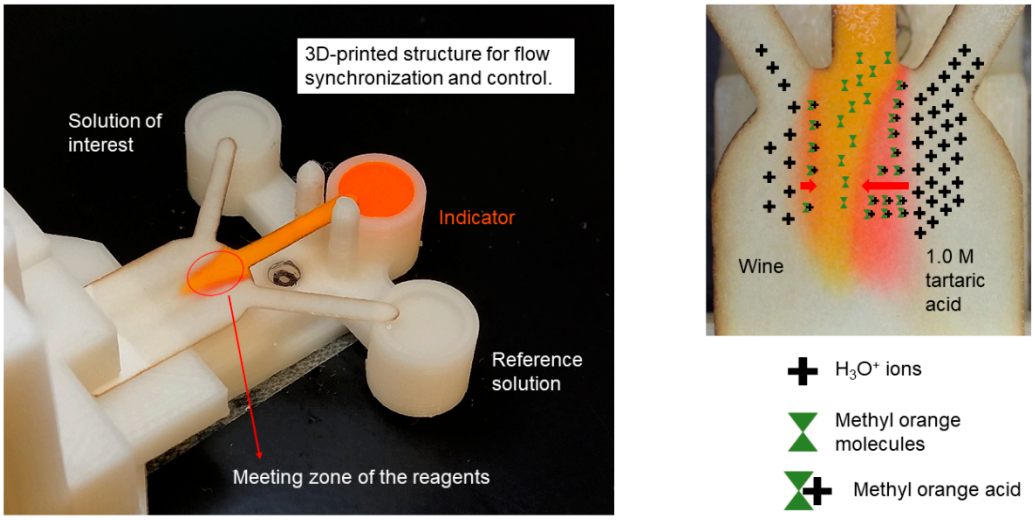

Figure 1. Picture of the ionic strength wine evaluation using a diffusion-based µPAD and the flow control system. Red arrows illustrate the diffusion widths due to unequal ionic concentration of solutions in the meeting zone.

2.2. Principles of Numerical Simulation

2.2.1. Fluid Flow and Mixing Phenomena

Computational fluid dynamics (CFD) is a derivation of the finite volume method that discretizes the solving domain into smaller cells and solves the Navier—Stokes equations in each cell. Ansys Fluent CFD software is chosen for solving the equations of the fluid flow through the porous media substrate. We assumed that the fluid is incompressible, Newtonian and the process is isothermal.

For solving the Navier—Stokes equation, a coupled scheme is chosen for the pressure-velocity coupling. Due to the dimensions, laminar flow is the governing regime and the energy and thermal sources are negligible, the continuity (1) and momentum (2) equations solved at each cell are:

$$\nabla \vec{U} = 0, \tag{1}$$

$$\rho \vec{U} \cdot \nabla \vec{U} = -\nabla P + \mu \nabla^2 C \tag{2}$$

In the above equations $\vec{U}$ is the velocity vector, ρ is the density of the working fluid, ∇P is the pressure gradient and C is the species concentration within the solving domain.

A user defined scalar is introduced to model the diffusion of species in the control volume.

The assumption of laminar flow implies that the convection-diffusion Equation (3) describes the transport phenomena in the domain of interest. The convection-diffusion equation is defined as:

$$\rho \vec{U} \cdot \nabla C = D \nabla^2 C, \tag{3}$$

Let the D be the diffusion coefficient of the species.

In order to simulate the diffusion in the problem, the Equation (3) is solved simultaneously with continuity and momentum Equations (1) and (2) at each iteration.

2.2.2. Numerical Modelling of the Paper Substrate

The substrate is defined as a porous medium and the geometry is segregated into three zones. Two zones are the lateral inlet branches and the other zone contains the middle inlet and main channel. The porous medium is defined in Fluent by its porosity and the viscous resistance values (1/permeability (α)), which are identical for all the zones. The only difference is in their magnitude of the X and Y vectors. These values are calculated

based upon the inlets' angle and defined in the opposite direction of the flow to define the resistance against the fluid movement.

It is worthy to mention that the inertial resistance is neglected in the model, since it is completely overshadowed by the viscous resistance. Calculations showed that the viscous resistance is greater than the inertial resistance by approximately 1×10^3 magnitude of order. Also, it should be noted that the authors are aware of the fact that the wetting phenomenon swells the fibers. But since the material of the paper-substrate is the same in all the cases and the same reagents are used, the authors have presumed that the permeability and the viscous resistance has remained unchanged for the sake of simplification.

2.2.3. Porous Medium

Whatman grade 5 paper, bought from @Fisher Scientific, is used as the assay substrate.

Porous media are tortuous matrices of fibers that are packed together creating some voids (or in other words; pores) [35]. The fluid flows within the pores and is affected by the size of the pores and their distribution. One of the most important characteristics of the porous medium is its porosity (ε) that can be calculated through:

$$\varepsilon = \frac{V_v}{V_O} \tag{4}$$

where, V_v and V_O are representing the void volume and the body volume of the understudy medium.

The total volume of the paper consists of the voids volume plus the fibers (or particles) volume. Therefore, the porosity of the medium can be correlated with the density of the whole porous medium (ρ_0) and the density of its constituent fibers/particles (ρ_p). As a result, the porosity can be calculated as:

$$\varepsilon = 1 - \frac{\rho_p}{\rho_0} \tag{5}$$

The permeability (α) of the porous medium, according to Yazdchi et al. [36], can be obtained from the physical and geometrical properties of the substrate, rather than the pressure drop and flow velocity within the porous medium. The equation is described as:

$$\frac{\alpha}{d^2} = \frac{\varepsilon^3}{\varphi\left(\frac{L_e}{L_f}\right)^2(1-\varepsilon)^2} \tag{6}$$

where, L_f, L, d and φ are fiber's length, substrate's total length, fiber's diameter and the pore shape factor, respectively.

Table 1 summarizes the geometrical and physical properties of cellulose fibers, present in Whatman 5 paper. Therefore, from Equation (5), the Whatman 5 paper porosity can be obtained (0.6467). The permeability (α) is calculated from equation 6, being 4.551×10^{-15} m^2, which was then used in the definition of porous zone in the Fluent Model.

Table 1. Paper substrate and cellulose fiber characteristics.

Property	Value
Density of Cellulose ($\rho_{\text{cellulose}}$)	1.5 gr/cm^3 [35]
Diameter of the cellulose fiber (d)	19.6 µm [35]
Average length of the cellulose fiber (L_f)	830 µm [35]
Density of Whatman grade 5 paper (ρ_{W5})	0.53 gr/cm^3 [35]
Pore shape factor (φ)	140 [36]
Length of the substrate (L)	30 mm
Substrate main channel width (W_{ch})	10.5 mm
Substrate inlet channel width (w_i)	2 mm
Substrate inlet channel length (l_i)	15 mm

Porous medium also affects the effective diffusion coefficient. The geometry of the substrate will be optimized based on the comparison of the diffusion of the user-defined scalar in the numerical models. According to Giri [37], the diffusion coefficient of a dye molecule (mathematically defined as the scalar) is reported to be 2×10^{-10} m^2/s. Ansys Fluent software requires the diffusion coefficient (D) to be in [kg/m.s] unit. Therefore, D is multiplied by the fluid density before using it in computations. Furthermore, to model the porous zone in the Fluent Model, the effective diffusion coefficient (D_{eff}) is calculated through [38]:

$$D_{eff} = (D \cdot \rho) \cdot \varepsilon \quad (7)$$

Therefore, according to Equation (7) the effective diffusion coefficient in the Fluent model is set to 1.29×10^{-7} kg/m·s.

2.2.4. Boundary Conditions

The initial scalar's concentration is assumed to be 0.05 M in lateral channels. Besides, the working fluid is assumed to be liquid water at RT (25 °C) and 50% (HR), see Table 1. The initial flow velocity at the inlets is set to 1.39×10^{-4} m/s (value estimated from initial measurements of the time required to fill the inlet branches). The convergence residuals are set to 1×10^{-10} for all the criteria. Other properties, such as the pressure outlet condition, the density of fluid, the diffusivity of the scalar, the porosity and the viscous resistance (1/permeability) are summarized in Table 2.

Table 2. Physical properties of fluids and physical characteristics of paper substrate.

Property	Value
Water density (at 25 °C)	998.2 kg/m^3
Water viscosity (at 25 °C)	0.001003 kg/m·s
Diffusion coefficient of dye (D)	2×10^{-10} m^2/s [37]
Porosity of the Whatman 5 porous media	0.6467
Viscous permeability	4.551×10^{-15} m^2

2.2.5. Grid Independency

A grid independency analysis is done to make sure that the size of the discretized cells does not affect the final results. Six mesh densities of the 90-degree model (see Figure 2) are compared.

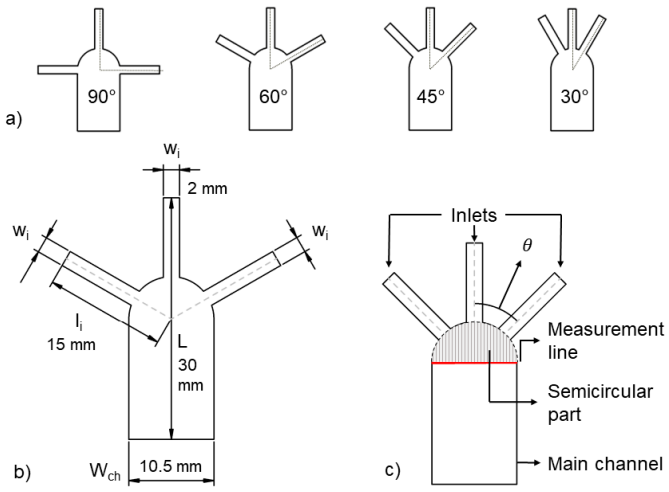

Figure 2. Schematics of the substrate geometry. (**a**) from left to right: Substrate geometries of the 90, 60, 45 and 30-degree models. Channel width (W_{ch}), paper strip length (L), inlets branch width (w_i) and measurement line are also displayed in (**b**,**c**).

The boundary conditions and the solving methods are identical in all the cases.

The minimum element size of the mesh schemes varies from 500 µm in the "Low" mesh density to 25 µm in the "Ultra-fine" mesh density (detailed description of the mesh schemes is presented in the Appendix A). Due to the porous nature of the control surface, the differences in the velocity profiles are quite insignificant. As a result, the scalar distribution in the different mesh designs is set as a reference for comparison.

2.2.6. Diffusion Evaluation Methods

One of the most common methods to evaluate the distribution of species is the comparison of the scalar concentrations at each cell to the median value [39]. This method uses the following dimensionless and normalized ratio: (σ).

$$\sigma = \frac{(C_i - \overline{C})}{(C_{max} - \overline{C})} \tag{8}$$

where C_i is the calculated concentration at the ith cell. $\overline{C}$ denotes the median concentration in the solving domain and C_{max} is the highest concentration of species. By obtaining the normalized ratio σ, the mixing quality ($M.Q$) is calculated in each mesh scheme.

$$M.Q = 1 - \sqrt{\frac{1}{N} \times \sum_{1}^{N} (\sigma^2)} \tag{9}$$

where N is the number of discretized cells in each mesh density and it depends on the minimum element size. The larger the minimum element size, the smaller the number of cells.

2.3. Geometry

Figure 2a shows the four different models created to study the effect of the inlets' orientation on the diffusion width. The angle between the middle inlet and the lateral inlets varies from 90°, 60°, 45° and 30° degrees. Hereinafter, the introduced geometries are referred to as 90-degree, 60-degree, 45-degree and 30-degree models.

For a proper comparison, all the models share the same total length of the paper strip, the required fluid volume to fill the inlet's branch and the distance from the fluid source to the center of the main channel. Therefore, the total length (L), inlets' width (w) and the channel width (W_{ch}) are set to 30 mm, 2 mm and 10.5 mm, respectively. (Please see Figure 2b)

The top of the main channel starts with a semi-circular shape, see Figure 2c. This decision is made in order to make sure that the change in inlets' angle does not affect other characteristics of the design. The semi-circular part has a 10.5-mm diameter and its center is exactly located at the middle of the main channel. Figures 1 and 2c show that the addition of this part not only guarantees the equal geometrical preconditions for all the models, but also brings flexibility in designing different models.

The length of the inlets' branches ($l_c = l_i - W_{ch}/2$) from the fluid source up to the edge of the semi-circular part is kept constant due to the presence of this circular beginning of the main channel. Therefore, l_c is 9.75 mm in all the models, regardless of the inlets' angle.

The measurement line, as shown in Figure 2c, is set at the intersection of the main channel and the semi-circular's part.

2.4. Experimental Setup

In order to verify the numerical simulation results and to evaluate the proposed sensor performance, several experimental assays are designed. The studied geometries (30-degree, 45-degree and 90-degree models) are laser cut (using NEJE7000mW laser) in Whatman grade 5 paper.

A 3D-printed support is developed to keep the paper substrate fixed. This printed support facilitates a simultaneous contact of the three inlets of the paper strip to the reagents.

To evaluate the results, pictures are taken at different time intervals and the diffusion widths are studied over the measurement line. It should be noted that to avoid viscosity variations all the experiments are conducted at the room temperature (RT, 25 °C).

2.4.1. Reagents

Conventional white table wine (pH 3.25 at RT) is supplied locally. Tartaric acid (2,3-Dihydroxybutanedioic acid), is bought from @Merck Schuchardt OHG. Tartaric acid is one of the main components of wines. Three concentrations of 0.1, 0.5 and 1.0 M of tartaric acid are prepared. Measurements at the RT shows that the prepared tartaric acid solution had a pH of 2.9, 2.08 and 1.68, respectively.

Due to the pH range of wines and tartaric acid solutions (generally at or lower than pH 3.7), Methyl orange (Sodium 4-{[4-(dimethylamino)phenyl]diazenyl}benzene-1-sulfonate) is selected as the pH indicator (its pH transition range is between 3 and 4). To prepare the methyl orange indicator, 0.1 g of methyl orange is dissolved in 80 mL of water. Then, ethanol (95%) is added to reach a total volume of 100 mL. The physical Physical properties of the used reagents are presented in Table 3.

Table 3. Physical properties of white wine and tartaric acid at room temperature (25 °C).

Property	Value
White wine density	1080 kg/m^3
White wine viscosity	0.00148 kg/m.s [40]
Tartaric acid molar mass	150.078 g/mol
Tartaric acid viscosity	0.00121 kg/m.s (from producer's catalogue)

2.4.2. 3D Printed Support

One of the challenges of the paper-based microfluidics diffusion-based sensors is achieving a concurrent contact between the inlets' samples and the indicator. Therefore, a 3D-printed support has been designed to avoid the human error factor in substrate positioning and to achieve simultaneous flow between inlets. The 3D structure, as illustrated in Figure 3a,b, consists of 5 parts: the chassis, the reservoirs, the vertically adjustable arm, the paper holder and a screw.

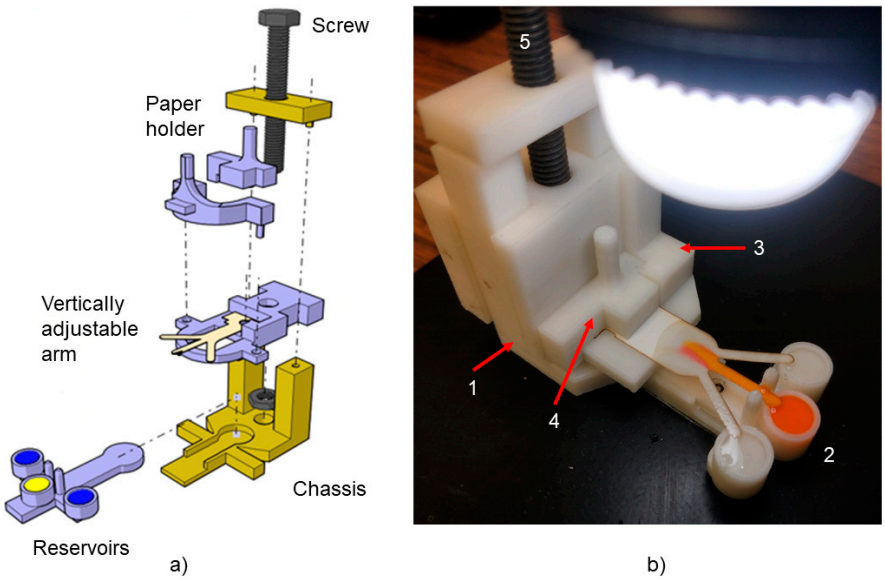

Figure 3. 3D-printed support. (**a**) Assembly of the different parts. (**b**) Picture of a test under performance.

The chassis (number 1 in Figure 3b) is a horizontal plate that stabilizes and bears the whole setup. The chassis has an internal thread (for the screw to enter in) and a section to hold and fix the reservoir.

To evaluate the effect of the inlets' angle on the diffusion, three reservoir models are developed to fit the 30-degree, 45-degree and 90-degree paper strips (number 2 in Figure 3b). This part has three cylindrical containers, which are filled with 60 μl of the solution.

The other part is the vertically adjustable arm (number 3 in Figure 3b). This part is connected to the chassis using only the screw (number 5 in Figure 3b) and it enables the simultaneous contact between the reagents and the inlets of the paper strip. The paper holder (number 4 in Figure 3b) is fabricated to make sure that the paper is fixed and does not move during the tests.

The abovementioned parts are designed with CATIA V5 software and the resulting ".STL" files are printed by a ZORTRAX M200 3D -printer. The material used for fabricating the parts is Z-ULTRAT (ABS- Acrylonitrile Butadiene Styrene).

2.4.3. Measurement Configuration

Since the diffusion width evolves while there is a species gradient (see Equation (3)), there is the need to establish a benchmark time to produce repeatable and accurate results. Once the diffusion width is established, this is measured through the RGB profile analysis of the reaction between the reagents and the pH identifier in the meeting zone. The measurement evaluates the intensity change in the green color channel. Initially, methyl orange has a solid yellow (light orange) color in its neutral form. When hydronium (H_3O^+) from the sample of interest (acids pH < 4) diffuse into methyl orange, the pH indicator experiences structural changes and reflects a red color. The beginning of the reaction causes a drop in the intensity of the green channel, since the yellow color shifts to red and subsequently the constituent green color index decreases.

To determine the measurement time, the moment when the intensity of the green channel starts to drop is set as the "Time zero" and the pictures for analysis are taken at certain intervals (60, 90, 120, 180 and 240 s) after the "Time zero". Numerous trials showed that this strategy is legit, repeatable and can be applied to all the cases. The pictures of the measurement line (as shown in Figure 2c) are captured by the Dino-Lite MS325B microscope. The ambient and the projected light are the same in all the assays and the pictures are later analyzed by the ImageJ software.

Finally, the limit of detection value (*LOD*) is calculated through the following formula: (detailed description of the *LOD* is presented in the Appendix B.

$$LOD = 3.3 \times \frac{S}{m} \tag{10}$$

where S is the standard deviation between the actual values and the predicted values by the calibration plot and m is the slope of the regression line.

2.4.4. Errors and Data Curing

There are two main sources of error in this work: numerical simulation errors and the empirical test errors. Careful efforts are made to guarantee that the mathematical model is in agreement with the true flow. The effect of discretization is considered and the cells' sizes are chosen accurately to not influence the final results. Also, the residuals of the results between consecutive iterations are properly chosen to not produce a false convergence.

In the experimental section, the errors might have been caused by the staff and/or by the devices. Numerous experiments (at least 5 tests for every configuration of solutions on each model) are conducted in order to minimize these effects. Moreover each group of dataset is analyzed and the standard deviation (*S.D*) is calculated through:

$$S.D = \sqrt{\frac{\sum_i^N \left(C_i - \overline{C}\right)^2}{N}} \tag{11}$$

Let C_i, $\overline{C}$, i and N be the value of interest at the ith pixel, mean value of interest in the population, arbitrary variable and the total number of population in the analysis, respectively.

In order to avoid the picture capturing errors (such as light reflection and the ambient light) the microscope is positioned in a manner to receive the minimum reflection and its position is kept still during the assays. Besides, the magnification rate is constant for all the models. Also, the ambient light is measured and the background light is adjusted to be uniform in all the tests.

Eventually, the Grubb's test is applied to all the obtained results to detect the outliers at a 0.05 significance level to minimize the effect of the abovementioned errors.

3. Results and Discussion

3.1. Numerical Simulation

A detailed report on the mesh refinement is presented in Appendix A: Grid study. The mixing quality is studied to see the effect of the mesh scheme on the produced result. Figure 4 shows a comparison of the different meshes. "Fine", "Ultra" and "Ultra-fine" meshes provide similar results. For instance, the species distribution of the "Fine" mesh scheme only showed a 0.9% deviation from the "Ultra-fine" mesh design. Therefore, the "Fine" mesh distribution is selected to perform the study.

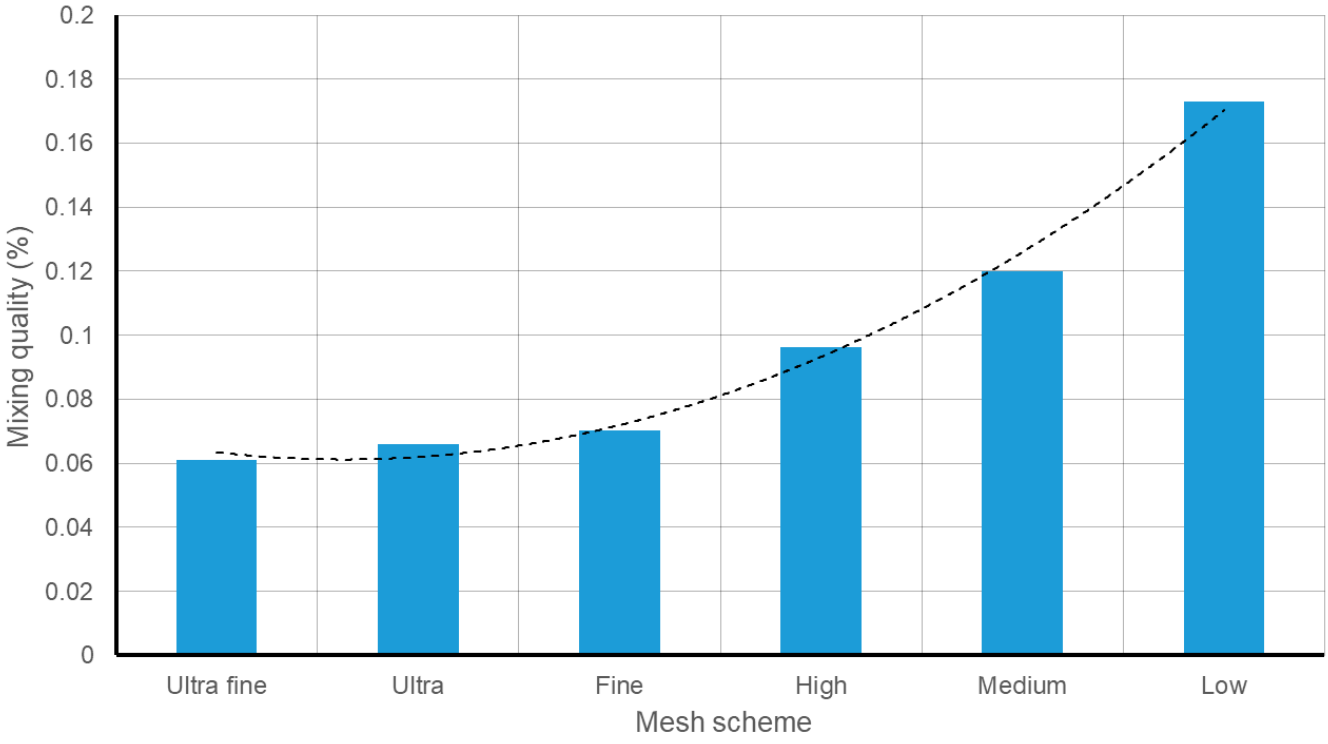

Figure 4. Mixing quality based on the applied mesh scheme.

Numerical Analysis of Inlets' Angle Effect on the Species Diffusion in the Porous Medium

Previous conventional microfluidics studies reported an enhancement of diffusion velocity, depending on the inlets' angle [41]. Thus, four different substrate geometries with inlets' angle of 30, 45, 60 and 90 degrees are modeled and simulated to study if the same effect is relevant in porous substrates.

Figure 5 shows the numerical simulation results of the diffusion width at the measurement line for the different models. According to the results, there is a reinforcing effect due to the inlets' angle. When the lateral inlets are closer to the middle inlet (smaller angle), the diffusion width becomes wider. The reported diffusion width for the 90-degree model is 480 µm, while the species diffusion width is 550 µm in the 30-degree model. Figure 6

plots the flow lines for each model. In the case of the 90-degree model, the flow lines from lateral inlets enter the main channel perpendicular to the general direction of the flow. Since there is only one outlet in the design, the flow needs time and space to change direction. According to the results, this required time affects the diffusion. For instance, when the inlets' angle reduces, the deviation from the general direction of the flow in the main channel decreases, and as a result, the species have more time and space to diffuse.

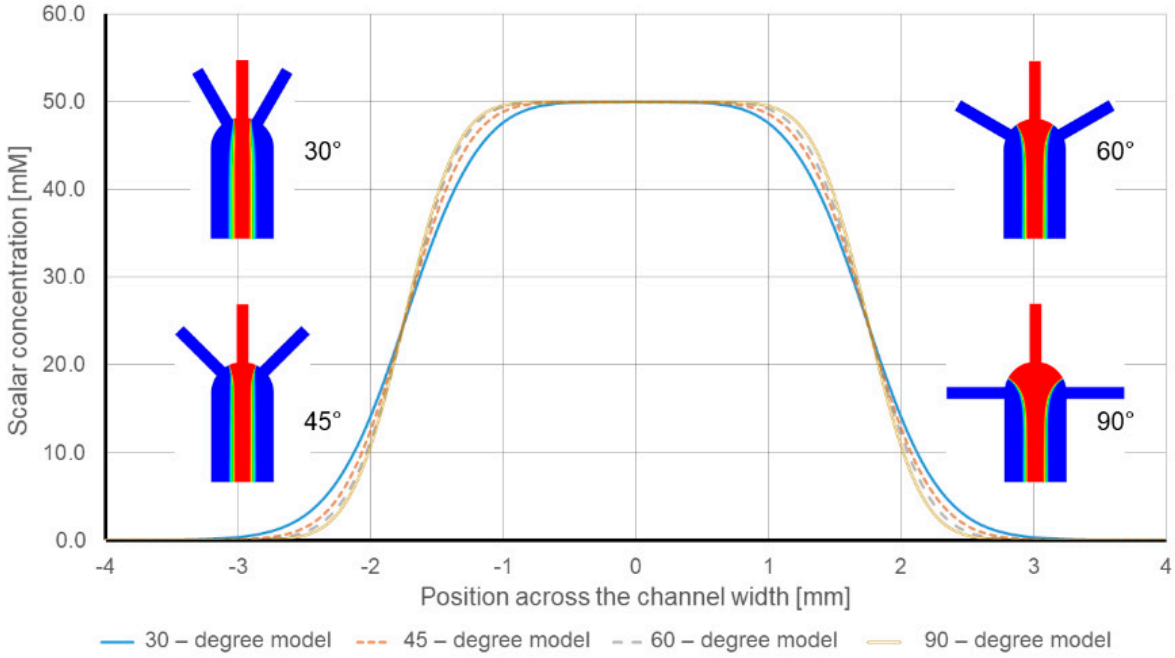

Figure 5. Numerical model results of the Species diffusion width with respect to inlets' angle.

Figure 6 depicts the presence of regions (dead zones) between the inlets, where the flow velocity is at its minimum value. The comparison between the different models shows that these minimum velocity regions shrink by decreasing the inlets' angle. Figure 6a,b shows that as the distance between the inlets increases, the developed dead zone becomes larger. The effect of these dead-zone areas on the diffusion width can be seen in Figure 6c,d. As shown in Figure 6, the diffusion width begins to grow in Figure 6c, where the angle is smaller compared to Figure 6d, which has a larger inlets' angle.

Dead zones show an opposite relation with the diffusion width, a larger dead zone causes a narrower diffusion width at the measurement line. Therefore, the size and the location of the dead zones with diffusion contour can explain the differences of species distribution in different models.

3.2. Experimental Results

Several paper substrate geometries of the 30-degree, 45-degree and 90-degree models are prepared and tested to validate the numerical simulations results. To enhance accuracy, an appropriate substrate support is used for each model, and all the reservoirs are filled with 60 µL of solution.

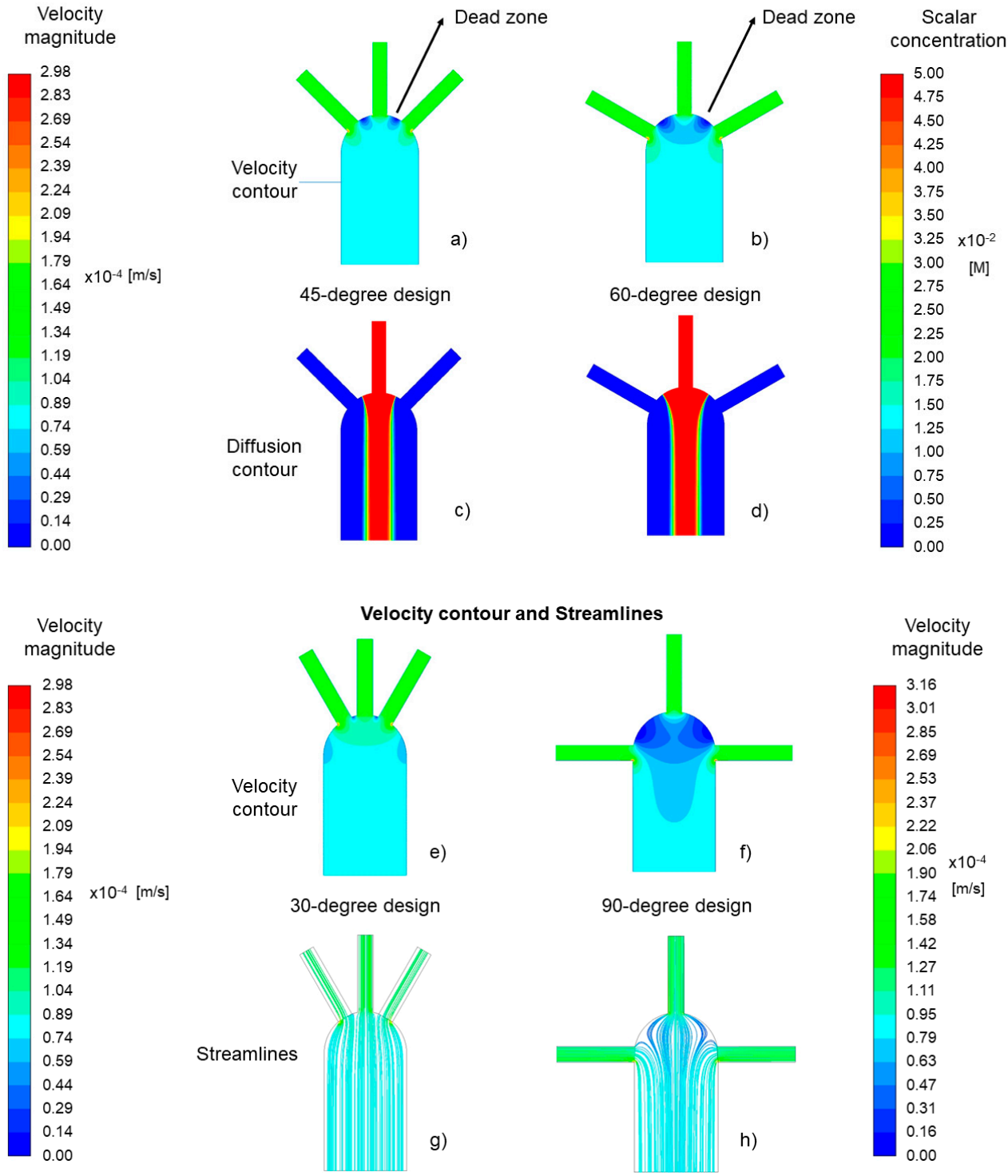

Figure 6. Velocity and diffusion contours of the 45-degree (**a**,**c**) and 60-degree designs (**b**,**d**). Velocity contours and streamlines of the 30-degree model (**e**,**g**) and the 90-degree model (**f**,**h**) are also illustrated.

3.2.1. Relation between Inlets' Angle and the Required Time for Measuring the Diffusion

The time required to develop a 1.5 mm of diffusion width in all the cases is analyzed to establish an accurate protocol to be measured with repeatability by ImageJ software. The evaluation of the diffusion width is conducted on the measurement line.

Figure 7 demonstrates that the required time is related to the inlets' angle and increases from 274.5 s (±68.02 s) in the 30-degree model to 637 s (±113.3 s) in the 90-degree model. This is in agreement with previous numerical results.

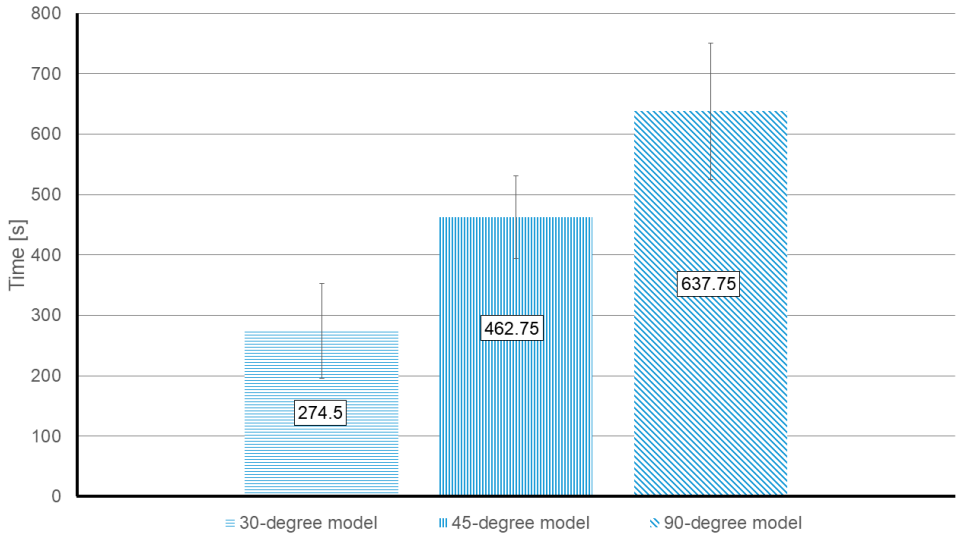

Figure 7. Experimental value of the required time to develop a 1.5 mm diffusion width at the measurement line. The reported values are the median time for each model by considering all the working reagents. The units are in seconds.

Figure 8 compares the interaction between the pH indicator (middle inlet) and the reagents (0.1 M tartaric acid and wine) over the time, in the three different models (30-degree, 45-degree and 90-degree). In the measurements done at 120 s after the "Time zero", the diffusion width increases considerably in the 30-degree and the 45-degree models. Moreover, in the 30-degree model, the shift of the pH indicator color is visible with the naked eye. Meanwhile, in the 90-degree model, the color change on the tartaric acid side is barely visually distinguishable.

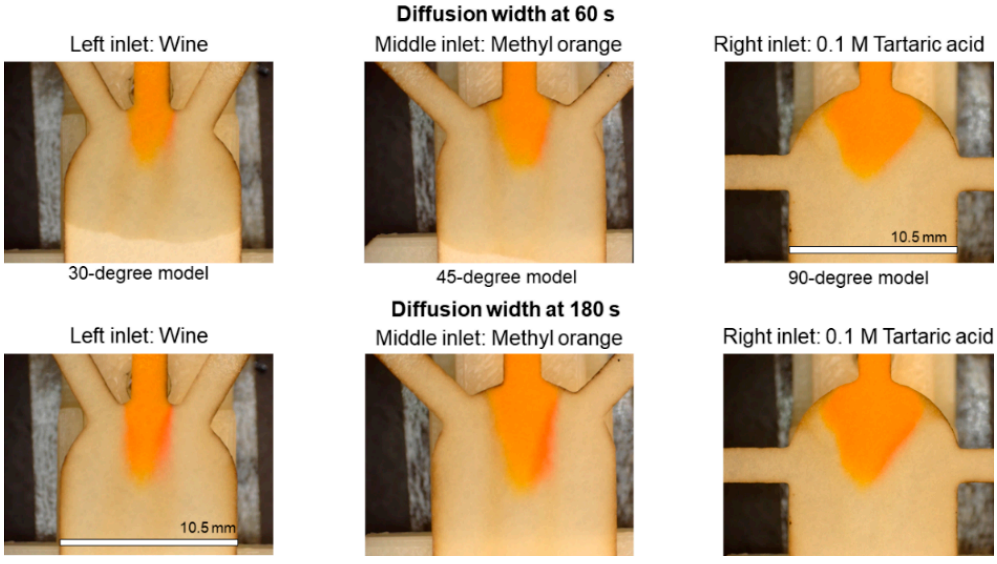

Figure 8. Diffusion widths at 60 s and 120 s after "Time zero" in paper strips with 30°, 45° and 90° of inlets' angle. At all the cases, the wine is flowing through the left inlet and 0.1 M tartaric acid is entering through the right inlet. Scale = 10.5 mm.

Previous numerical results have shown that the dead zones appear in certain regions of the porous medium, and they modify the diffusion width at the steady-state. In agreement with the numerical results, the experimental outcomes reveal that the dead zones do also play a role during the transient flow. Therefore, the change in the inlets' angle creates a different dead-zone area, which modifies the time taken for the flow to achieve a stable laminar flow.

3.2.2. Effect of the Inlets' Angle on the Diffusion Width

In order to define a protocol that produces repeatable and accurate results, the selected time to analyze the intensity of the green channel of the pictures is set to 240 s after the "Time zero".

Figure 9 depicts the intensity of the green channel of the 30-degree and 45-degree models. In agreement with the numerical results, the diffusion width changes with the inlets' angle. In both models, the same reagents (0.1 M tartaric acid from left and 1.0 M tartaric acid from right inlet) are introduced. The arrows A and C in Figure 9 show that both models (the 30 and 45-degree models) are able to reflect the presence of hydronium in the 0.1 M tartaric acid. As is expected, the 30-degree model is more sensitive than the 45-degree model, since the diffusion width is 1.89 mm for the same ionic strength compared to 1.825 mm (arrow C compared to arrow A).

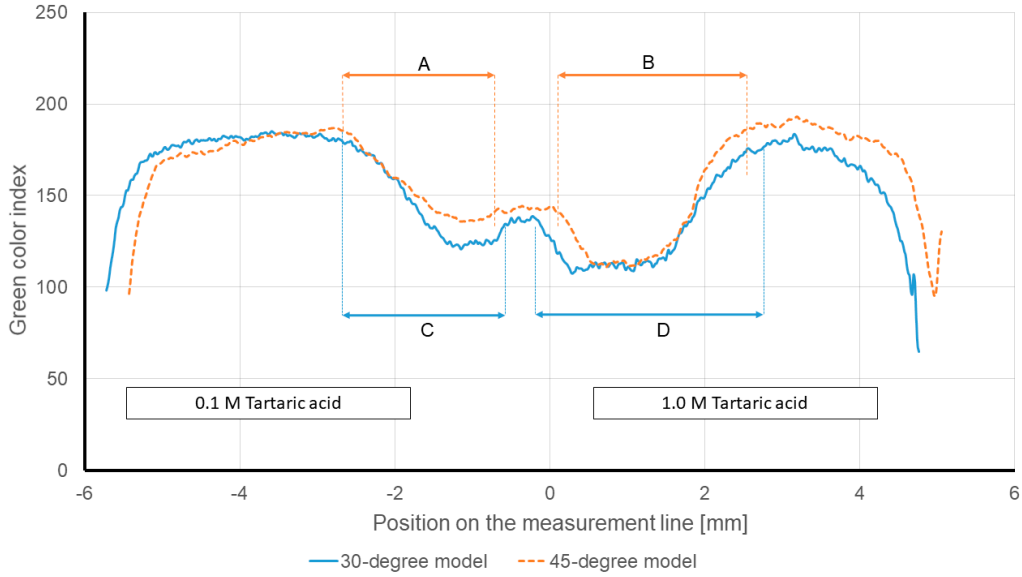

Figure 9. Intensity of the green color channel at the measurement line of different models at 240 s after the "Time zero". In all the models, 0.1 and 1.0 M tartaric acid solutions were entered through the left and right inlets, respectively.

In the same Figure, the arrows B and D show that both models can also reflect the presence of hydronium in the 1.0 M tartaric acid side (right side of the graph). Since the 1.0 M tartaric acid has a higher hydronium concentration compared to the 0.1 M tartaric acid, the intensity of the green channel analysis shows a wider diffusion width on the right side of the graph. The measured diffusion width for the 45-degree model is 2.164 mm (arrow B). While the diffusion width for the 30-degree model increases to 2.594 mm (arrow D). The mentioned results are not only in agreement with the provided justifications, but also, they show that the 30-degree model has higher sensitivity to the hydronium concentration.

Figure 10 plots a visual comparison of the diffusion development in the different models. In all the pictures in Figure 10a, the 0.1 M tartaric acid enters through the left inlet, and the 1.0 M tartaric acid is introduced via the right inlet. According to the pictures i and ii, the 30-degree and 45-degree models show a measurable response to the introduced reagents. On the other hand, in the pictures of Figure 10b, wine enters through the left

inlet, and the 0.1 M tartaric acid is introduced via the right inlet. The comparison shows that only the 30-degree model (picture iv) displays a measurable response to the ionic strength of the wine. The 45-degree model requires further in-depth analysis. Meanwhile, the 90-degree model (iii and vi) is struggling to reflect the ionic strength even for the highest concentrations.

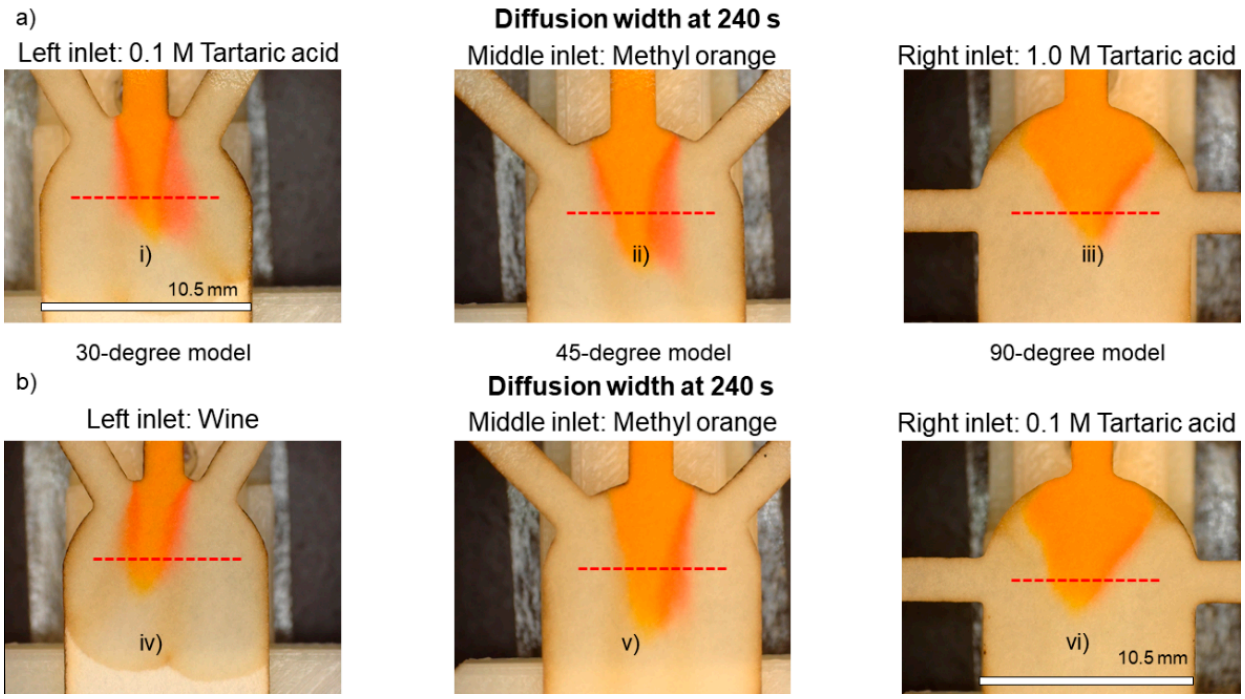

Figure 10. Visual comparison of diffusion development in different models. Measurement line is displayed as the dashed line.

According to the results, if the ionic concentration decreases, the diffusion phenomenon would be more dependent on the geometrical characteristics of the substrate. Therefore, the most accurate geometry would be the 30-degree model. As predicted in the numerical models, the inlets' angle modifies the way the solutions enter the main channel. Subsequently, the encounter of the reagents is affected. By taking into account the results and the provided justifications, it can be concluded that choosing a lower angle for the inlets facilitates the interactions between the fluids of different angles and improves the performance of paper diffusion-based sensors.

The results pointed out by the numerical model were validated experimentally. (Please see Figure 11A). According to the numerical results, the 30-degree model could provide a 2.15 mm of diffusion width. Meanwhile, the 45 and 90-degree models only provide 1.85 and 1.45 mm of diffusion width for the same ionic strength of the solution, respectively. On the other hand, regarding the experimental results, the diffusion width for the 30, 45 and 90-degree models were 1.865, 1.798 and 1.281 mm, respectively (detailed description of the reported diffusion widths of the experimental assays in mentioned in the next paragraph). By comparing the numerical and experimental results, it can be claimed once again that the experimental results support the numerical studies, and the numerical model has simulated the μPAD with acceptable accuracy.

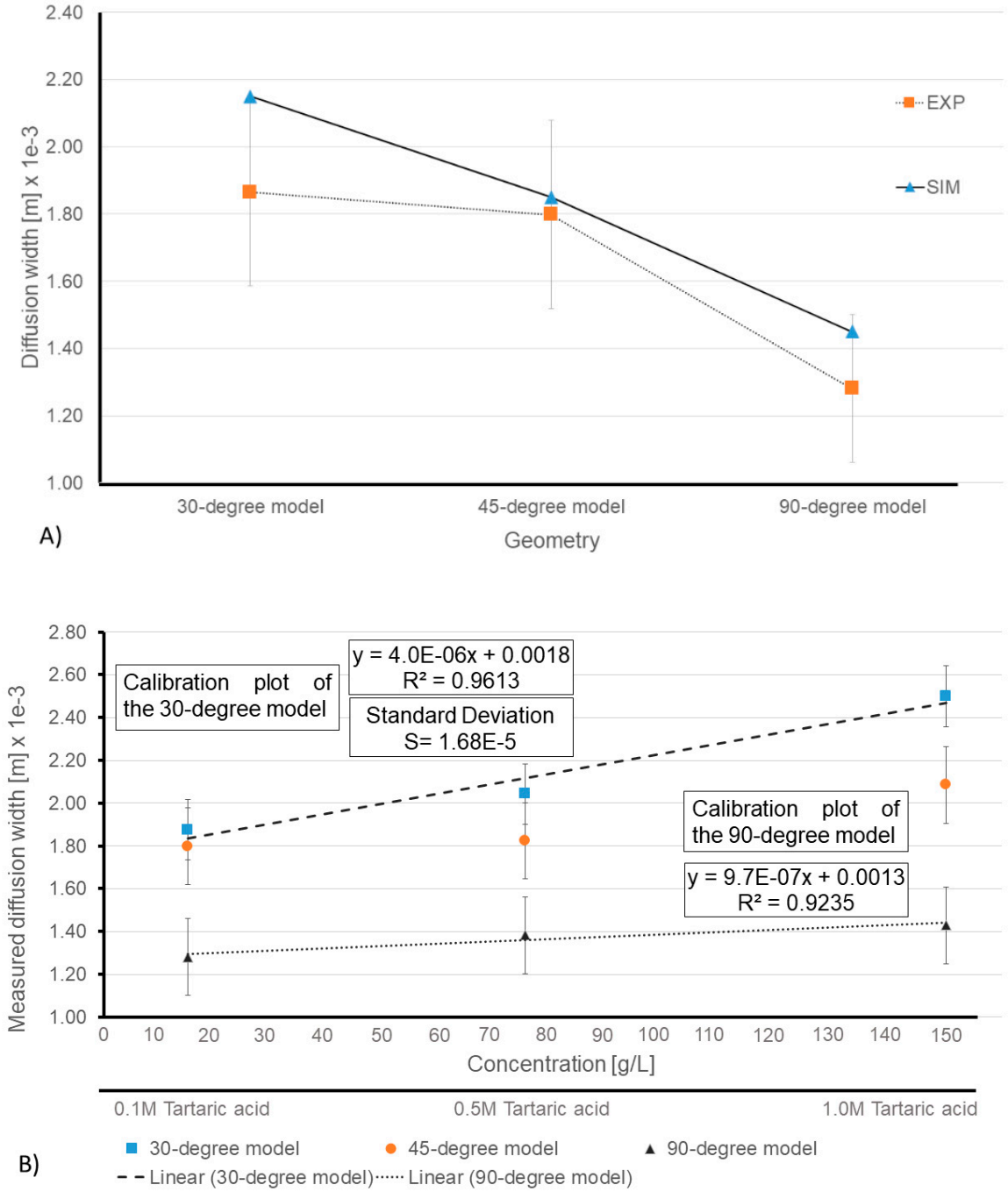

Figure 11. (**A**) Comparison between the diffusion widths in numerical results and the experiments. (**B**) Measured diffusion width based on the changes in the intensity of green channel and the calibration plots of the 30-degree and 90-degree models.

Figure 11B displays the average reported diffusion widths in all the proposed models for the measured green color profile of the reagents (0.1, 0.5 and 1M tartaric acid). The *X*-axis is the concentration based on (g/L) unit, which was converted from the molar (M) unit (with respect to the molar mass of tartaric acid) and the *Y*-axis is the measured diffusion width based on the meter (m) unit, which was converted from the millimeter (mm) unit. Figure 11B clearly shows that the 30-degree model has a steeper regression line, and therefore, it is more sensitive to capture the differences between tartaric acid solutions. Meanwhile, the regression lines in the 45-degree and 90-degree are more gradual and demonstrate poor sensitivity. For instance, the 30-degree model displayed a 1.865 ± 0.28 mm and 2.478 ± 0.18 mm of diffusion width for the 0.1 M and 1.0 M tartaric

acid reagents, respectively. However, the aforementioned values for the 45-degree model were 1.798 ± 0.28 mm and 2.085 ± 0.11 mm, showing only a 200 µm margin between different solutions. The reported margin for the 90-degree model was even worse, when the reported measurements dropped to 1.281 ± 0.22 mm and 1.429 ± 0.21 mm for 0.1 M and 1.0 M tartaric acid solutions, respectively. Moreover, based on the calculated regression line, the 30-degree model displayed a 13.9 g/L limit of detection, whereas the same value for the 90-degree model was reported as 34.6 g/L.

The results showed that, by choosing the inlets' angle properly, even the lowest ionic concentration can be measured with the simplest detection techniques.

3.2.3. Response Time Optimization for the 30-Degree Model

One of the major advantages of the µPADs is the possibility to provide results in a short turnaround time. Heretofore, the results showed that choosing a small angle can magnify the diffusion and shorten its required time. In order to optimize the proposed setup, the diffusion was analyzed at the inlets' intersection of the 30-degree model. The new measurement line was chosen: first, to have the same evaluation position for all the cases, and second, to reduce the required time to evaluate the diffusion zone on the new measurement line (see Figure 12). The test configuration was similar to previous tests, except for the picture capturing time. Pictures were taken at 120, 180 and 240 s after the "Time zero".

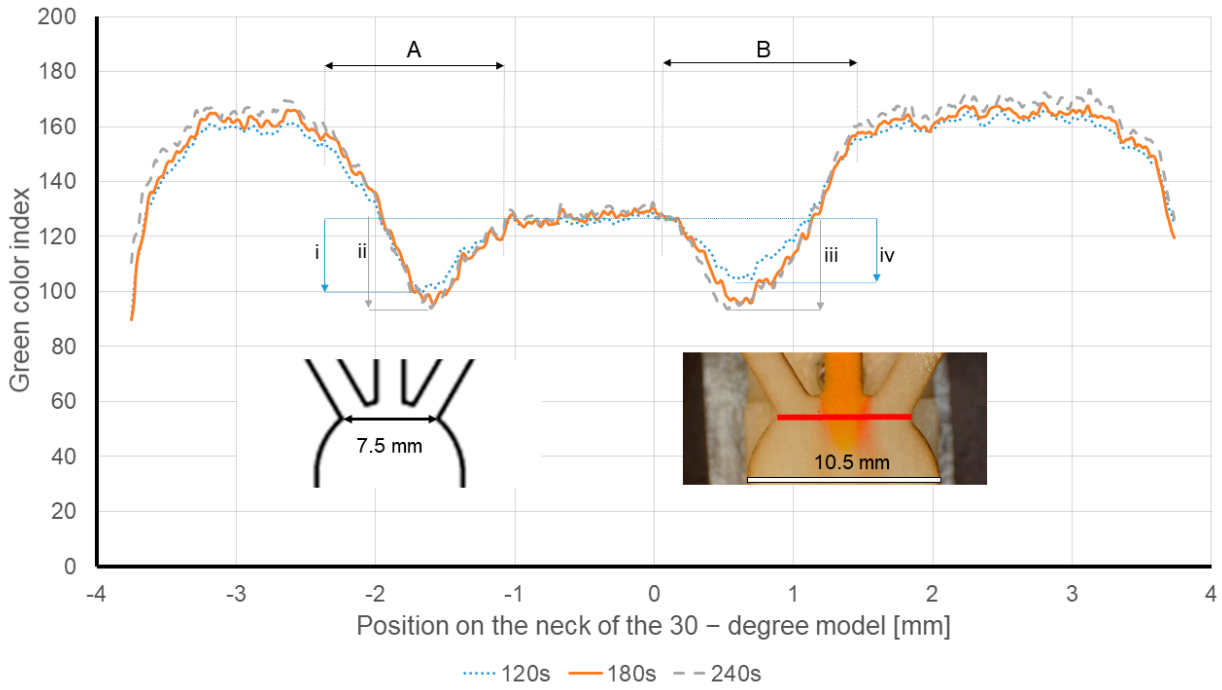

Figure 12. Intensity of the green channel of the diffusion on the measurement line at 120, 180 and 240 s after the time zero. Wine is injected through the left inlet and 0.1 M tartaric acid solution is entered via the right inlet. Red line shows the new measurement line at the neck of the 30-degree model. The dimensions are also illustrated in the pictures.

Figure 12 displays the overlap of the intensity of the green channels of the 30-degree model at 120, 180 and 240 s after the "Time zero". In these experiments, the wine is soaked through the left inlet, and the 0.1M tartaric acid solution is entered via the right inlet. The red line plotted in Figure 12 shows the new measurement line at the neck of the 30-degree model. The arrows A and B show the diffusion width, and the arrows i–iv show the drop in the intensity of the green color channels.

As expected, in all the tests, the measured diffusion width (arrow A) remained constant and only showed insignificant changes over time. The measured diffusion width for the

wine was 938.66 μm ± 14.05 μm, and apparently it was independent of time. For instance, the intensity of the green channel drop is 23.2 units for the wine 120 s after the "Time zero" (arrow i). While the same measurements at 180/240 s after the "Time zero" (arrow ii) only shows a drop of 25 units.

The evolution of the intensity of the green channel of the 0.1 M tartaric acid solution (arrow B) is also measured, being 975.33 μm ± 56.41 μm. However, the intensity of the green channel drop in the tartaric acid side seems to be more affected by the time compared to the wine samples. The drop in the intensity of the green channel is 32.48 units at 180 and 240 s (arrow iii) after the "Time zero", while it is 23.16 units at 120 s. This means that the color change is intensified over time. Therefore, for pH measurements, longer times would be required to achieve accurate measurements in this type of sensor.

To measure the diffusion width, which is the physical value that correlates to the ionic strength, the evaluation at the new measurement line (neck of the 30-degree model) provides reliable results in 120 s and running the test for a longer time period does not alter the diffusion width, as it is plotted in Figure 12 (please see arrows A and B).

The obtained outcomes can be explained by the diffusion flux and the definition of porous medium. As it has been stated before, the smallest dead zones are reported in the 30-degree model. This can be translated into the fact that when the solutions from different inlets enter the main channel, they encounter each other, and they begin to interact (or diffuse) imminently. The existing hydronium from the wine and the tartaric acid solution diffuses into the pH indicator region. Since the hydronium concentration is limited, the resulting diffusion flow would be affected, and the diffusion width growth would be decelerated. Hence, it means that the hydronium ions diffuse further as the time passes, although at a lower rate. Meanwhile, it should be noted that the diffusion is occurring within a porous medium, which generates a flow perpendicular to the diffusion flow. While in the porous media there is a continuous flow from the inlet/s towards the outlet. It is true that the diffusion width increases over time, but there is also a bulk movement from the inlet to outlet. The diffusion is happening inside the porous medium and the hydronium advances further over time, but at the same time, the diffusion zone is moving towards the outlet due to the bulk movement. So, if the evaluation is carried out at a certain line, the measured diffusion width would be independent of the time, and it only relies on the initial flux, while the diffusion flow is affected by the hydronium concentration and time. Therefore, measuring the diffusion width over a line not only eliminates the time factor in the diffusion, but also provides the capability to compare the concentration of species in two solutions. Therefore, the proposed design is suitable for ionic strength measurements.

On the other hand, the drop in the intensity of the green channel is influenced by time. Especially, as the concentration of hydronium increases. The drop in the intensity of the green channel is due to the pH indicator's color shift, and the color shift is caused by the transformation of the methyl orange molecule from the Azo structure to the Quinoid structure. The transform rate is highly affected by the amount of hydronium in the solution and results in the sedimentation of methyl orange salts. At lower hydronium concentrations the sedimentation is limited, but as the concentration increases the sedimentation is augmented dramatically and the salts even form fibers. As a result, the salts and fibers are stranded in the pores, and as the time passes, they accumulate and reflect a more intense color shift.

To validate the performance of the sensor, the diffusion width of the different solutions is measured. The wine shows an average diffusion width of 938.66 ± 14.05 μm, whereas the 0.1, 0.5 and 1.0 M tartaric acid solutions demonstrate an average diffusion width of 975.33 ± 56.41 μm, 1314.08 ± 69.06 μm and 1651.03 ± 34.84 μm, respectively. Figure 13 plots the calibration line obtained from the diffusion width at the inlets' neck for different tartaric acid solutions.

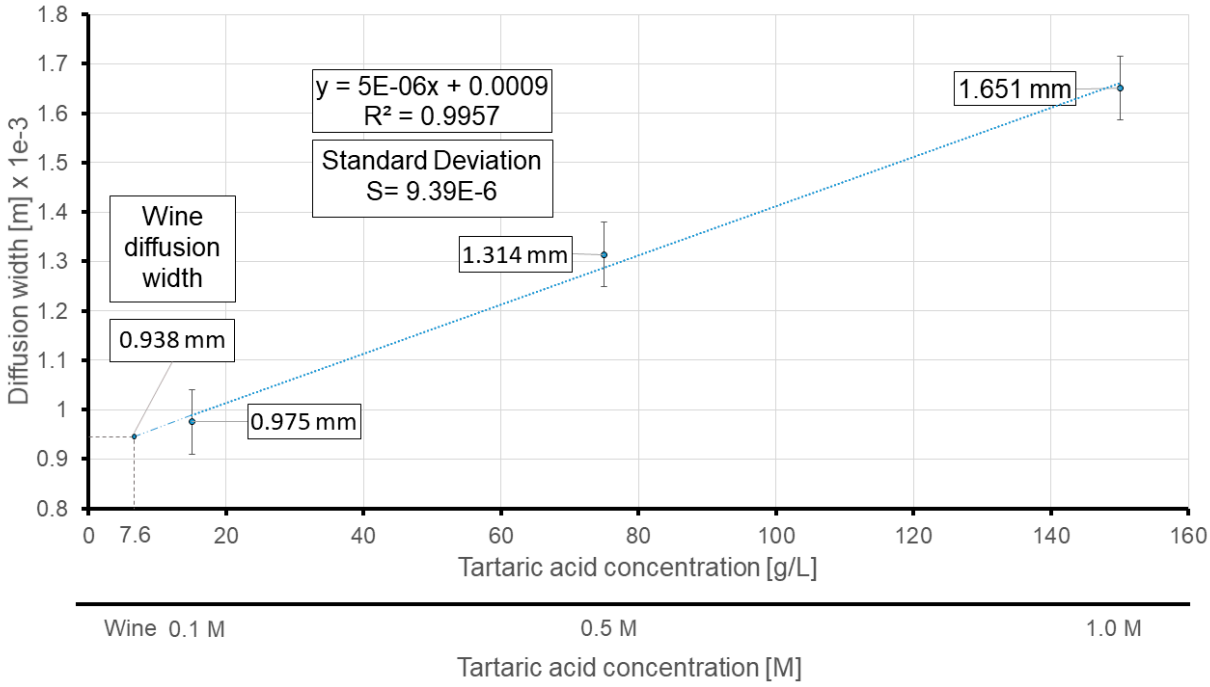

Figure 13. Calibration plot based on the average measured diffusion widths at the new measurement line (neck of the 30-degree model). The predicted concentration of wine is also displayed via extrapolation of the regression line. The units are in millimeters.

Based on the obtained calibration plot, the proposed sensor predicts 7.6 g/L of total acid concentration for the wine sample. Alternatively, the literature HPLC measurements showed that the total acid concentration of white wines varies from 5.64 to 10.7 g/L [42]. The average acid concentration of the white wine, according to the literature, is 7.91 g/L, which is significantly in agreement with the predicted concentration of the wine under study by the sensor.

The limit of detection for the 30-degree model (at the inlets' neck), according to the results, is equal to 6.2 g/L or 41.3 mM, which is an improvement compared to previous μPAD measurements. On the other hand, the obtained LOD legitimized the utilization of the proposed μPAD for ionic strength determination in wines, and once again showed that the diffusion widths of wine and 0.1M tartaric acid are in the same order and outcomes are in agreement with previous studies [43]. Although the reported LOD is not as remarkable as other techniques which require bulky measuring equipment, it should be noted that the proposed self-referencing sensor is designed and validated to be used in remote areas with minimum reliance on sophisticated and laborious detection and quantification techniques. Therefore, even being able to conduct quantitative measurements in less-developed regions can be considered as a great step forward.

On the other hand, the numerical and experimental results also revealed that the orientation of inlets is mainly affecting the neighboring inlets and the flow velocity. This can be translated into the fact that choosing appropriate inlets' angle and type of substrate can expand the variety of tests to be performed. Therefore, the outcomes of this assay can be extrapolated to other studies and improve the μPADs' designs.

Finally, it should be noted that in the experimental section of this assay, we used wine as a sample under analysis. Because in the wine production process, knowing the wine's ionic strength can be later related to the capacity of the wine to be stored for longer periods. We selected the tartaric acid as a reference solution, since according to [42], the tartaric acid is the most abundant acid in wines. However, there are numerous other reagents that can be used for determining the ionic strength (for instance, 0.05M KCl and 0.25M NaOH (1%)

solutions). Therefore, by choosing a different ionic strength reference, this sensor can be applied to numerous other applications.

4. Conclusions

This study proposes a diffusion paper-based sensor to take advantage of microfluidics, 3D fabrication methods and simple detection techniques to widen the capabilities of lab-on-paper platforms. Since the uncontrollable flow is the major drawback of the μPADs, a 3D-printed support was developed to guarantee the flow synchronization in the porous medium, and the flow was analyzed using CFD models.

A CFD model which took as reference the paper characteristics was developed and validated as a useful tool for the design of paper diffusion-based sensors. The model was used to evaluate the effect of the substrate geometry on the flow within the porous medium and to develop a sensor setup that could compare the ionic concentration of an unknown solution to a known solution quantitatively.

The experimental tests were in agreement with the numerical models and validated that less time was required to develop the diffusion zone if the inlets' angles were smaller. For instance, the 30-degree model required 57% less time to develop a diffusion zone compared to the 90-degree model. Moreover, models with inlet angles bigger than 30° were unable to detect concentrations below 0.5 M.

Therefore, the 30-degree model was used to implement a paper diffusion-based sensor to evaluate the ionic strength of wines by comparison to different tartaric acid solutions. This novel sensor presents a limit of detection of 6.2 g/L and it is capable of evaluating the ionic concentration of commercial wines in 120 s without the need of any external equipment or trained personnel. Different substrates can be evaluated to further optimize the turnaround time of the results. This sensor strategy can be applied to other species and using the same model of different paper substrates can be evaluated to tune the generated capillary flow. As a result, the accuracy and the results turnaround time can be enhanced.

Author Contributions: Conceptualization, P.M., S.K., J.A.L.M. and J.C.-T.; methodology, P.M. and J.C.-T.; software, P.M., H.K. and S.K.; validation, P.M., H.K. and S.K.; formal analysis, P.M. and J.C.-T.; investigation, P.M.; resources, S.K. and J.C.-T.; data curation, P.M. and H.K.; writing—original draft preparation, P.M.; writing—review and editing, J.A.L.M. and J.C.-T.; visualization, P.M. and S.K.; supervision, J.C.-T.; project administration, J.C.-T.; funding acquisition, J.C.-T. All authors have read and agreed to the published version of the manuscript.

Funding: This study was partially supported by the La Red Nacional Espanyola de Microfluidica [grant number RED2018-102829-T] together with the European regional development Funds (FEDER) and the Spanish Ministry of Economy and Competitivity (grant number CTQ2017-84966-C2-1-R).

Institutional Review Board Statement: Not applicable.

Informed Consent Statement: Not applicable.

Acknowledgments: The authors are thankful to Universitat Politecnica de Catalunya (UPC) for providing the required materials. We are also highly grateful to CELBIOTECH Lab. for the assistance and providing the technical support.

Conflicts of Interest: The authors declare no conflict of interest.

Appendix A. Grid Study

A mesh independency analysis ensures that the mesh density and distribution are not affecting the final results. We chose the 90-degree model as the basis for mesh refinement and the scalar diffusion as the variable of interest. Since the fluid was flowing through a porous medium, the flow velocity would be relatively small, and the viscous resistance would be considerably large. As a result, the mesh refinement did not have a significant effect on the velocity profile. Thus, we decided to monitor the scalar diffusion. Mesh refinement consisted of six grid groups. The minimum element size varied from 0.5 mm to 25 μm. The details of the studied grids are mentioned in Table 1.

Table 1. The details of the studied mesh distributions.

Grid	1×10^{-4} Element Size (m)	1×10^{-5} Minimum Surface Area (m^2)	Minimum Orthogonal Quality	Number of Iterations
Low	5.0	25.1	0.833	88
Medium	2.5	11.68	0.787	110
High	1.25	6.01	0.661	165
Fine	0.5	1.93	0.69	317
Ultra	0.375	1.75	0.533	358
Ultra-fine	0.25	0.798	0.301	552

In all the cases, it was presumed that the flow velocity is 1.39×10^{-4} m/s. The fluid density and viscosity were set to 998.2 kg/m^3 and 0.001 kg/(m.s), respectively. For mimicking the diffusion (species transport), a User-defined scalar was defined and dedicated to the main channel. The scalar's concentration was set to 0.05 M and its diffusivity was calculated to be 1.29×10^{-7} kg/m.s (Please refer to Section 2.2.3 in this article).

Mixing quality investigations showed that the reported mixing qualities in the "Fine", "Ultra" and "Ultra-fine" mesh refinements were quite similar. Whilst the "Low" mesh distribution showed a mixing quality of 17.3%, the reported mixing quality of the "Ultra-fine" scheme was 6.12%. Comparison between the mixing qualities of the "Fine" and "Ultra-fine" mesh designs only showed a 0.9% of difference. (Please see Figure 3 in the manuscript)

Moreover, according to the results (Figure A1), the "Fine", "Ultra" and "Ultra-fine" mesh schemes provide the most similar results. Point to point comparisons showed that the "Low" mesh scheme has 58.6% of similarity to "Ultra-fine" mesh design. Meanwhile, the results of the "Fine" mesh distribution presented a 96.2% of similarity to the "Ultra-fine" mesh scheme.

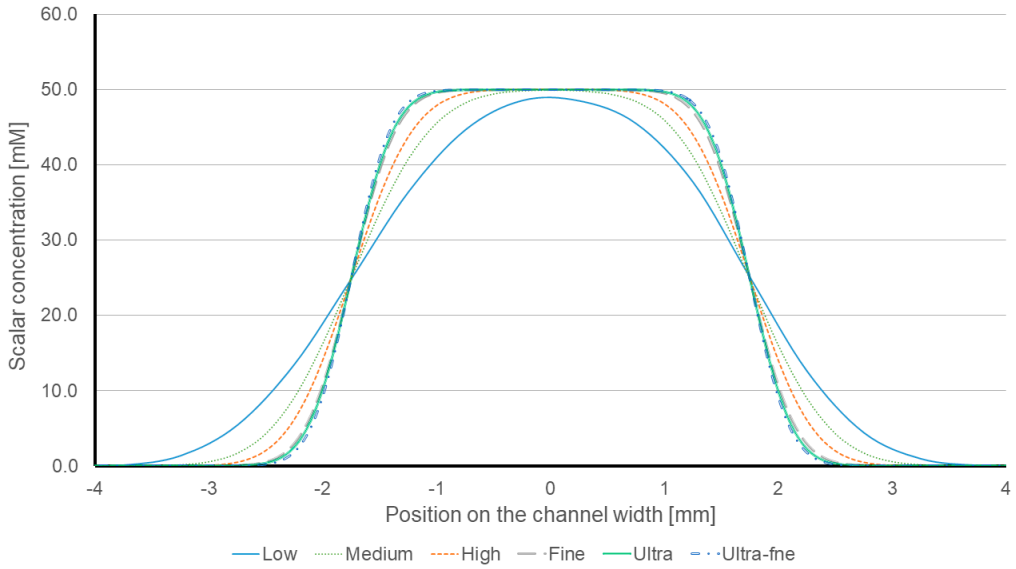

Figure A1. Distribution of scalar with respect to the mesh design in the 90-degree model.

Despite producing the most similar results, the number of required iterations for the results to converge was a determining parameter. Analysis revealed that the number of required iterations for the "Fine" mesh scheme was 42.6% less than the same value for the "Ultra-fine" mesh design and therefore, it was more efficient from the calculation-cost point of view. Considering all the aforementioned points, we decided to use the "Fine" mesh distribution for the numerical analysis.

Appendix B. Limit of Detection

Limit of detection (LOD) expresses the minimum amount of a compound that can be detected in comparison to its absence. One of the most conventional methods for determining the LOD in experimental methods is by considering the generated standard deviation. In most of the assays the distribution of results can be illustrated by a regression line, expressed as:

$$y = mx + b \tag{A1}$$

where m is the slope of the regression line and b is the interception point of the line with the y-axis.

By determining the regression line formula and obtaining the standard deviation (S) of the assays, the limit of detection can be found through:

$$LOD = 3.3 \times \frac{S}{m} \tag{A2}$$

References

1. Whitesides, G.M. The origins and the future of microfluidics. *Nature* **2006**, *442*, 368–373. [CrossRef] [PubMed]
2. Akyazi, T.; Basabe-Desmonts, L.; Benito-Lopez, F. Review on microfluidic paper-based analytical devices towards commercialisation. *Anal. Chim. Acta* **2018**, *1001*, 1–17. [CrossRef] [PubMed]
3. Zhu, H.; Fohlerová, Z.; Pekárek, J.; Basova, E.; Neužil, P. Recent advances in lab-on-a-chip technologies for viral diagnosis. *Biosens. Bioelectron.* **2020**, *153*, 112041. [CrossRef]
4. Chinnadayyala, S.R.; Park, J.; Le, H.T.N.; Santhosh, M.; Kadam, A.N.; Cho, S. Recent advances in microfluidic paper-based electrochemiluminescence analytical devices for point-of-care testing applications. *Biosens. Bioelectron.* **2019**, *126*, 68–81. [CrossRef]
5. Karimi, S.; Mehrdel, P.; Farré-Lladós, J.; Casals-Terré, J. A passive portable microfluidic blood-plasma separator for simultaneous determination of direct and indirect ABO/Rh blood typing. *Lab Chip* **2019**, *19*, 3249–3260. [CrossRef] [PubMed]
6. Karimi, S.; Mehrdel, P.; Casals-Terré, J.; Farré-Llados, J. Cost-effective microfabrication of sub-micron-depth channels by femto-laser anti-stiction texturing. *Biofabrication* **2020**, *12*, 025021. [CrossRef] [PubMed]
7. Ai, Y.; Zhang, F.; Wang, C.; Xie, R.; Liang, Q. Recent progress in lab-on-a-chip for pharmaceutical analysis and pharmacological/toxicological test. *TrAC—Trends Anal. Chem.* **2019**, *117*, 215–230. [CrossRef]
8. Amor-Gutiérrez, O.; Costa-Rama, E.; Fernández-Abedul, M.T. Sampling and multiplexing in lab-on-paper bioelectroanalytical devices for glucose determination. *Biosens. Bioelectron.* **2019**, *135*, 64–70. [CrossRef]
9. Yetisen, A.K.; Akram, M.S.; Lowe, C.R. Paper-based microfluidic point-of-care diagnostic devices. *Lab Chip* **2013**, *13*, 2210–2251. [CrossRef]
10. Sriram, G.; Bhat, M.P.; Patil, P.; Uthappa, U.T.; Jung, H.Y.; Altalhi, T.; Kumeria, T.; Aminabhavi, T.M.; Pai, R.K.; Madhuprasad; et al. Paper-based microfluidic analytical devices for colorimetric detection of toxic ions: A review. *TrAC—Trends Anal. Chem.* **2017**, *93*, 212–227. [CrossRef]
11. Cate, D.M.; Adkins, J.A.; Mettakoonpitak, J.; Henry, C.S. Recent developments in paper-based microfluidic devices. *Anal. Chem.* **2015**, *87*, 19–41. [CrossRef]
12. Lisowski, P.; Zarzycki, P.K. Microfluidic paper-based analytical devices (μPADs) and micro total analysis systems (μTAS): Development, applications and future trends. *Chromatographia* **2013**, *76*, 1201–1214. [CrossRef]
13. Zhang, Y.; Rochefort, D. Activity, conformation and thermal stability of laccase and glucose oxidase in poly(ethyleneimine) microcapsules for immobilization in paper. *Process Biochem.* **2011**, *46*, 993–1000. [CrossRef]
14. Wang, S.; Ge, L.; Song, X.; Yu, J.; Ge, S.; Huang, J.; Zeng, F. Paper-based chemiluminescence ELISA: Lab-on-paper based on chitosan modified paper device and wax-screen-printing. *Biosens. Bioelectron.* **2012**, *31*, 212–218. [CrossRef] [PubMed]
15. Lashgari, M.; Yamini, Y. An overview of the most common lab-made coating materials in solid phase microextraction. *Talanta* **2019**, *191*, 283–306. [CrossRef] [PubMed]
16. Li, X.; Ballerini, D.R.; Shen, W. A perspective on paper-based microfluidics: Current status and future trends. *Biomicrofluidics* **2012**, *6*, 011301. [CrossRef] [PubMed]
17. Jagadeesan, K.K.; Kumar, S.; Sumana, G. Application of conducting paper for selective detection of troponin. *Electrochem. Commun.* **2012**, *20*, 71–74. [CrossRef]
18. Nguyen, V.T.; Song, S.; Park, S.; Joo, C. Recent advances in high-sensitivity detection methods for paper-based lateral-flow assay. *Biosens. Bioelectron.* **2020**, *152*, 112015. [CrossRef]
19. Li, F.; Liu, J.; Guo, L.; Wang, J.; Zhang, K.; He, J.; Cui, H. High-resolution temporally resolved chemiluminescence based on double-layered 3D microfluidic paper-based device for multiplexed analysis. *Biosens. Bioelectron.* **2019**, *141*, 111472. [CrossRef] [PubMed]
20. Escobedo, P.; Erenas, M.M.; Martínez-Olmos, A.; Carvajal, M.A.; Gonzalez-Chocano, S.; Capitán-Vallvey, L.F.; Palma, A.J. General-purpose passive wireless point–of–care platform based on smartphone. *Biosens. Bioelectron.* **2019**, *141*, 111360. [CrossRef]

21. Kim, W.; Lee, S.; Jeon, S. Enhanced sensitivity of lateral flow immunoassays by using water-soluble nanofibers and silver-enhancement reactions. *Sens. Actuators B Chem.* **2018**, *273*, 1323–1327. [CrossRef]
22. Parolo, C.; de la Escosura-Muñiz, A.; Merkoçi, A. Enhanced lateral flow immunoassay using gold nanoparticles loaded with enzymes. *Biosens. Bioelectron.* **2013**, *40*, 412–416. [CrossRef] [PubMed]
23. Walczak, R.; Dziuban, J.; Szczepańska, P.; Scholles, M.; Doyle, H.; Krüger, J.; Ruano-Lopez, J. Toward Portable Instrumentation for Quantitative Cocaine Detection with Lab-on-a-Paper and Hybrid Optical Readout. *Procedia Chem.* **2009**, *1*, 999–1002. [CrossRef]
24. Gerold, C.T.; Bakker, E.; Henry, C.S. Selective Distance-Based K+ Quantification on Paper-Based Microfluidics. *Anal. Chem.* **2018**, *90*, 4894–4900. [CrossRef] [PubMed]
25. Apilux, A.; Dungchai, W.; Siangproh, W.; Praphairaksit, N.; Henry, C.S.; Chailapakul, O. Lab-on-paper with dual electrochemical/colorimetric detection for simultaneous determination of gold and iron. *Anal. Chem.* **2010**, *82*, 1727–1732. [CrossRef] [PubMed]
26. Wei, X.; Tian, T.; Jia, S.; Zhu, Z.; Ma, Y.; Sun, J.; Lin, Z.; Yang, C.J. Target-responsive DNA hydrogel mediated stop-flow microfluidic paper-based analytic device for rapid, portable and visual detection of multiple targets. *Anal. Chem.* **2015**, *87*, 4275–4282. [CrossRef]
27. Kong, T.; You, J.B.; Zhang, B.; Nguyen, B.; Tarlan, F.; Jarvi, K.; Sinton, D. Accessory-free quantitative smartphone imaging of colorimetric paper-based assays. *Lab Chip* **2019**, *19*, 1991–1999. [CrossRef]
28. Abo Dena, A.S.; Bayoumi, E.E. Lab-on-paper optical sensor for smartphone-based quantitative estimation of uranyl ions. *J. Radioanal. Nucl. Chem.* **2018**, *318*, 1439–1445. [CrossRef]
29. Jeong, S.G.; Kim, J.; Jin, S.H.; Park, K.S.; Lee, C.S. Flow control in paper-based microfluidic device for automatic multistep assays: A focused minireview. *Korean J. Chem. Eng.* **2016**, *33*, 2761–2770. [CrossRef]
30. Lim, H.; Jafry, A.T.; Lee, J. Fabrication, flow control, and applications of microfluidic paper-based analytical devices. *Molecules* **2019**, *24*, 2869. [CrossRef] [PubMed]
31. Apilux, A.; Ukita, Y.; Chikae, M.; Chailapakul, O.; Takamura, Y. Development of automated paper-based devices for sequential multistep sandwich enzyme-linked immunosorbent assays using inkjet printing. *Lab Chip* **2013**, *13*, 126–135. [CrossRef]
32. Fu, E.; Liang, T.; Spicar-Mihalic, P.; Houghtaling, J.; Ramachandran, S.; Yager, P. Two-dimensional paper network format that enables simple multistep assays for use in low-resource settings in the context of malaria antigen detection. *Anal. Chem.* **2012**, *84*, 4574–4579. [CrossRef]
33. Lutz, B.; Liang, T.; Fu, E.; Ramachandran, S.; Kauffman, P.; Yager, P. Dissolvable fluidic time delays for programming multi-step assays in instrument-free paper diagnostics. *Lab Chip* **2013**, *13*, 2840–2847. [CrossRef]
34. Osborn, J.L.; Lutz, B.; Fu, E.; Kauffman, P.; Stevens, D.Y.; Yager, P. Microfluidics without pumps: Reinventing the T-sensor and H-filter in paper networks. *Lab Chip* **2010**, *10*, 2659–2665. [CrossRef] [PubMed]
35. Casals-Terré, J.; Farré-Lladós, J.; Zuñiga, A.; Roncero, M.B.; Vidal, T. Novel applications of nonwood cellulose for blood typing assays. *J. Biomed. Mater. Res. Part B Appl. Biomater.* **2019**, *107*, 1533–1541. [CrossRef] [PubMed]
36. Yazdchi, K.; Srivastava, S.; Luding, S. On the validity of the carman-kozeny equation in random fibrous media. In Proceedings of the International Conference on Particle-Based Methods (PARTICLES)—II International Conference on Particle-Based Methods: Fundamentals and Applications (PARTICLES 2011), Barcelona, Spain, 26–28 October 2011; pp. 264–273.
37. Giri, B. *Laboratory Methods in Microfluidics*; Elsevier: Amsterdam, The Netherlands, 2017; ISBN 9780128132364.
38. Du Plessis, E.; Woudberg, S. Modelling of diffusion in porous structures. *WIT Trans. Eng. Sci.* **2009**, *63*, 399–408. [CrossRef]
39. Mehrdel, P.; Karimi, S.; Farré-Lladós, J.; Casals-Terré, J. Novel variable radius spiral-shaped micromixer: From numerical analysis to experimental validation. *Micromachines* **2018**, *9*, 552. [CrossRef] [PubMed]
40. Danner, L.; Niimi, J.; Wang, Y.; Kustos, M.; Muhlack, R.A.; Bastian, S.E.P. Dynamic viscosity levels of dry red and white wines and determination of perceived viscosity difference thresholds. *Am. J. Enol. Vitic.* **2019**, *70*, 205–211. [CrossRef]
41. Ivorra, B.; Redondo, J.L.; Santiago, J.G.; Ortigosa, P.M.; Ramos, A.M. Two- and three-dimensional modeling and optimization applied to the design of a fast hydrodynamic focusing microfluidic mixer for protein folding. *Phys. Fluids* **2013**, *25*, 032001. [CrossRef]
42. Prenesti, E.; Berto, S.; Toso, S.; Daniele, P.G. Acid-base chemistry of white wine: Analytical characterisation and chemical modelling. *Sci. World J.* **2012**, *2012*, 249041. [CrossRef]
43. Mehrdel, P.; Karimi, S.; Farre-llados, J.; Casals-terré, J. Portable 3D-printed sensor to measure ionic strength and pH in buffered and non-buffered solutions Pouya Mehrdel. *Food Chem.* **2021**, *344*, 128583. [CrossRef] [PubMed]